CAPTURING THE NON-LINEAR DYNAMICS OF PARTICLE MIGRATION IN COMPLEX VISCOUS FLOWS

by

Abimbola Adetola Abatan

B.S., Clark Atlanta University, December 2000

M.S., University of Pittsburgh, August 2003

Submitted to the Graduate Faculty of

the School of Engineering in partial fulfillment

of the requirements for the degree of

Doctor of Philosophy

University of Pittsburgh

2007

UNIVERSITY OF PITTSBURGH

SCHOOL OF ENGINEERING

This dissertation was presented

by

Abimbola Adetola Abatan

It was defended on

June 27^{th} 2006

and approved by

Joseph J. McCarthy, Ph.D., Associate Professor

Robert S. Parker, Ph.D.,Associate Professor

Sachin S. Velankar, Ph.D., Assistant Professor

Anne M. Robertson, Ph.D., Associate Professor

Dissertation Director: Joseph J. McCarthy, Ph.D., Associate Professor

ABSTRACT

CAPTURING THE NON-LINEAR DYNAMICS OF PARTICLE MIGRATION IN COMPLEX VISCOUS FLOWS

Abimbola Adetola Abatan, PhD

University of Pittsburgh, 2007

Low Reynolds number multiphase flows are prevalent in many industrial applications, such as separations processes, cell growth in bioreactors and catalysis operations. Due to the interplay between phases, the characterization of these flows is rather complex yet necessary to fully understand the intrinsic dynamics. This study discusses the interactions between a viscous fluid phase and rigid particles dispersed within the fluid.

The particles are observed to spontaneously migrate within the toroidal structures that form between rotating flat-disk impellers to repeatable non-trivial asymptotic locations. The stability of the asymptotic migration positions is dependent on flow and particle conditions and includes both the exact center of the torus as well as other intermediate locations that are classified as higher order clusters. It is of particular interest that the particle clusters coincide with the location of unmixed islands within the underlying flow, illustrating significant coupling between the solid and fluid behavior. Furthermore, the results also show that migratory competition can occur when multiple particles are introduced into the same flow region.

This behavior is also examined using a one-way coupled Lagrangian-Eulerian model based on the Basset-Boussinesq-Oseen (BBO) equation. In this approach, particle motion is captured by incorporating a variety of fluid-particle force models into a Eulerian treatment of the flow field. Although a regular cellular flow is able to capture rotation rate and particle diameter effects, it is unable to provide insight into interactions between the particles and

any secondary island structures that exist in many rotating flow systems. Thus, a 2D approximation of the experimental cellular flow is obtained by a perturbing a cellular flow streamfunction to produce fluid island structures. The model was then used to analyze a dilute suspension of slightly non-neutrally buoyant solid spheres as they migrate across the curved fluid streamlines of the viscous flow. The effect of the Saffman lift force on the lateral migration of the solid spheres is also evaluated. Without this additional term, the BBO model predicts an inward motion solely for light particles, whereas heavy particles are predicted to migrate outwards. However when included into the BBO model, both types of particles exhibit inward migration which is analogous to our experimental work. The equilibrium particle location could be manipulated by varying the flow characteristics and stability of the fluid islands.

It is believed that this thesis significantly contributes to the understanding and perhaps eventual manipulation of the hydrodynamic interactions within such systems to yield spontaneously organized, 'structured suspensions'. This work can be extended to study the migration behavior of other discrete entities within a flow such as bubbles or droplets by appropriate modification of the experimental and computational procedures to other geometries.

DESCRIPTORS

BBO	Lift Force
Low Reynolds Number	Multiphase Flow
Particle Migration	Rotating Flow

TABLE OF CONTENTS

LIST OF TABLES

LIST OF FIGURES

PREFACE

My thanks to Dr. McCarthy for his guidance and support as my advisor at the University of Pittsburgh. You challenged me scientifically, exposed me to new ideas and taught me to work independently. My thanks to the members of my committee- Dr. Parker, Dr. Velankar and Dr. Robertson. Whether instructing me in a class, providing expertise on an experiment or verbally providing encouragment, you have each played a significant role towards the completion of my degree.

My thanks to the following past and present members of the Granular Transport Group- Watson Vargas, Steve Nase, Kunal Jain, Hongming Li, Deliang Shi and Isabel Figueroa. It has been a pleasure learning with each of you. My heartfelt thanks to my amazing family. Completing this degree would not have been possible without your love and support. And finally, to the One who was and is always with me; who by His sacrifice so long ago showed me what it was to persevere. Yahweh, Olodumare- this is for your glory.

1.0 INTRODUCTION

Consider the natural motion of waves on a body of water due to the wind. Now consider the complex counter-rotating eddies that can form as one of those waves interacts with a standing man-made structure in the sea. Although these patterns are aesthetically pleasing, they can also be appreciated for the scientific principles which they elegantly exhibit. Such systems often exhibit non-uniform mixing which can lead to complex transport properties when characterizing the system.

In spite of these difficulties, the study of complex flows has persisted due to their prevalence in a variety of industrial process units, such as cyclone separators and stirred tank reactors. Various methods have been applied to these problems to determine the process parameters that allow the maximum mixing efficiency when homogeneity (in the context of an even product distribution) is desired.

The viscosity of the fluid greatly factors into the behavior of complex flows. For low viscosity fluids, increases in fluid velocity can quickly introduce turbulence into the system, which can add a considerable amount of disorder and difficulty. For highly viscous systems however, the onset of turbulence is greatly delayed thereby allowing the analysis of these systems by tools that do not have to account for secondary and tertiary eddies due to turbulence. The addition of another phase - for example, solid particles - also contributes another layer of complexity to the mixing behavior of what is now a multiphase flow. These systems are often non-uniformly mixed, either due to the character of the flow field (which can contain recirculation zones, vortices, eddies, etc) or due to the presence of a particulate phase, leading to complex transport properties.

The behavior of particles small enough to be affected by the molecular thermal energy from the fluid is characterized as Brownian motion. Such particles are passively advected

by the fluid; i.e., the fluid drag is the determinant force on the particle and thus the particle motion effectively mirrors that of the fluid streamlines. On the other hand, non-Brownian particles have long been observed to deviate from the streamlines, resulting in rather interesting behavior. Segré and Silberberg [4, 5] first showed that neutrally buoyant particles could migrate across flow streamlines to non-trivial equilibrium positions within a uni-directional flow. In this pioneering work, the small rigid particles were not merely passively advected, but migrated *across* fluid streamlines to the equilibrium radial position, regardless of their initial positions. They termed this phenomena the 'tubular-pinch effect', given that the particles maintained a radial position similar in shape to the vessel in which they flowed – a pinched tube formation. This behavior has been validated both experimentally and computationally, most recently by Chun and Ladd [6, 7] using the Lattice Boltzmann simulation technique.

Particles have also been observed to migrate in dense multi-particle flows even in the case of vanishing Reynolds number (*i.e.* an ideal Stokes' flow) due to interactions between the particles [8, 9, 10, 11, 12]. These studies showed that particles in relatively concentrated suspensions can segregate into discrete bands upon shearing a half-filled Taylor-Couette system- an instability which which has been termed 'shear-induced migration'. Behavior such as shear-thinning near vessel walls [11, 13, 14] has been observed at rates significantly faster than by diffusion alone. Attempts at characterizing this phenomenon has produced studies which evaluated the effects of particle density [15, 16, 17], particle asphericity and/or deformability [18, 19, 20, 21, 12], particularly in Poiseuille [22, 23] and Couette flows. [24, 25, 26, 27]

Particle migration has also been observed in concentrated particle flows even in the case of vanishing Reynolds number (i.e., an ideal Stokes' flow) due to hydrodynamic interactions between the particles, [8] a phenomenon which has been termed 'shear-induced migration'. This has also been postulated for the observed migration of polymer chains within a pressure driven flow [12] and the migration of red blood cells towards the center of a blood vessel [13]. The cause of migration in these flows has been attributed to thermodynamic effects, meaning the particle(s) migrate to regions of lowest shear in the flow field. However symmetry can cancel out the effects of a shear gradient, thus other forces must be at work.

Another theory is that kinetics/hydrodynamics are the predominant forces causing the particle to move from the solid boundaries of the flow field and towards the center of the flow profile. For non-neutrally buoyant particles (i.e. For particles of a different density than the fluid, buoyancy effects gain importance [28, 29, 30], and in multi-directional flows, non-linear fluid effects [31, 32, 3] which arise at moderate Reynolds numbers become an added point of interest. All of these studies bear relevance to this particular analysis of the multiphase toroidal flow between parallel flat disks, and it will be shown that a combination of forces are at work to explain the observed behavior.

More than just the migration direction, it is also important to evaluate the equilibrium location of the particles with respect to the fluid within a system. Multiple local equilibrium positions were reported by Joseph *et al.*, [33, 34] who investigated both neutrally buoyant and slightly non-neutrally buoyant particles in Poiseuille and Couette flows using Direct Numerical Simulation (DNS) techniques. They found that heavier (denser) particles can undergo turning-point transitions which can lead to multiple equilibrium positions at certain Reynolds numbers in Newtonian and viscoelastic flows. This illustrated the importance of a lift term based on the slip velocity and particle rotation- a finding which is further reinforced even for non-Brownian particles in the computational results of this study.

This brief history illustrates the difficulty associated with elegantly capturing the physics of multiphase flows. The primary interest of this dissertation is understanding the fluid-particle interactions in dilute flows, thus particle-particle effects are beyond the scope of the research presented here. Our analysis can generally be restricted to an individual particle; specifically, the migration of single solid spheres within the toroidal flow formed in a stirred tank with flat disk impellers.

The structure of this work is as follows: Chapter 2 provides the foundation for this work with a discussion of previous research on fluid mixing mechanisms in various rotating flows, various studies of particle migration and pertinent computational tools to analyze of these systems. Chapter 3 explains the primary experimental setup of this work and flow visualization of the particle motion within the stirred tank flow. The impact of certain parameters (particle density, impeller spacing, rotation rate, *etc.*) on the asymptotic position of the particles are also investigated. Chapter 4 describes the use of a CFD tool to evaluate

symmetry effects within the stirred tank flow. Chapter 5 discusses the use of a 2D analytical model to examine migration in both regular and chaotic flows and probe relevant forces. This chapter also elaborates on the use of non-integrable time perturbations on the steady flow field to understand the effects of periodicity within these flows. Chapter 7 concludes with a comprehensive summary and possible directions/applications for this work.

2.0 BACKGROUND

This thesis builds on the pioneering work of Segré and Silberberg [4] by further exploring the interactions between a viscous fluid phase and discrete solid particles randomly dispersed within that fluid. Particle migration in rotating flows is poorly understood due to the streamline curvature and complex inner structure of the fluid.

Several researchers have contributed to the field, such as Chan and Fung [26], who investigated the terminal velocity or gravitational settling of small non-neutrally buoyant spheres within a cellular flow field. They noted a 'crossing-trajectory effect' where particles crossed fluid streamlines as a result of the fluid inertia and buoyancy forces, similar to the work by Segré and Silberberg [4] in the the pipe flow. Ye and Roco [16] evaluated the motion of neutrally-buoyant polystyrene beads in a turbulent Couette flow, using a successive freeze-frame approach. They studied the effects of particle size and proximity to wall boundaries (both stationary and moving), and observed that particle spin about its own axis was higher near the moving portion of the apparatus versus near a stationary wall as a result of a higher velocity gradient. In addition, the angular velocity of the particles decreased with increasing diameter, which the authors speculated was due to another mechanism other hydrodynamic effects.

Crisanti *et al.* [15] studied the motion of small particles in a steady, periodic cellular flow. Although the particles were small enough to be tracers, they were alternatively lighter or heavier than the fluid phase. The authors observed that lighter particles migrated to the center of the cellular flow, but heavier particles diffused through the cell in a manner they termed 'inertial diffusion' of no particular direction. These researchers also noted that the particles themselves did not display chaotic behavior- rather, the random motion observed was directly related to the density difference between the particles and the fluid. That is,

for light particles, stable locations could be defined within the flow that acted as attractors for the particles. In contrast, these locations were unstable for heavy particles and therefore generated the diffusive paths reported.

Following that brief history, a basic discussion of various rotating flows of particular interest to this study is found in section 2.1 with further discussion on various particle migration mechanisms in multiphase systems. Section 2.2 presents the BBO model and illustrates its particular applicability to this study, and section 2.3 discusses the use of a particular CFD package to understand the underlying flow mechanics.

2.1 MIXING AND MIGRATION IN ROTATING FLOWS

What follows is a brief overview of such systems with particular focus on particle migration in rotating flows to fully appreciate the novelty of this work. The study of rotating fluid flow systems have significant relevance in certain chemical engineering processes such as bioreactor design and membrane filtration apparatus. Although the interplay between phases makes the characterization of these flows rather complex, it is still necessary to fully understand the intrinsic dynamics of these processes.

2.1.1 Taylor-Couette Flow

A well-known rotating flow is the Taylor-Couette system illustrated in Figure 1. The apparatus is usually made up of two concentric cylinders of different diameter which can rotate in the same or opposite directions. The resulting stacked vortices that form in the annulus/gap between the cylinders are counter-rotating (shown in Figure 1b) and are comprised of invariant nested stream surfaces. Studies have shown that the stability of the vortices is highly dependent on the rotation rates (Ω_1, Ω_2) and the annular spacing ($R_2 - R_1$). For example, Ashwin *et al.* [35] showed that particle paths can be mathematically confined to 2D recirculating surfaces for stable modes. Flow fields which contain such surfaces are commonly called cellular flows. King *et al.* [36] concluded that rotational symmetry maintains

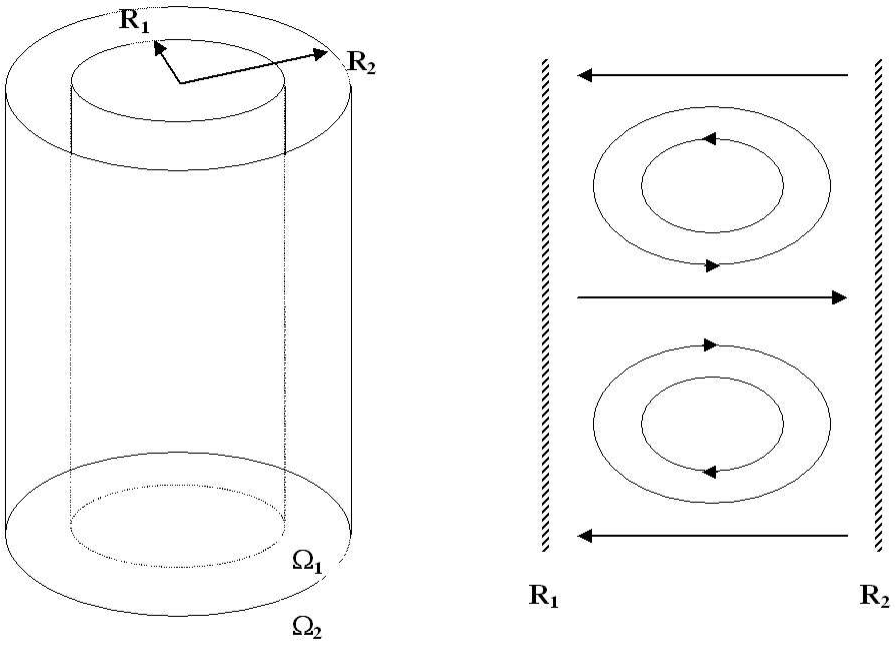

Figure 1: Schematic of Taylor-Couette flow: (a) concentric cylinder setup characterized by cylinder radii (R_1, R_2) and rotation rates (Ω_1, Ω_2); (b) counter-rotating tori that form in the gap between the cylinders.

the stability of the cellular flow. At higher rotation rates, the vortices have been shown to transition to what is commonly known as *wavy* Taylor-Couette flow due to instabilities and a loss of symmetry in the fluid system.

Baier and Graham [37] studied the flow patterns which form as a result of using two inviscid fluids within the Taylor-Couette gap. Such a two fluid system yields side-by-side vorticular regions which can be made stable or unstable based on the co- or counter-current rotation rates of the cylinders. Still others [38, 39] have studied particle motion in these flows, and corroborated findings that non-wavy Taylor vortices are independent cells with no cross-flow between vortices while examining the physical mechanism which causes particle segregation in such flows, particularly as a function of particle density. These studies have also shown that the deviation of particle paths from fluid streamlines becomes more pronounced as the density ratio increases.

If we define a well-mixed system as one which is largely homogeneous in nature, then the vortices or toroidal structures which characterize cellular flows will largely be barriers to mixing, particularly at low Reynolds numbers. King *et al.* [36] showed that the Taylor-Couette tori are separated by Kolmogorov-Arnold-Moser (KAM) surfaces such that they are isolated from the outside flow and from each other except through molecular diffusion. It follows then that the motion of small solid spheres within such a flow will be greatly influenced by the fluid structure. Indeed, Annamalai and Cole [40] observed that droplets settling under the influence of gravity within a low Reynolds (Re) number flow will spiral inward in a direction perpendicular to gravity to a smaller radial position than the initial location due to an induced particle rotation.

2.1.2 Secondary Structures and Rotating Disks

A viscous fluid between parallel rotating disks (such as the simple schematic in Figure 2) within a stirred tank can also produce vortices/tori similar in structure to the Taylor-Couette cells. Any perturbation of the main tori in Figure 2 can yield the secondary island structures shown as a result of the folding and bending of the internal concentric structure. Such disturbances can lead to heterogeneous areas within the flow where some exhibit the characteristics

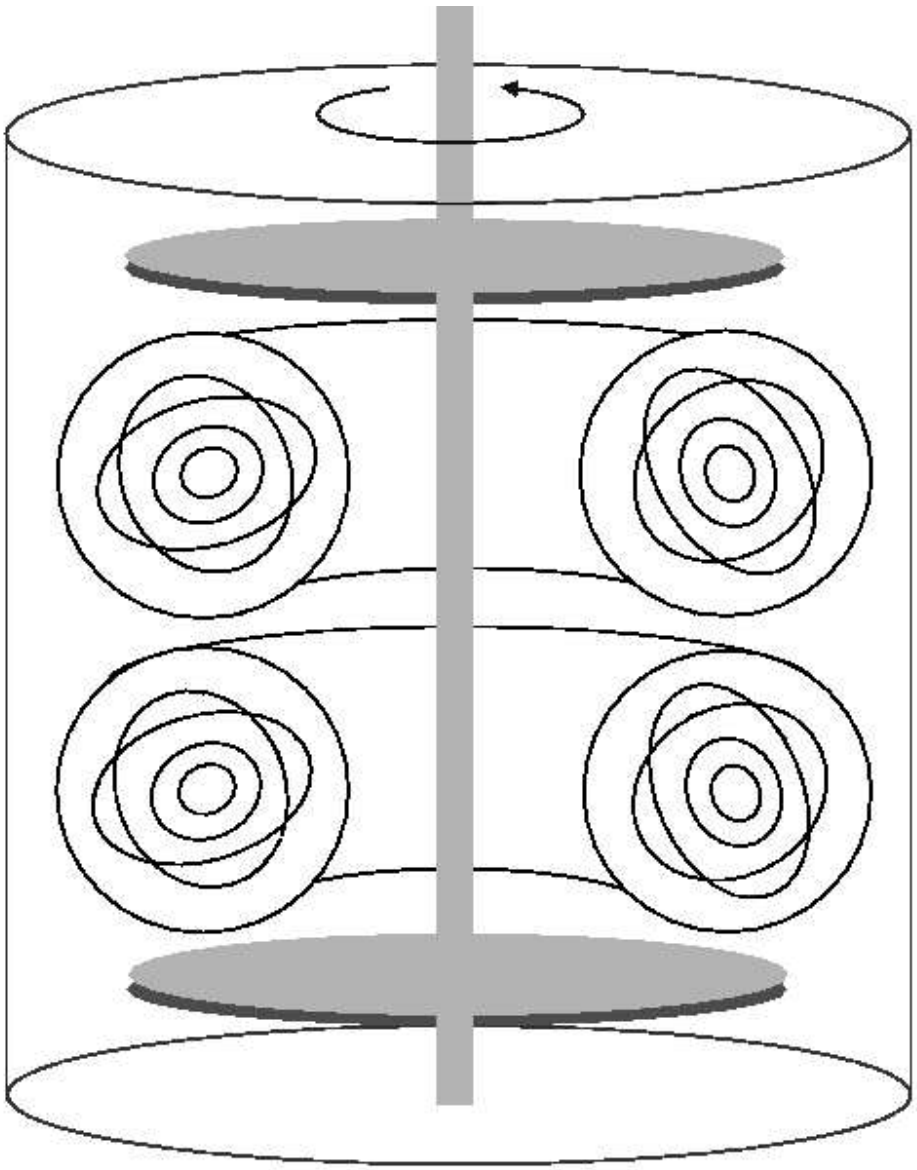

Figure 2: Schematic of mixing tank flow illustrating counter-rotating fluid tori between parallel flat-disk impellers, rotating at constant rotation rate, Ω.

of good mixing whereas others outline isolated zones. Harvey [41] analyzed mixing within a stirred tank to determine a characteristic mixing time using particle tracking methods. He concluded that in a stirred tank reactor under laminar flow conditions, the relative placement and size of adjacent impellers can be used to decrease circulation zones and increase the size of well-mixed zones.

Gauthier [42] experimentally analyzed the flow between co- and counter-rotating disks with high radius-to-spacing ratio, enclosed by a rotating cylinder. That study concluded that the instabilities which arise can yield disordered or spiraling patterns, particularly for counter-rotating disks at different rotation rates. Thus, even though the flow between parallel disks can yield secondary recirculation or cellular phenomena, the wavy instability of the Couette flow does not seem to be one of them.

Alvarez *et al.* [43] further determined that the flow within a torus can be chaotic depending on the symmetry of the flow and the rotational protocol of the impeller(s). Using both computational and experimental techniques, Fountain *et al.*., [44, 45] developed a theory for predicting regions of regularity and chaos in a 3D flow.

According to these studies, the well-ordered regular regions are centered about elliptical points (as shown in Figure 3) which are nested orbitals of decreasing radius that bear resemblance to the main torus. Fluid elements beginning near such a point will merge onto the concentric pathlines. The chaotic regions (shown in Figure 4) are characterized by the stretching and folding of fluid elements.

It follows that the chaotic regions enhance mixing since two fluid elements both beginning near such a singularity will not necessarily maintain the same path but can diverge onto separate pathlines, which is the very definition of a chaotic flow. The authors [44] called the non-chaotic regions 'islands' and theorized that these were actually closed higher-order KAM surfaces/tori which twist around the tank at a different periodicity yet remain nested within the primary toroidal flow. Figure 2 is an illustration of these concepts, depicting islands occur around elliptical points which are chained together by divergent hyperbolic points.

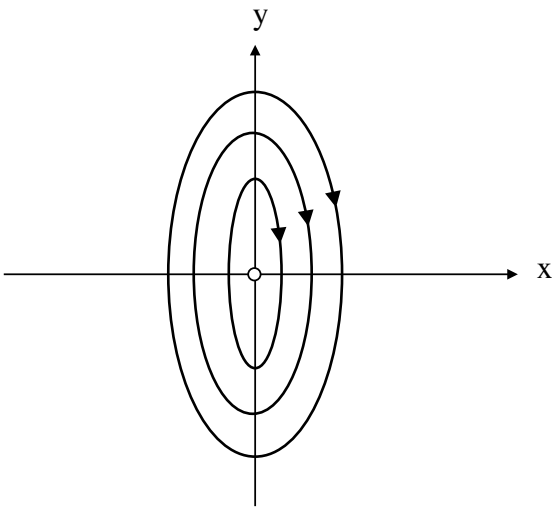

Figure 3: Convergent elliptical point [2]

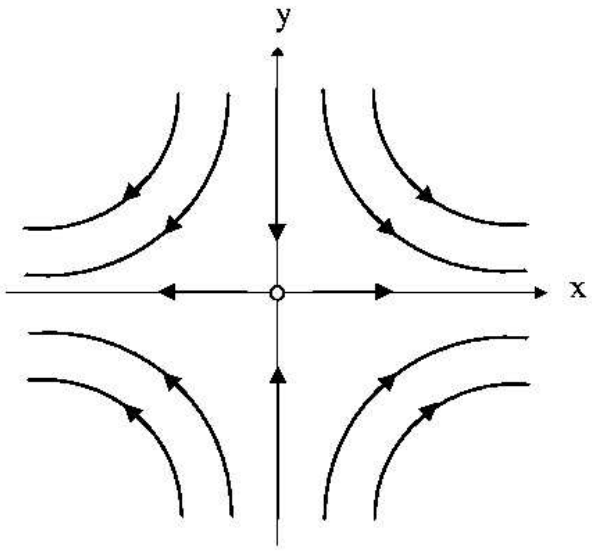

Figure 4: Divergent hyperbolic point [2]

2.1.3 Rotating Wall Vessel

The previous section illustrated the complexity in characterizing the flow field within rotating flow systems. Perhaps a simpler rotating system would be the quasi-two-dimensional Rotating Wall Vessel (RWV), also known as High Aspect Ratio Rotating Vessels (HARV) when the diameter-to-depth ratio is very large. A simple illustration of this apparatus is shown in Figure 5 (isometric view). These systems are particularly suitable for shear-sensitive applications such as the growth of endothelial tissue [46] and ovarian cell growth [47]. The cells are seeded on a spherical support which is suspended in free fall within the HARV due to the balance between centripetal. forces (towards the axis of rotation), centrifugal forces (tangential to the axis of rotation), and gravity. HARVs have also been used to achieve 3D differentiation and functionality for cells which are difficult to grow in traditional microchannel bioreactors [48] with remarkable success. Interestingly, Beigley and Kleis [49] have shown that recirculation zones can persist based on the shear environment within a traditional RWV, making this system applicable to the current study.

2.2 BASSET-BOUSSINESQ-OSEEN (BBO) EQUATION

The use of analytical and computational models can enhance the understanding of a particular system without the additional expense that experiments can sometimes require. Due to this convenience, it is beneficial to computationally examine the behavior of particles crossing the streamlines of a flow with curved streamlines, particularly as a function of buoyancy effects. This can been done by incorporating single-particle fluid interactions into a continuum-based Lagrangian advection of dilute suspensions.

As previously mentioned, our analysis is restricted to dilute systems. However, one of the complexities of a dilute multiphase flow is how to best describe the differing length scales encountered- *i.e.* on the order of the particle, or on the order of the bulk flow. There must be an understanding of forces at the non-Brownian particle scale as well as of the global steady state fluid structure, in order to understand the impact variations in these length scales can

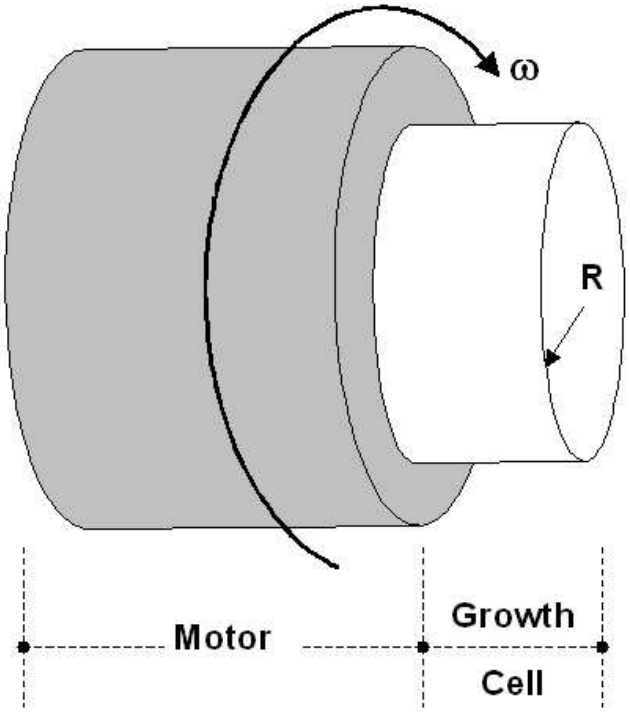

Figure 5: Isometric view of clinostat mounted on a rotating motor.

have on the equilibrium of the system. The Basset-Boussinesq-Oseen (BBO) equation is a model used to adequately capture competing effects. As shown in Equation 2.1, the BBO equation is a two-phase model which describes the motion of a single particle of constant mass and shape:

$$\begin{aligned} m_p \frac{d\mathbf{V}}{dt} &= (m_p - m_f)\mathbf{g} + m_f \frac{D\mathbf{U}}{Dt} + \frac{1}{2} m_f \frac{d\Upsilon_1}{dt} \\ &\quad + 6\pi a \mu \Upsilon_2 + 6\pi a^2 \mu \int_0^t \frac{d\Upsilon_2/d\tau}{\sqrt{\pi\nu(t-\tau)}} d\tau \end{aligned} \tag{2.1}$$

The first two terms of Equation 2.1 represent the Buoyancy force due to the density difference between particle and fluid and the Pressure force due to the shear gradient in the fluid flow. The reader should note that the shear gradient captured by the pressure term in Equation 2.1 is a function of the material or substantial derivatives of the fluid (**U**) and particle (**V**) velocities. That is:

$$\frac{D\mathbf{U}}{Dt} = \frac{\partial \mathbf{U}}{\partial t} + \mathbf{U} \cdot \nabla \mathbf{U} \quad ; \quad \frac{d\mathbf{U}}{dt} = \frac{\partial \mathbf{U}}{\partial t} + \mathbf{V} \cdot \nabla \mathbf{U} \tag{2.2}$$

The third term of Equation 2.1 captures Added Mass effects which account for the fluid mass dragged along with the particle due to a no-slip boundary condition at the particle surface. The fourth and fifth terms are the Stokes' Drag and Basset History integral respectively. The drag force is a result of the relative velocity (**U**-**V**) between the fluid and the particle at steady state, whereas the Basset history term is a form of drag due to the initial unsteady motion of a particle in a viscous fluid, or the effect of diffusion of vorticity around the sphere.

$$\Upsilon_1 = (\mathbf{U} - \mathbf{V} + \frac{1}{10} a^2 \nabla^2 \mathbf{U}) \quad ; \quad \Upsilon_2 = (\mathbf{U} - \mathbf{V} - \frac{1}{6} a^2 \nabla^2 \mathbf{U}) \tag{2.3}$$

The added mass, drag and history terms are functions of the variables Υ_1 and Υ_2, which are defined in Eqn 2.3. These expressions are in turn functions of the slip velocity (**U**-**V**) and

Faxén corrections (∇^2U terms), which account for velocity gradients or flow non-uniformity in the immediate vicinity of the particle.

As written, Equation 2.1 is not considered appropriate for capturing *Re* effects without modifications to the drag term [50] or an express account of turbulence length-scale fluctuations (for extremely large *Re*), although coefficients based on an acceleration parameter can be used [51]. Equation 2.1 is also specifically written for a single particle, thus it is inappropriate for concentrated suspensions as it cannot simulate inter-particle interactions. Nevertheless, this simple model is adequate as a first-order approximation for the continuum-based Lagrangian advection of a single solid particle, and has been used by several computational studies to incorporate particle-fluid interactions into a continuum-based Lagrangian advection of dilute suspensions. These are concisely summarized in a review by Michaelides [52].

2.2.1 Maxey-Riley Formulation

Maxey *et al.* studied the steady [3] and chaotic [53] sedimentation of aerosol particles within infinite, periodic, cellular flows. By simulating heavy particles as aerosols and light particles as bubbles, the effect of particle density was evaluated. In particular, Maxey and Riley [54] reformulated the BBO equation to represent the acceleration of a small sphere in a uniform cellular flow:

$$m_p \frac{d\mathbf{V}}{dt} = (m_p - m_f)\mathbf{g} + m_f \mathbf{U}\cdot\nabla\mathbf{U} - \frac{1}{2}m_f\left(\frac{d\mathbf{V}}{dt} - \mathbf{V}\cdot\nabla\mathbf{U}\right) + 6\pi a\mu(\mathbf{U}-\mathbf{V}) \quad (2.4)$$

The authors neglected the Basset history force by assuming any fluctuations in the flow field due to the initial motion of the particle were negligible. There is a significant body of work on the significance of the history term [52, 55]. The conclusion of these studies is that the history term gains significance only when the initial velocity of the particle is significantly different that that of the fluid, as in the case of very light particles. The asymptotic positions of slightly non-neutrally buoyant particles with an initial relative velocity of zero are of primary interest, thus the history term was also neglected in this work.

2.2.2 Lateral Lift Force

Past studies of rotating flows often assumed the particles are both far from neighboring boundaries and small enough that lateral migration (lift) forces may be neglected. For larger non-Brownian particles, however, lift terms play an important role in the transverse motion of particles [52, 51]. Saffman [31, 56] conducted research on the motion of a particle in a pressure-driven pipe flow which resulted in the so-called Saffman lift force presented in Equation 2.5. This force arises from an induced rotation due to a velocity gradient across the particle, and is perpendicular to the direction of translation [57].

$$F_L = 6.46a^2(\mu\rho_p)^{\frac{1}{2}}|\nabla \times \mathbf{U}|^{\frac{1}{2}}[(\mathbf{U}-\mathbf{V}) \times (\nabla \times \mathbf{U})] \tag{2.5}$$

Stone [29] and others [28, 30] subsequently summarized that for low to moderate Reynolds number flows, this force could yield a drift of particles across fluid streamlines since it is perpendicular to the direction of translation (due to the net direction of the slip velocity). For non-Brownian particles, even a neutrally buoyant particle can move relative to the local fluid if there is a gradient of pressure across the particle surface, as Segre . The effect of particle spin about its own axis would produce a lateral lift and aid migration at small but finite values of Re [58, 59], such that the slip-velocity Reynolds number (Re_s) should be much less than the shear Reynolds number (Re_G) which should then be less than unity. That is:

$$Re_s = \frac{\rho_p a|\mathbf{U}-\mathbf{V}|}{\mu} \quad << \quad Re_G = \frac{\rho_f a^2|\nabla \times \mathbf{U}|}{\mu} \quad < \quad 1 \tag{2.6}$$

Maintaining this inequality ensures that the vorticity of the flow ($\nabla \times \mathbf{U}$) is small thus the problem is still within a laminar Stokes flow regime. This means the form drag used in the BBO model is still applicable. There are other forms of the lift term available, [32, 34, 60, 61] which are extensions of Saffman's work and are applicable for higher Re flow systems.

The lift force is perpendicular to the direction of flow, thus a particle moving faster than the bulk flow will migrate *away* from regions of higher fluid velocity, whereas a particle lagging behind the bulk flow will move *towards* regions of higher fluid velocity [60, 57].

Extensions of this work have resulted in expressions valid for deformable particles such as droplets/bubbles, at more relaxed limits on *Re* [59, 62].

Coimbra and others [1, 55, 61] have studied the relative importance of the forces represented in the BBO equation in various flows. Following rigorous mathematical derivations, they present different forms of the Lift, Added Mass and Basset History terms. For the simple HARV shown in Figure 6 (front view), Ramirez *et al.* [1] showed that within the limits on *Re* shown in Eqn 2.6 result in the lift force being dominant over pressure effects. Since these two centripet al. forces point in opposite directions, the resulting radial balance was outwards. When Eqn 2.6 was not satisfied, the particle diverged from any equilibrium position; however when the particle *Re* was less than that of the fluid, one of the quadrants contained the asymptotic location of the particle.

These researchers emphasize the necessity of the history term, especially in the migration of particles significantly lighter than the continuous phase. They also determine that the local shear magnitude (determined by the rotation rate of the apparatus) on the particle decreases as the particle *Re* decreases, allowing an equilibrium position closer to the center of a rotating flow. Thus, for a counterclockwise rotation of the HARV, the flow domain could be divided into the four quadrants shown in Figure 6 (front view), which represent the possible equilibrium positions for non-neutrally buoyant particles. The schematic illustrates that the direction of the forces used in the Ramirez study – pressure (F_P), drag (F_D), lift (F_L) and buoyancy (F_B) – change direction based on which quadrant the particle is in due to the motion of the HARV and the particle properties such as density (which affects the buoyancy term). A particle would find an equilibrium location within this flow field when these body forces canceled each other to a net zero effect.

2.3 COMPUTATIONAL FLUID DYNAMICS (CFD)

Studies have increasingly included numerical models based on Computational Fluid Dynamics (CFD), a well-known modeling technique that treats the fluid according to continuum mechanics principles. FLUENT© is a CFD modeling package which is routinely used to cap-

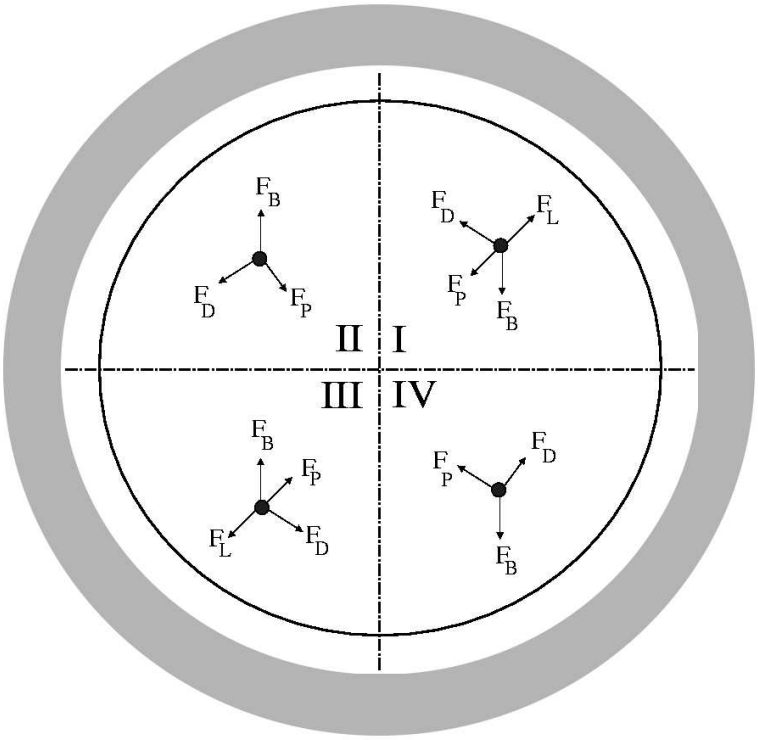

Figure 6: Front view of clinostat illustrating the force distribution in different quadrants according to Ramirez *et al.* [1], for counterclockwise rotation at constant ω.

ture fluid mechanics of various apparatus such as the stirred tank apparatus. This particular tool has also been used to evaluate the motion of large particles in mixers and filters [63] by incorporating a Discrete Phase Model (DPM) which is able to solve the equations of motion for coupled fluid and granular phase systems. Others [44] have also used this tool to evaluate the effect of the shaft tilt-angle in a single impeller stirred tank on the fluid island structures. The primary use of CFD as it relates to this study is to determine the velocity distribution within the stirred tank particularly as a function of asymmetry. This is discussed further in chapter 4.

2.3.1 Cellular Flow Streamfunctions

Maxey and Riley [54] simulated the acceleration of a small sphere using the BBO model (Equation 2.4). Equation 2.7 was used to simulate a two-dimensional rotating flow made up of concentric trajectories of decreasing radius, as shown in Figure 7. Stommel [64] first proposed this streamfunction to examine the entrapment of small particles (e.g. plankton) in oceanographic vortices.

$$\psi(x,y) = U_o L sin(\frac{2\pi x}{L}) sin(\frac{2\pi y}{L}) \tag{2.7}$$

The authors ignored the Faxén corrections by assuming the particle was sufficiently small such that any flow non-uniformity at the length scale of the particle was negligible. A series of counter-rotating cells were used to create the flow fields shown in Figures 8 and 9, illustrating the differences in sedimentation patterns for various initial particle positions.

Maxey and Riley also defined a *capture radius*, *i.e.* a particle trajectory described by an overall balance of the competing forces. Without the lift force, the model used in this study also predicts that neutrally buoyant particles would migrate to such an orbital and maintain a constant radial position. Lighter particles would stay on a closed circular path, or migrate towards the center of a cell. In contrast, heavier particles in a cellular flow spiral outward due to dominant buoyancy effects.

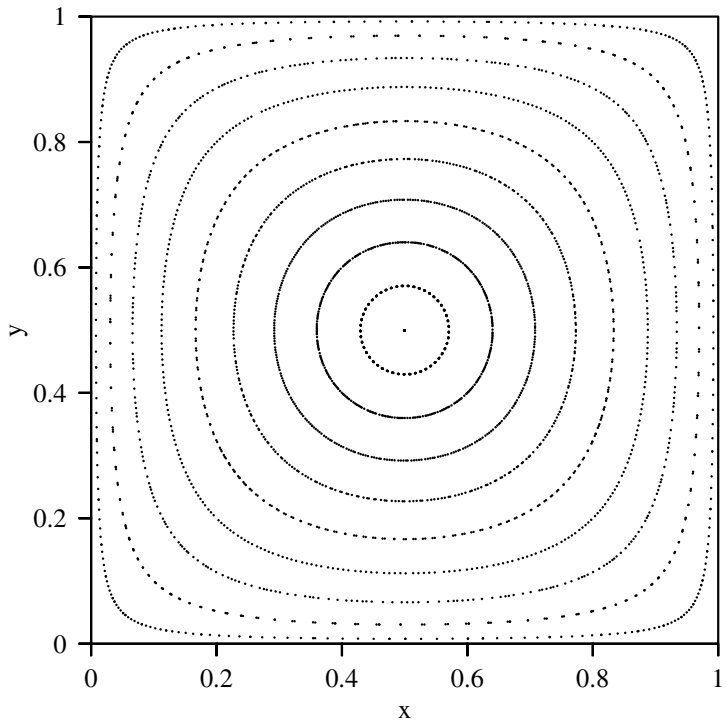

Figure 7: Concentric streamlines within a regular cellular flow as a function of initial (x,y) position. Fluid elements follow these streamlines in a clockwise motion.

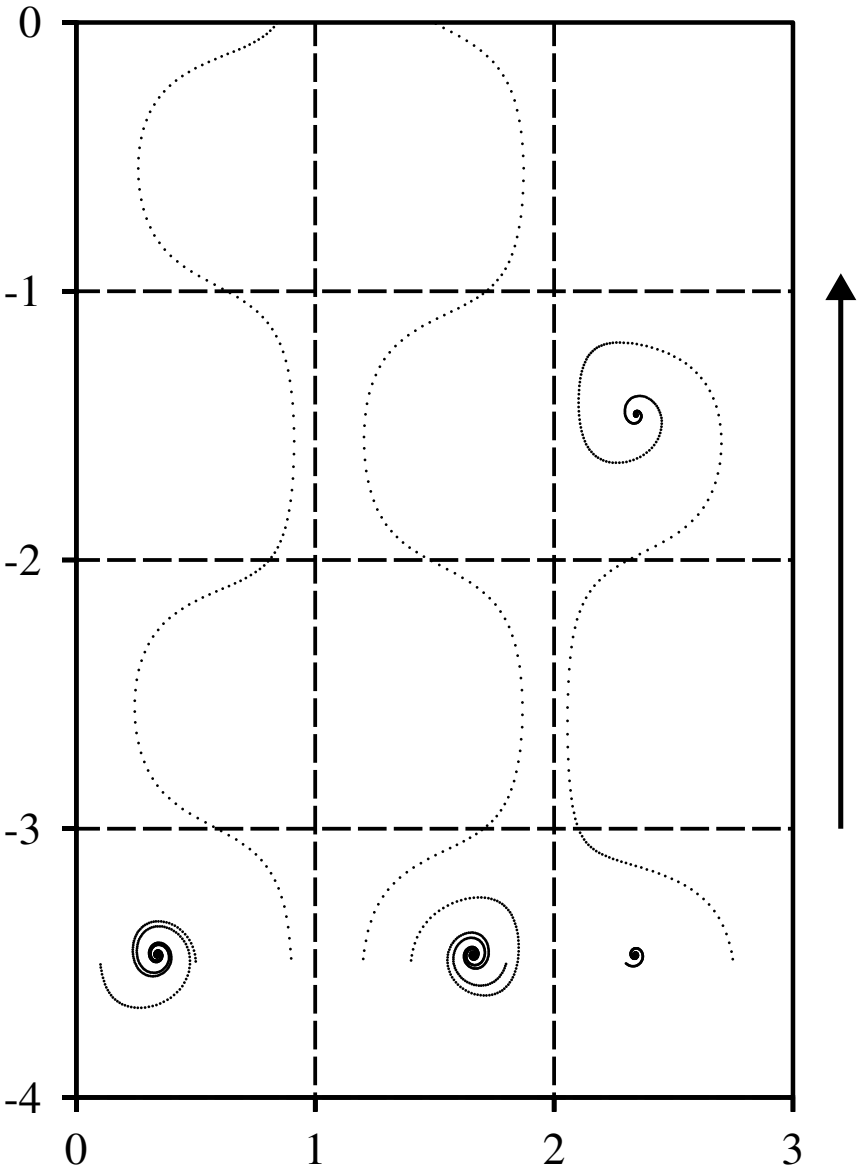

Figure 8: Trajectories of *light* particles (bubbles) ascending within a cellular flow field according to Maxey and Riley [3]; arrow shows direction of sedimentation. Initial positions are (0.1,-3.5), (0.5,-3.5), (0.9,-3.5), (1.4,-3.5), (1.2,-3.5), (1.8,-3.5), (2.3,-3.5) and (2.75,-3.5).

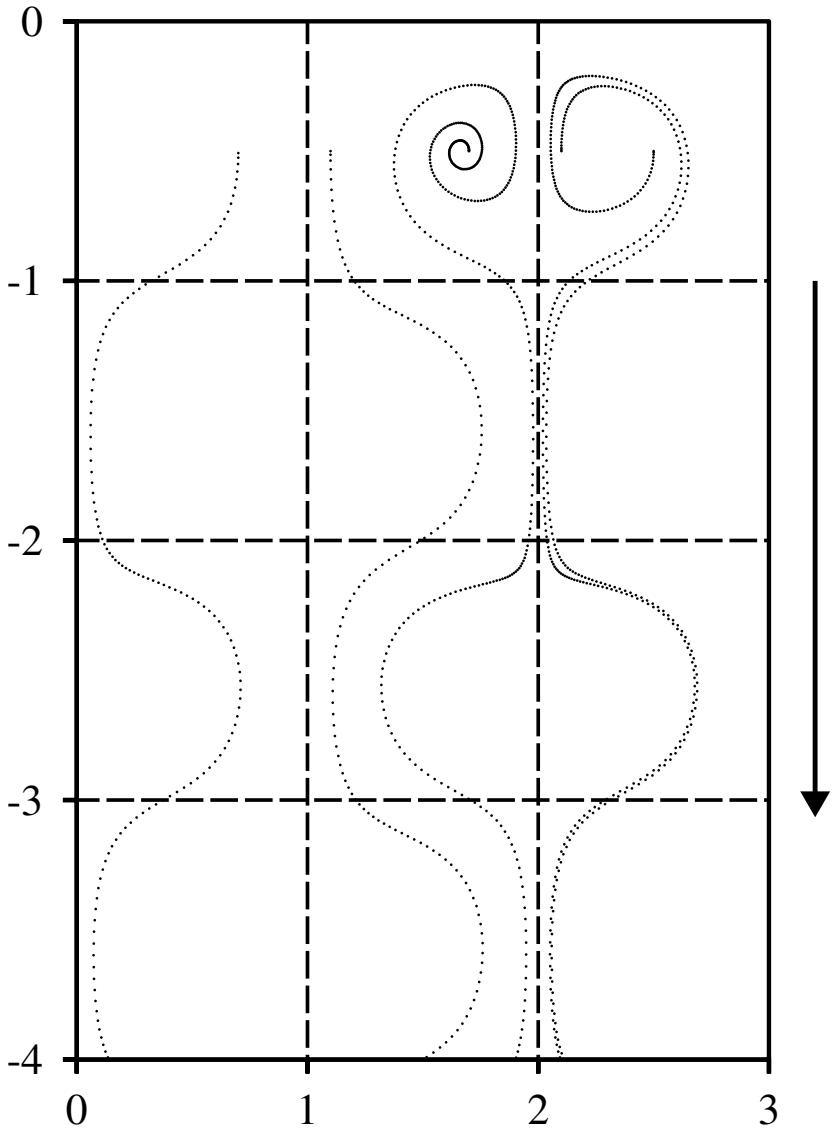

Figure 9: Trajectories of *heavy* particles (aerosol droplets) settling under gravity within a cellular flow field according to Maxey and Riley [3]; arrow shows direction of sedimentation. Initial positions are (0.7,0.5), (1.1,0.5), (1.7,0.5), (2.1,0.5) and (2.5,0.5).

Figure 8 shows sedimentation patterns for light bubbles. Five particles spiral into a stable attractive location within the cellular flow; two others rise out of the initial cell and rise upwards within the flow. A final bubble also rises upwards, but finds a stable location in another cell within the flow. In contrast, the heavy aerosol droplets in Figure 9 migrate away from the stable locations, irrespective of initial positions. It is interesting to note that the trajectories of two of the heavy particles actually merge and are eventually indistinguishable in subsequent cells. The key feature of these results is that non-neutrally buoyant particles (*i.e.*, of differing density than the continuous phase) have exhibited very different behavior than merely tracing out the flow streamlines of Figure 7.

Incompressible flow systems are adequately described by a trigonometric streamfunction of two spatial variables [65, 66, 67], which can then be made periodic with the addition of small, non-integrable perturbations [68]. This has been used to model various physical phenomena, from the orientation and stability of celestial bodies several times larger than the earth [69, 70, 71] to the growth of microscopic mammalian cells [1] within bioreactors. Such perturbations will be necessary to investigate the motion of non-Brownian particles within the fluid island structures found in stirred tank systems, as discussed in section 2.1.

3.0 MIGRATION IN A STIRRED TANK

As previously discussed, rotating viscous flows are known to contain regions of chaos and regions of regularity. This section details experimental observations of non-neutrally buoyant spherical particles migrating across flow streamlines to such regular locations within the toroidal flow between parallel flat disks at small but finite Reynolds numbers. Our focus is on dilute systems, thus the analysis can be restricted to an individual particle.

The co-axial stirred tank geometry used in this work represents a simple three-dimensional closed flow system where fluid drag may be used to counteract gravitational settling. By choosing a finite-sized cylindrical mixing tank, competition between centrifugal buoyancy forces, wall interactions and non-linear hydrodynamics as a function of the local shear environment can be evaluated. As will be shown, this balance results in repeatable asymptotic locations within the flow. Moreover, the underlying mixing tendency of the flow – which can be made almost globally chaotic – plays a significant role in the migration behavior.

In all experiments, the continuous phase is glycerin with a specific gravity (S.G.) of 1.26, whereas the slightly non-neutrally buoyant particles are either acrylic (S.G.=1.14) or cellulose acetate (S.G.=1.30) beads, 1.6mm or 2mm in diameter. Based on the density differences, the particles are identified as *light*, *i.e.*, density is slightly smaller than glycerin; or *heavy*, *i.e.* density is slightly greater than glycerin. The particles are large enough such that thermal fluctuations on the order of a fluid element (Brownian motion) are considered to have negligible effect on individual particle trajectories. The particle size, impeller spacing and rotation rate of the shaft are independent parameters which were varied to characterize the particle migration rates and equilibrium positions.

3.1 EXPERIMENTAL PROCEDURE

A 1500 ml simple mixing tank (made from clear cast acrylic cylinders purchased from McMaster-Carr) is placed within a square tank also made of acrylic as shown in Figure 10. This outer tank is sealed and also filled with glycerin which has been index-matched to acrylic using small amounts of sodium iodide (NaI) to reduce the effects of tank curvature. The inner cylindrical tank is then filled with fresh glycerin which is pumped in through the bottom of the apparatus using a Simon fluid pump. Bubbles which formed while pumping the glycerin into the tank were allowed to rise naturally as the glycerin 'sat' overnight. Due to the hygroscopic nature of glycerin, however, the tank was covered with wax paper so that there is minimum absorption of water from the atmosphere and therefore minimum change in the fluid viscosity.

The moving apparatus – multiple 3 inch (38.1 mm) diameter flat-disk impellers equidistantly spaced along an axial shaft – are placed into the tank and locked into a bronze 2-bolt flange mount in the bottom of the tank and connected to the top metallic shaft rotated by a motor. This dual anchor helped to stabilize the shaft during rotation. To maintain some uniformity in initial positions, two particles of differing density were placed between adjacent impellers and allowed to sediment- heavy particles sinking to the bottom disk and light particles floating to rest against the top disk. The laser sheet is then aligned with the shaft and impellers such that a cross-section of the tank is illuminated, and a CCD camera is placed directly perpendicular to this laser sheet. The entire setup – showing the laser, the illuminated flow and the camera placed perpendicular to the illuminated laser sheet – can be seen in Figure 11.

3.2 FLOW VISUALIZATION

When the shaft and impellers are rotated, invariant fluid tori form between impellers. They are separated by Kolmogorov-Arnold-Moser (KAM) surfaces such that they are isolated from the outside flow and other tori except through molecular diffusion. Glycerin loaded

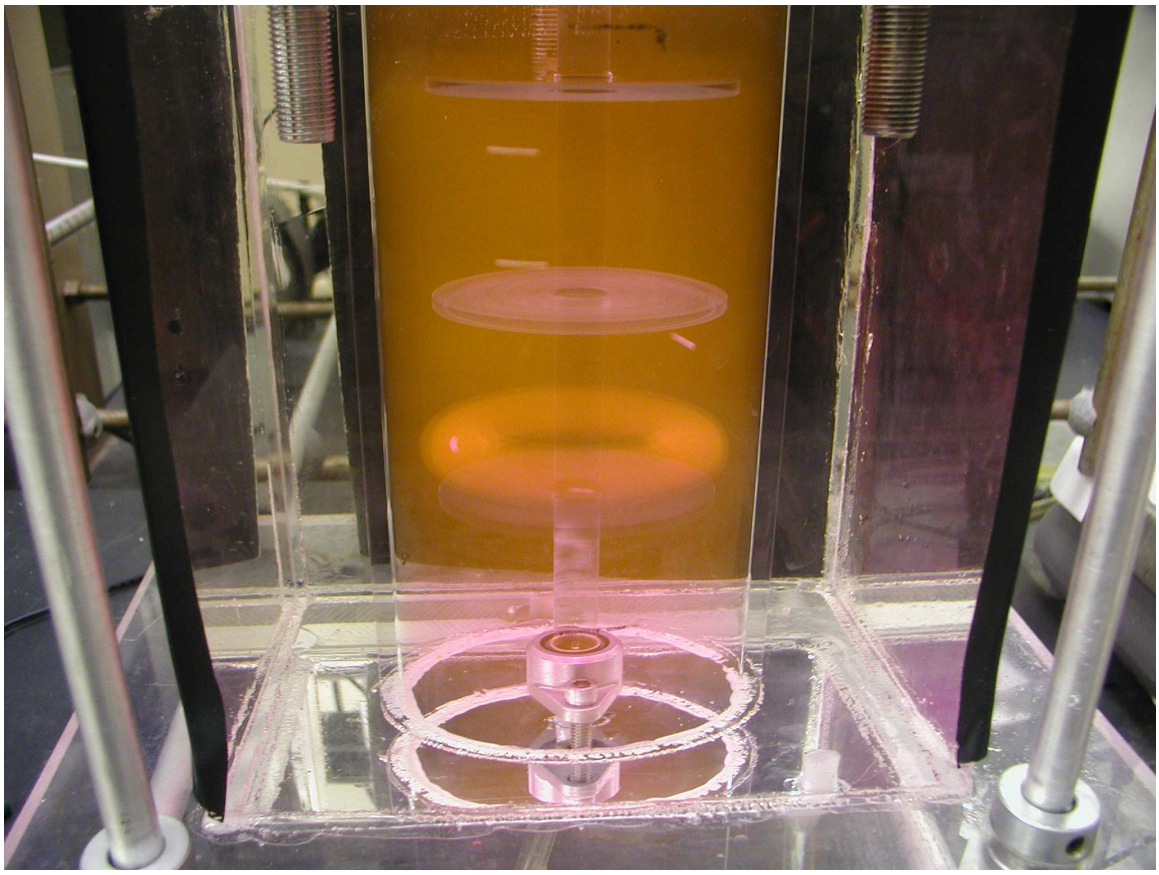

Figure 10: Experimental setup showing positioning of cylindrical tank within larger square acrylic box for refractive index matching. The white streaks are particles migrating within the toroidal flow.

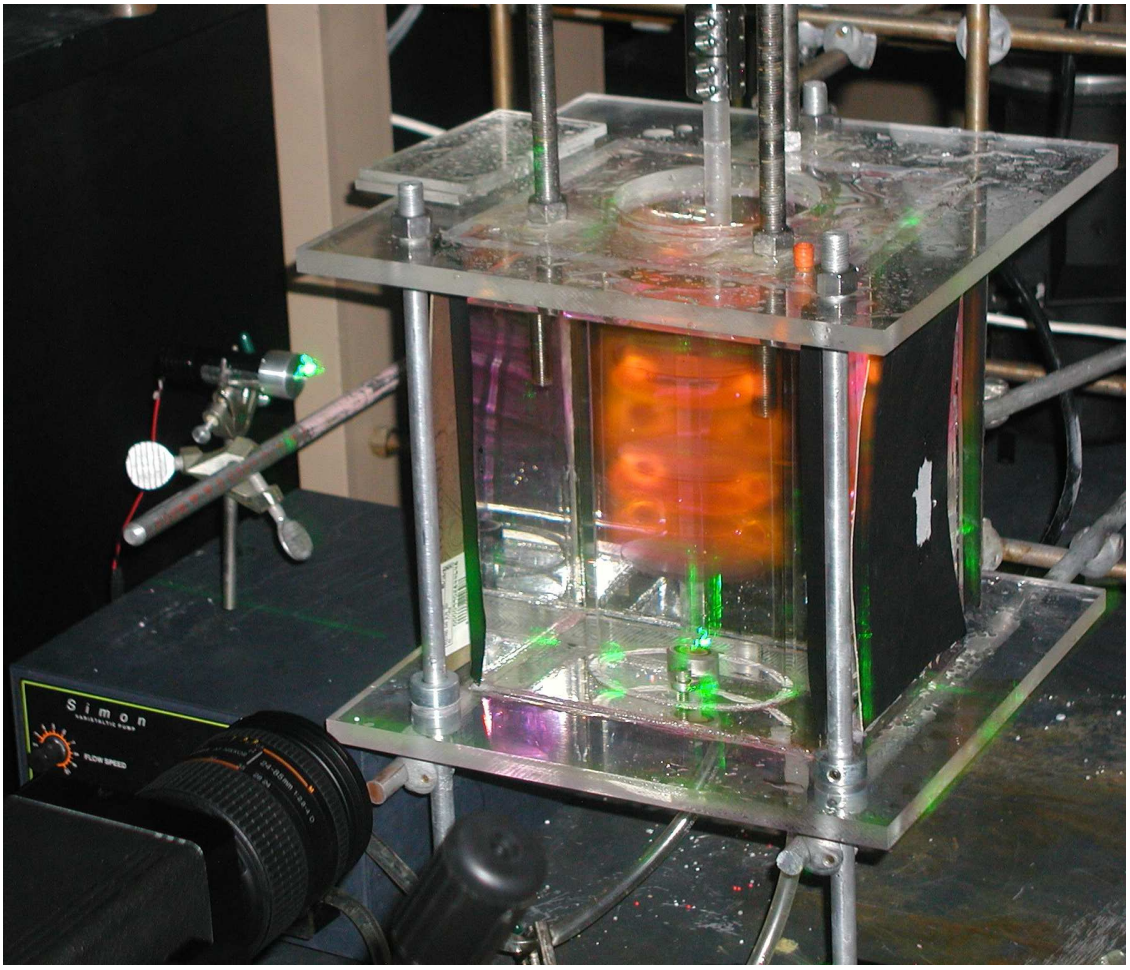

Figure 11: Experimental setup showing laser and camera (perpendicular to laser sheet) positions. With ambient lighting, one can see the tori as well as the laser cross-section.

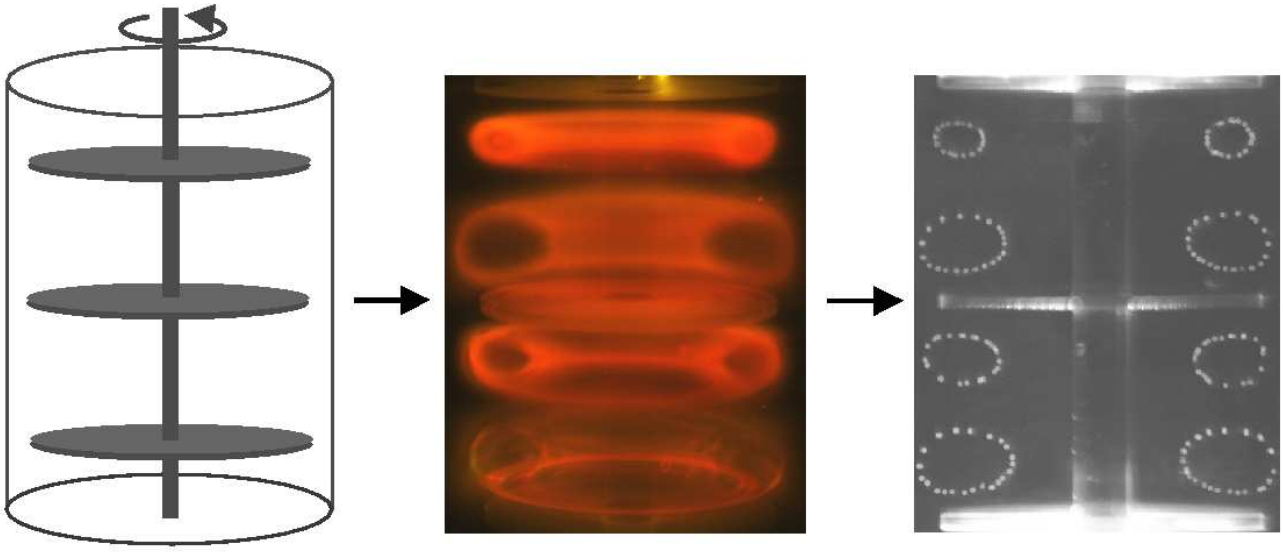

(a) (b) (c)

Figure 12: (a) Mixing tank geometry; (b) snapshot of fluid tori that form between adjacent impellers; (c) 60-second exposure of 2mm particles tracing out cellular orbitals within the fluid tori.

with Rhodamin B dye (which fluoresces orange) is injected into the flow to visualize the tori, as shown in Figure 12b. The different sizes of the tori could be considered a function of the direction of gravity and any opposing force. For the upper torus between a set of impellers, the motion of the top impeller flinging fluid back into that structure is mostly downward in the same direction as gravity. For the lower torus, the bottom impeller recirculates fluid back into that structure in a direction counter to gravity. This difference might explain the dilation of the top torus relative to the bottom structure.

A 532 nm wavelength laser diode (purchased from Edmunds Industrial Optics) is equipped with a beam splitter used to illuminate a 2D cross-section of the tank. When particles are introduced into the steady state flow, the CCD camera placed perpendicular to the laser sheet is used to create stroboscopic maps of the particle location each time it crosses the two-dimensional plane. Multiple crossings are captured within the same frame by using long

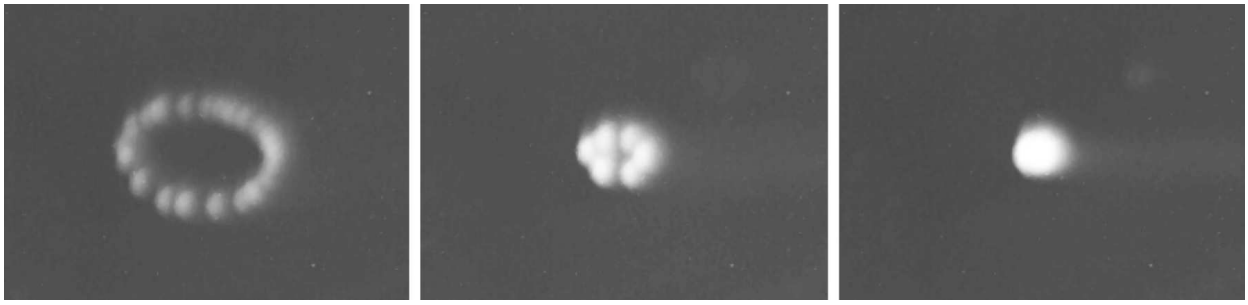

Figure 13: Experimental snapshots depict migration progress of a single particle at (a) 30min, (b) 60min and (c) 90min time intervals.

exposure times, creating experimental Poincaré sections of the particle motion within individual cells. Figure 12c is an example of such toroidal cross-sections, where the exposure time is 60 seconds with approximately 20 particle crossings in each snapshot. This experimental snapshot is of four particles tracing out cellular orbitals at a rotation rate of 80rpm and with a 2-in impeller spacing.

3.3 TRIVIAL EQUILIBRIA

Subsequent sections present the monotonic migration of non-neutrally buoyant particles within the previously described simple mixing tank (Figure 12).

3.3.1 Decreasing Cellular Trajectories

Previous computational work [3, 15] on the migration of very small particles within a cellular flow predicted that particles less dense than the continuous fluid phase moved inward toward the cell center, whereas more dense particles moved outward. In contrast, an inward migration for *both* heavier and lighter particles is observed in the experiments reported here.

The experimental snapshots of Figure 13 show typical circular trajectories for the monotonic inward migration of the particles. As the particle moves further within the cellular flow, the size of the circular path (*i.e.*, the radius of the particle orbital) decreases.

3.3.2 Particle Size Effects

A quantitative measure of the rate of migration for each particle can be made by plotting the radial position of the particles as a function of time. Figure 14 is a plot of the typical radial position vs. time for 1.6mm and 2mm particles at 60rpm. The reader should note that open symbols represent particles lighter than the fluid whereas closed/filled symbols represent particles heavier than the fluid for figures in the chapter.

Plotting the data on a log-log scale allows the comparison of the rate of migration for different densities and particle sizes. The smaller 1.6mm particles migrate inwards at a slower rate than the 2mm particles, as evidenced by the steeper curves of the larger particles. However, the difference between light and heavy particles also becomes less noticeable as the size of the particle increases. The migration rates of the light and heavy particles are relatively similar, especially for the 2mm particles. This is likely due to the fact that the particles are both within 10 percent difference from the density of glycerin. In theory, as the particle size decreases, it approaches the size of a fluid particle which is merely following streamlines of the flow. Thus deviations due to particle size would be more pronounced as the size increases. In these experiments, deviation from fluid behavior is characterized by increased rate or extent of migration.

3.3.3 Effects of Rotation Rate and Impeller Spacing

Changes in the distance between adjacent impellers and the impeller rotation rate affect the local shear environment within the tori and, therefore, the rate at which particles migrate within the flow. The cell width (defined as the tank wall-to-shaft distance) is kept constant and used to non-dimensionalize the radial position of the particle as it migrates within the cross-sectional cellular flow. The cell height (defined as half of the disk-to-disk distance) changes as the spacing between adjacent impellers is varied from 2-4 inches (5.08-10.16cm).

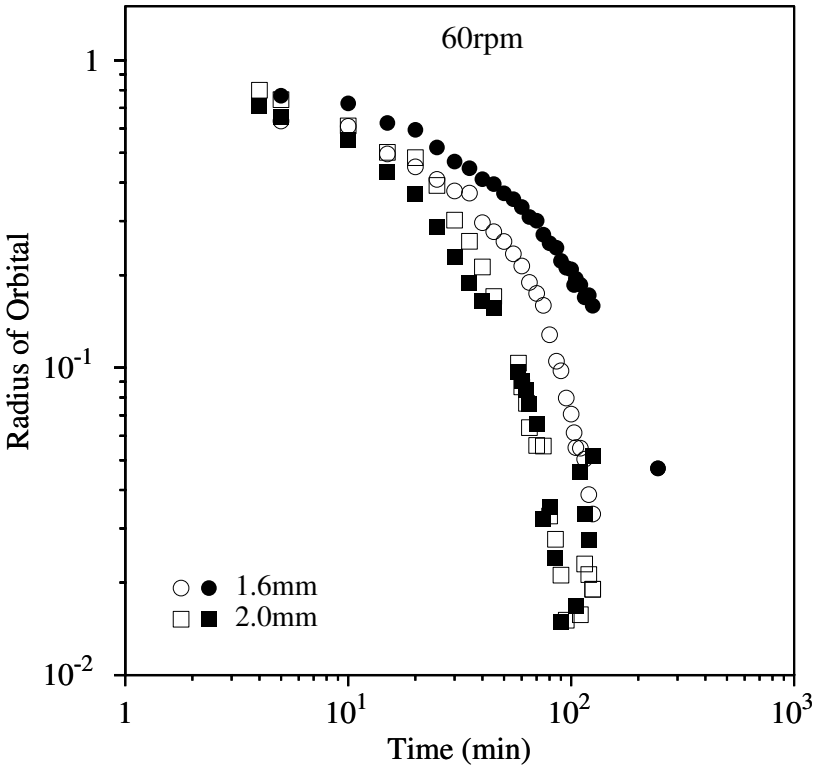

Figure 14: Representative migration rates at 60rpm for a 2-inch spacing. The smaller 1.6mm particles (○, ●) migrate at a slower rate relative to the larger 2mm spheres.

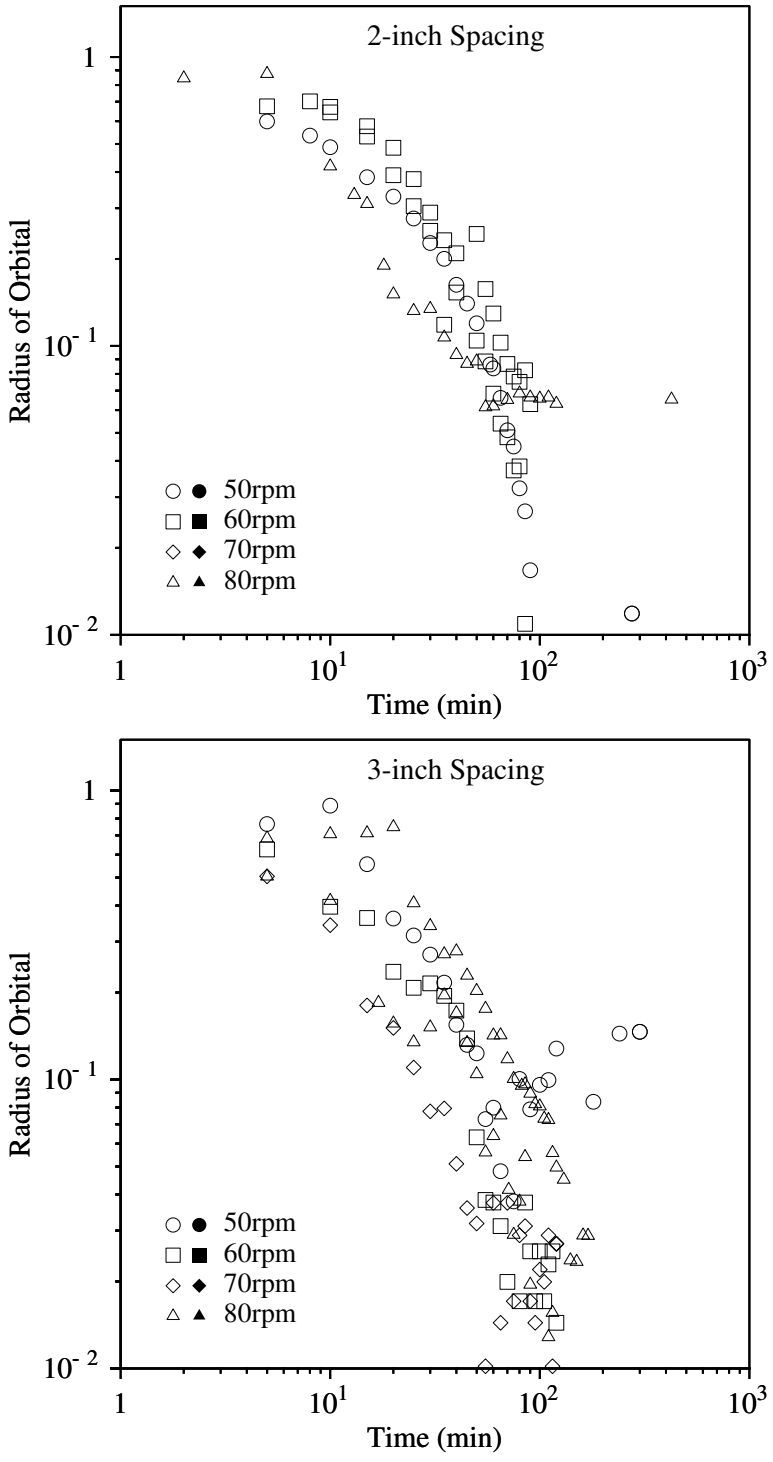

Figure 15: Radial position for light 2mm particles as a function of time at different rotation rates (50-80rpm) and impeller spacings (2-3 inches).

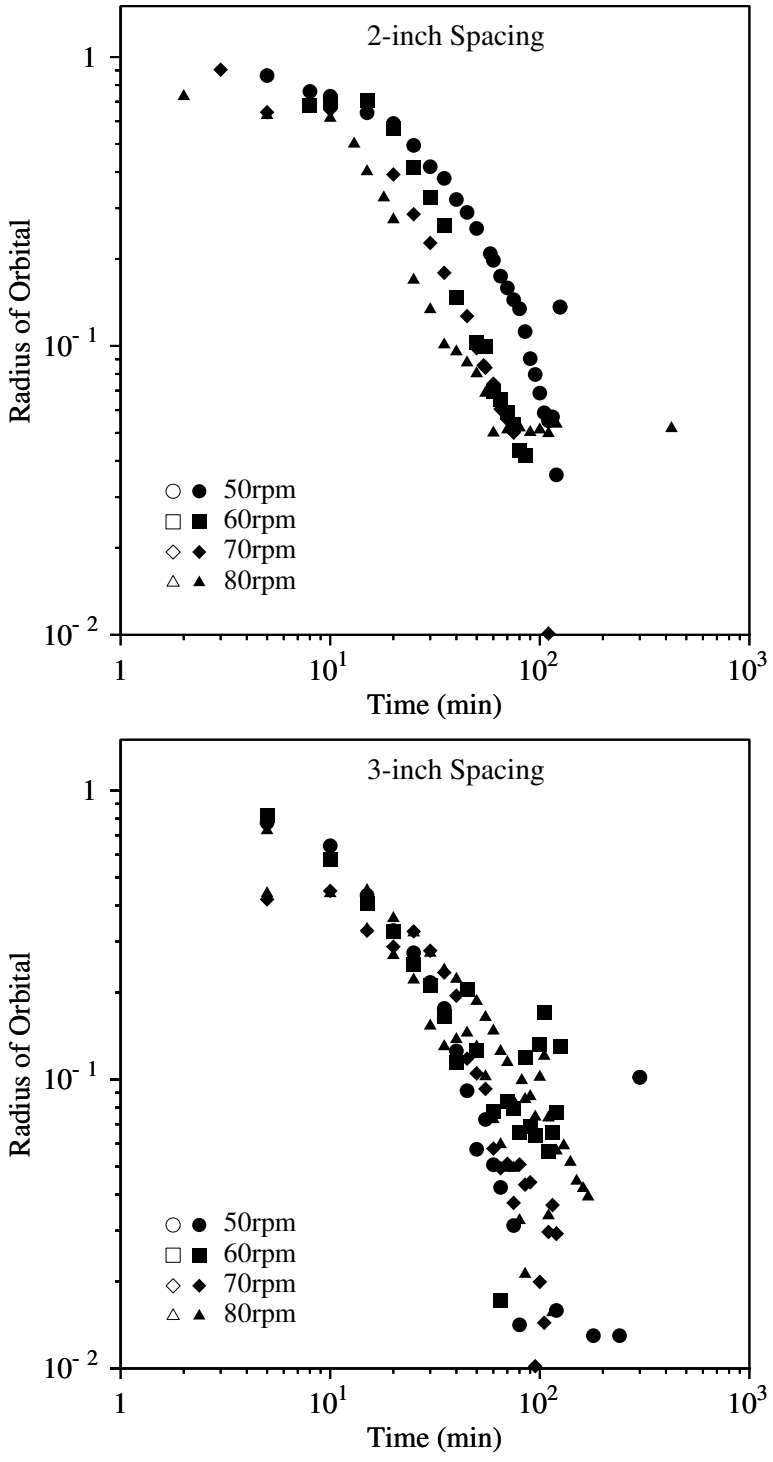

Figure 16: Radial position for heavy 2mm particles as a function of time at different rotation rates (50-80rpm) and impeller spacings (2-3 inches).

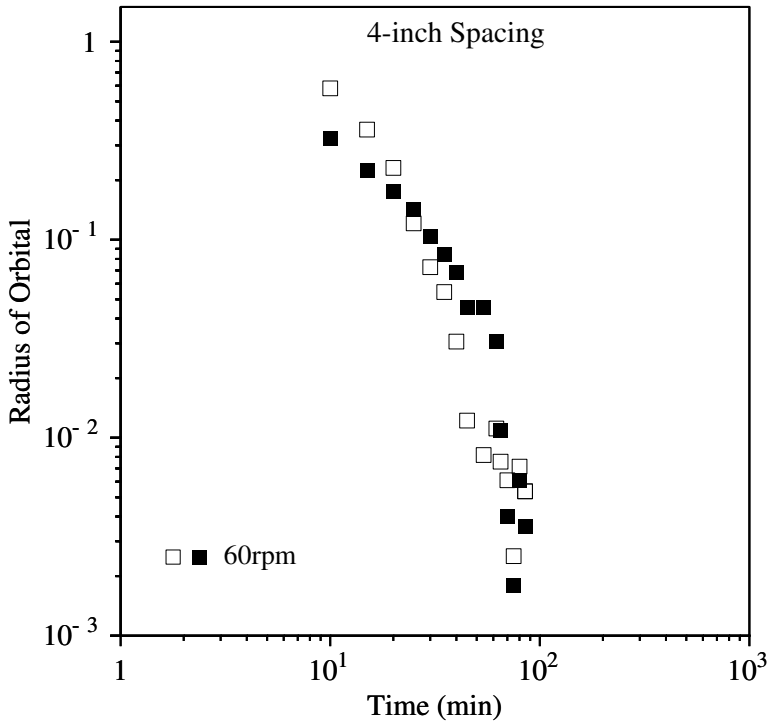

Figure 17: Radial position for light and heavy 2mm particles as a function of time at 60rpm for a 4-inch impeller spacing.

The spacing between adjacent parallel disks impacts the size and symmetry of the toroidal structures. For the 2-inch spacing, the tori are relatively symmetric as the ratio of cell height:width was approximately 1:1, with an increasing loss of symmetry for the 3-inch (1:1.5) and 4-inch (1:2) spacings. Figures 15 and 16 show this data at different rotation rates for both lighter and heavier 2mm slightly non-neutrally buoyant particles. The same data also seems to show an increase in migration rate with impeller spacing, requiring at least 90min for the migration to the torus center (time-axis) for the 2-inch spacing vs. 60min for the 3-inch spacing experiments.

The inward migration was also confirmed for the 4-inch spacing, as shown in Figure 17. It would seem that as the impeller/shaft rotation rate increases, the rate of migration increases correspondingly, although this dependence is not as clear to identify as the effect of spacing.

3.4 NON-TRIVIAL EQUILIBRIA

As previously stated, particles typically trace out relatively circular paths while gradually spiraling inwards within the fluid torus. For some particles, however, the crossings occur at the same radial positions creating 'clusters'. That is, for prolonged periods of time, the particle continuously crosses the 2D plane in a small number of discrete locations and inward migration ceases.

The center of the cell/torus is designated as a period 1 cluster, *i.e.*, all particle crossings occur at a single location. In a similar manner, a period n cluster means that the particle crosses the 2D plane in n discrete locations. It is worth noting that the formations are observed for both the acrylic (light) and cellulose acetate (heavy) particles.

The inset snapshots in Figures 18 and 19 illustrate the particle orbital at the times indicated as well as some of the various patterns observed. Recall each snapshot contains roughly 20 particle crossings; open symbols represent light particles and closed/filled symbols represent heavy particles.

3.4.1 Cluster Formations

At 50rpm, inward migration is seen until the particles reach a period 6 formation for the 3-inch spacing (Figure 18a) and a period 4 formation for the 2-inch spacing (Figure 18b). The 60rpm plot displays a period 5 formation for the 2-inch spacing (Figure 18c) and a period 4 formation for the 3-inch spacing (Figure 18d). However, the shape and radial position of these clusters are at a higher radial position than for the 50rpm data (see Table 1).

For the 70rpm plot, two different period 4 formations are observed in Figure 19a and 19b. Figure 19a especially bears resemblance to the period 4 cluster observed at 60rpm in Figure 18d. However, a quasi-stable period 5 formation (Figure 19c) is also seen for approximately 25 minutes before the particle migrates further inward and stalls in a period 4 formation similar to the other particles. A different period 5 formation was also seen for a 3-inch spacing at 70rpm (as detailed in Table 1). This was maintained for approximately 35min, and its structure was a tilted variation of Figure 19c. At 80rpm, the slope of the curves monotonically decrease when the particle crossings are distinct and separate, as seen in Figure 19d. In contrast, the curves level off when the particle crossings cluster into a period 3 formations (Figure 19e) and the particle migration stalled.

For the particle and flow conditions studied, it would seem that the stability of the clusters is highly dependent on rotation rate and impeller spacing. When the particle exhibits cluster formations, low-period stable clusters are generally observed at lower radial positions with increased rotation rate; for example, period 5 clusters at 60rpm vs. period 3 clusters at 80rpm.

An increase in impeller spacing also seems to yield lower-period formations, for example, period 5 clusters for a 2-inch spacing vs. period 4 for a 3-inch spacing at 60rpm (see Table 1). From these results, it would seem that the radial position also increases since the higher-order clusters are located further away from the cell center.

3.4.2 Adjacent Tori Comparison

The migration patterns of particles within the tori between adjacent impellers is very similar even when the particles are dissimilar. Figure 20 shows the similar patterns for both a heavy

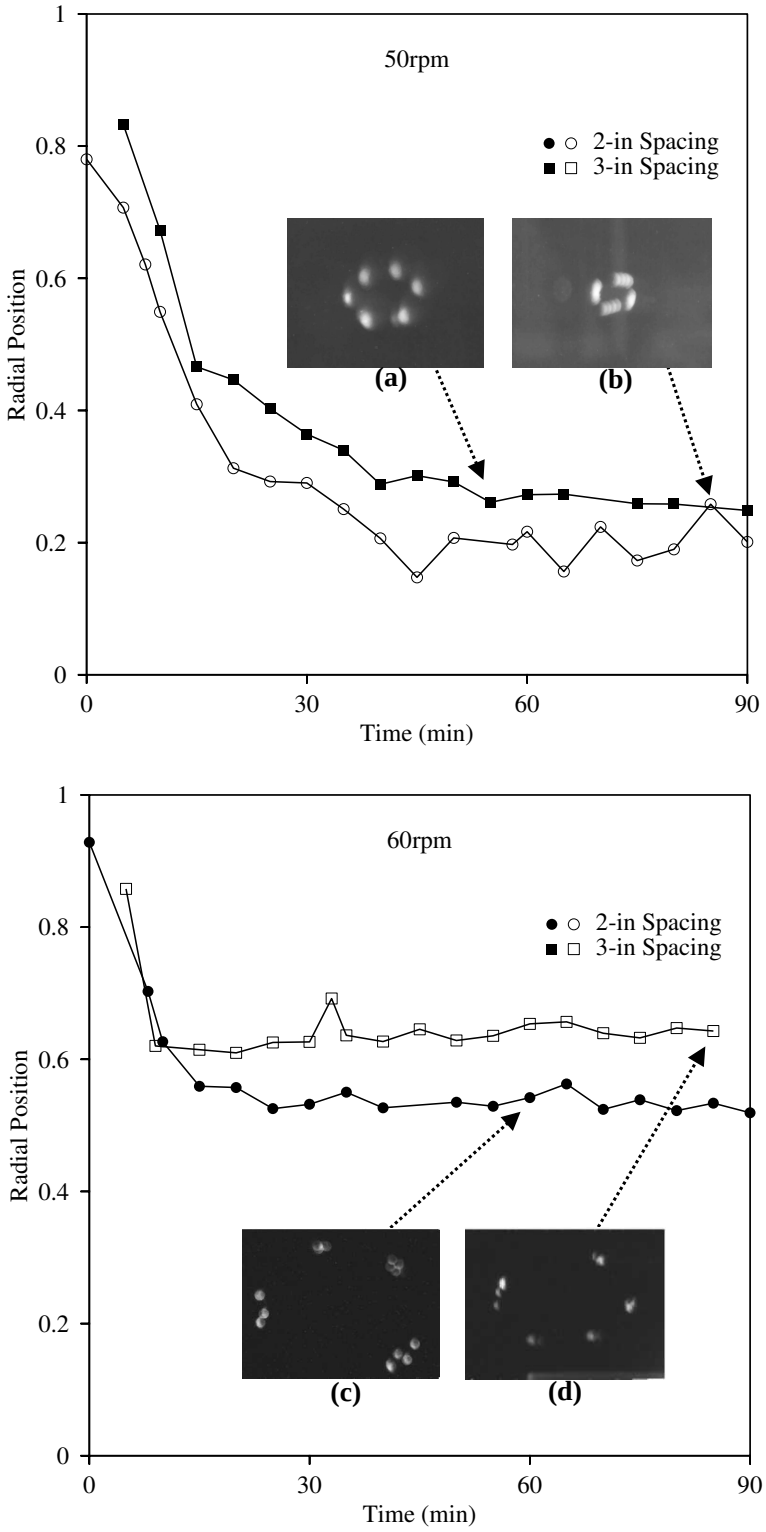

Figure 18: Radial particle positions, illustrating linear progression until clusters are formed. Inset snapshots illustrate: (a) 50rpm, 2-in spacing, period 6; (b) 50rpm, 3-in spacing, period 4; (c) 60rpm, 3-in spacing, period 5; (d) 60rpm, 2-in spacing, period 4.

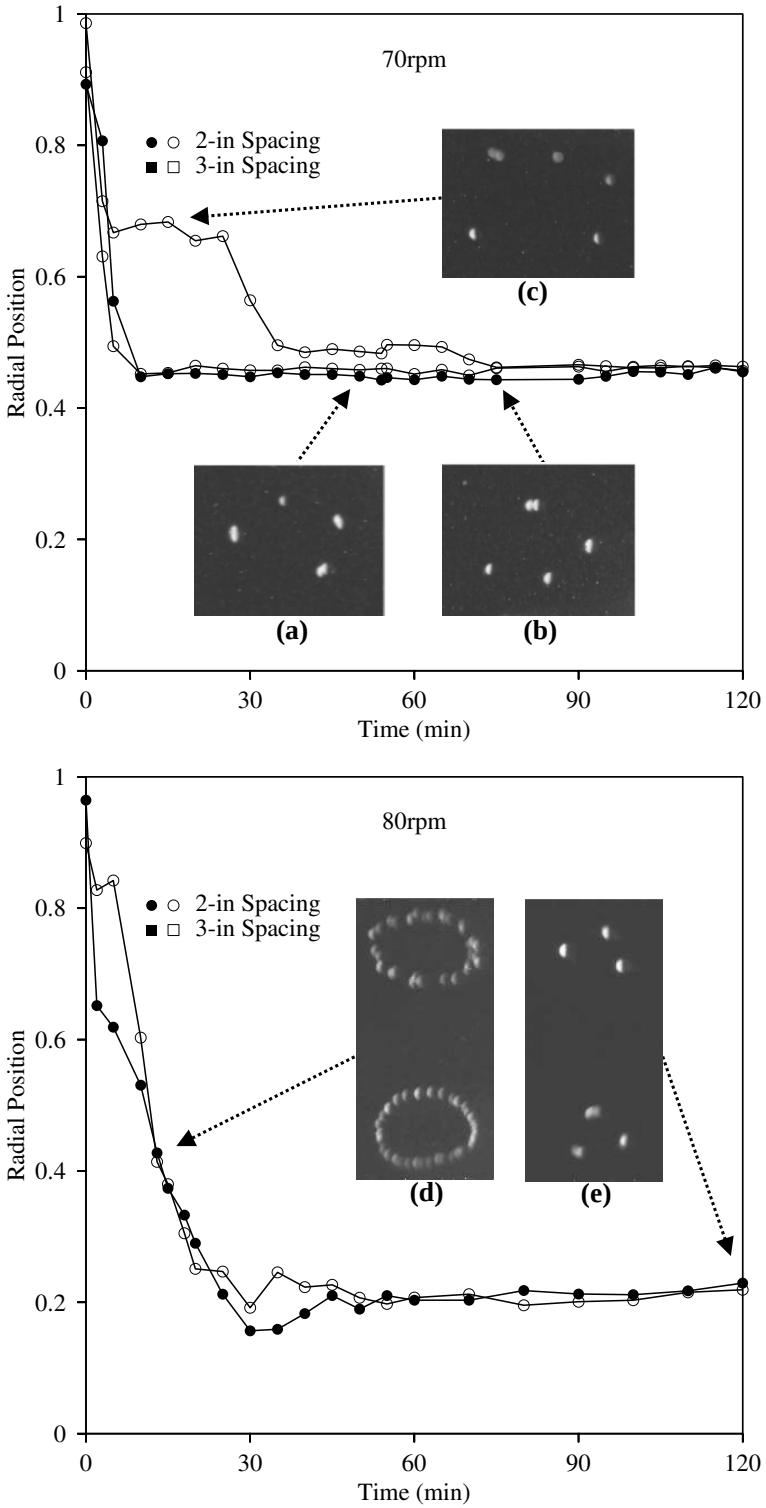

Figure 19: Radial particle positions. (a-b) 70rpm, 2-in spacing, period 4; (c) 70rpm, 2-spacing, period 5 (quasi-stable at this rotation rate); (d) 80rpm, 2-in spacing, regular crossings; (e) 80rpm, 2-in spacing, period 3 for both a light (top) and heavy (bottom) particle.

Table 1: Periodicity of particle clusters for 2- and 3-inch spacing as a function of rotation rate. **Note-* the period 5 cluster observed at 70rpm (radius=0.61) was seen for ∼35min; others were stable for the duration of the experiments.

	2-inch spacing		**3-inch spacing**	
RPM	*Clusters*	*Radius*	*Clusters*	*Radius*
50	6	0.25	4	0.20
60	5	0.55	4	0.65
70	4	0.45	5	0.61*
80	3	0.20	-	-

and light particle of the same size. When the particles are not stalled, the cellular orbitals traced by the top light particle and the bottom heavy particle are very similar, even as the crossings begin to cluster. When the particles stall into a period 4 formation, the shape of the island formations are similar, but rotated with respect to one another. This is the primary manner in which the tori differ- in the direction of rotation. However, the rate at which particles migrate within the tori are similar even when snapped at different angles of rotation.

3.4.3 Nested KAM surfaces

To clarify the effect of the mixing on the particle motion, dye-advection experiments were performed using Rhodamin B fluorescent dye. This required injection of the dye further into the toroidal structures to highlight any secondary structures present, such as the period 6 island chain highlighted seen in Figure 21. It should be noted that the presence of a needle acts as a perturbation of the flow, thus the experiments were continued and the flow allowed to re-settle to steady state. Even with the perturbation of the flow structure, period 3 islands are readily identified.

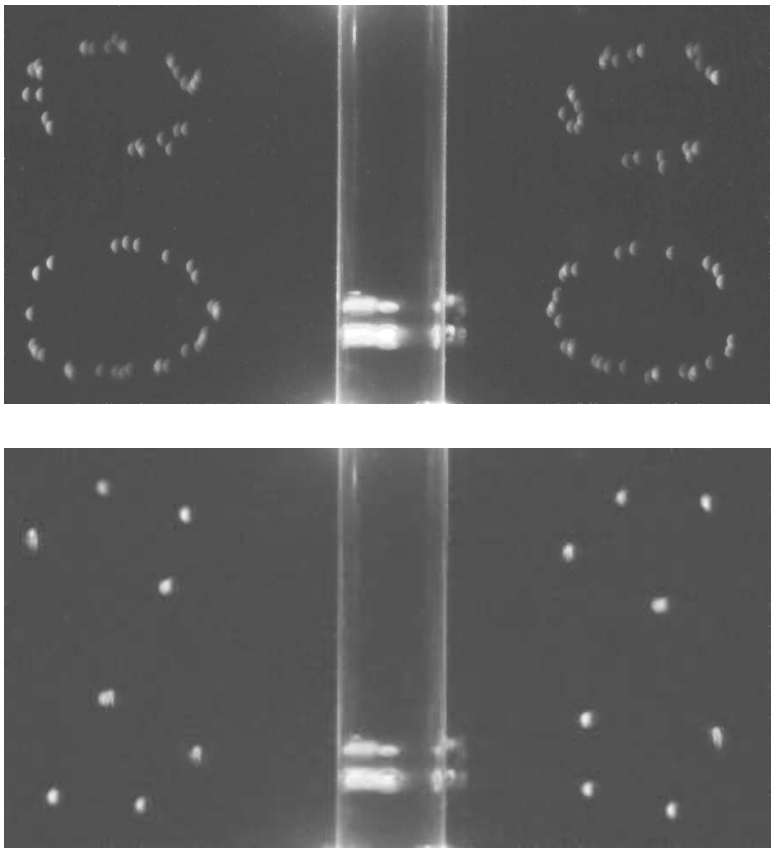

Figure 20: Monotonic (top) and period 4 (bottom) migration in adjacent tori at 70rpm. The white bars on the shaft are due to glare from the laser.

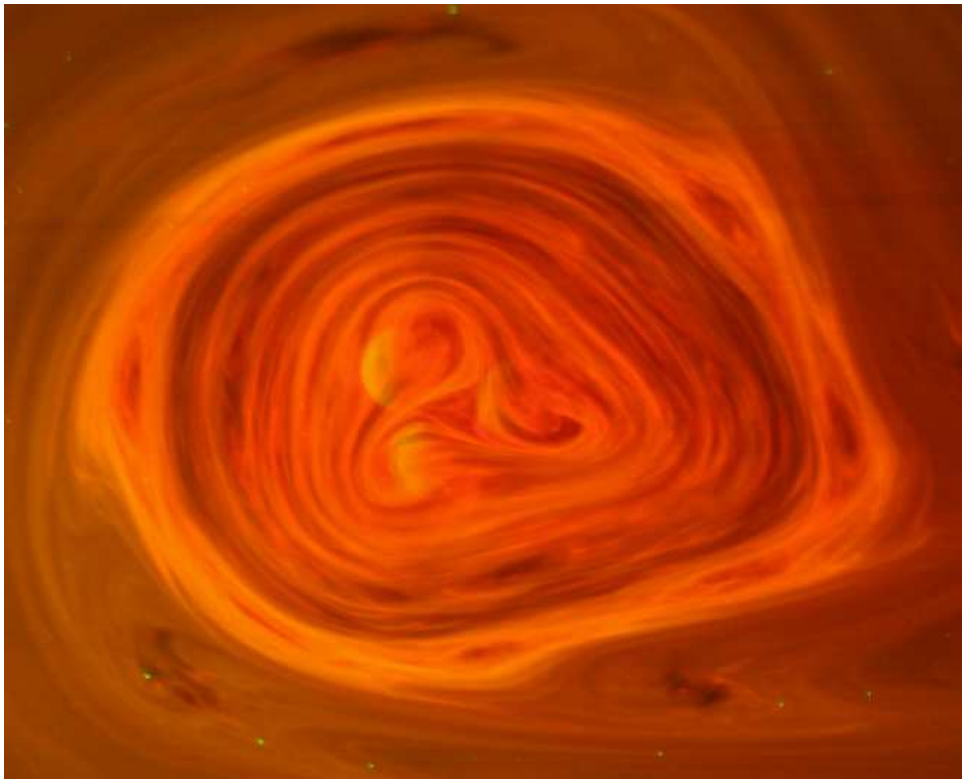

Figure 21: Complex inner structure of toroidal flow just after injection of Rhodamin B fluorescent dye dissolved in glycerin.

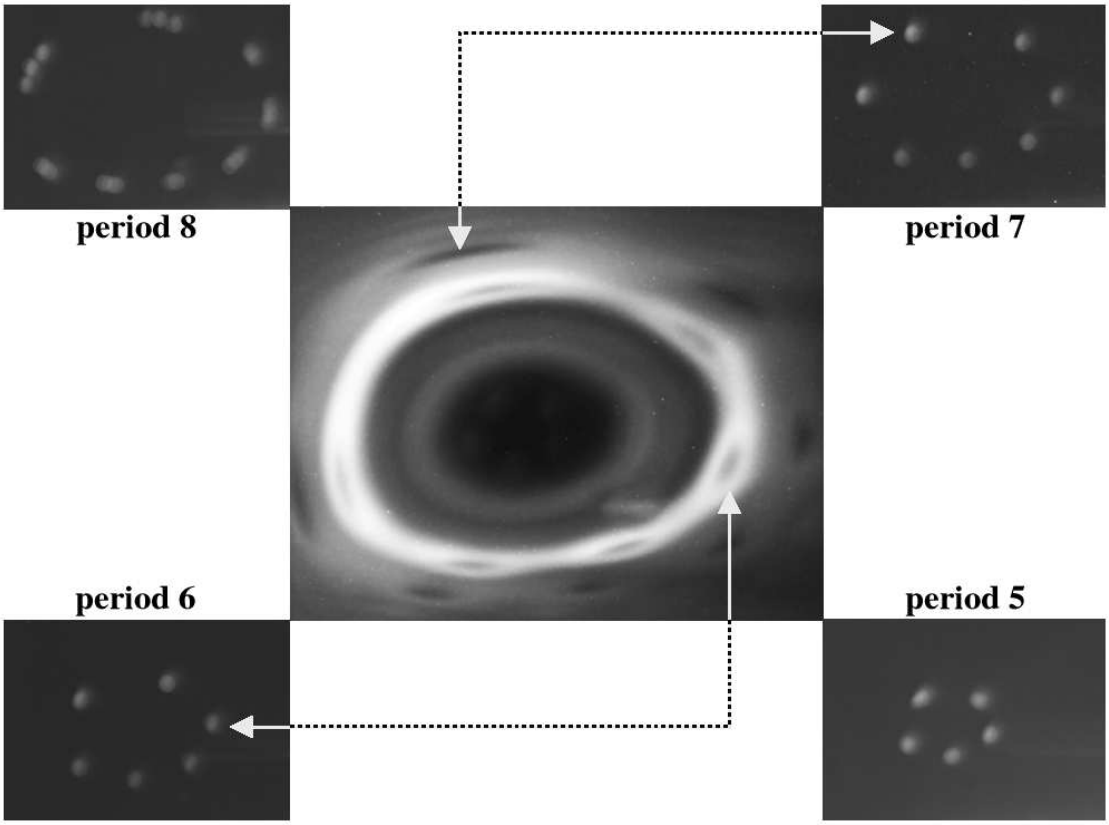

Figure 22: Higher-order cluster formations for both light and heavy particles, and the nested fluid islands which cause the stalling behavior.

Figure 22 illustrates both period 6 and 7 island chains within the same flow, as well as the corresponding particle migration clusters of the same periodicity at 60rpm. The period 5 and 8 clusters are shown for completion. The highlighted period 7 chained structure is the counterpart to that observed in Figure 21 at equilibrium. These experiments show that the chaotic flow is made up of nested island chains of decreasing periodicity as one moves towards the center of the fluid torus.

Figure 23 is a closeup of one of the island chains for both the fluid (top) and particle (bottom). Close inspection of the period 4 structure also shows nested concentric tori/KAM surfaces. This is a typical feature of invariant KAM surfaces [65]; *i.e.*, magnification of any one of the islands would yield the same island structure replicated *ad infinitum*. The corresponding particle islands show a clustering of particle positions as the particle traces out the internal structure of the islands.

The top snapshot in Figure 23 also physically illustrates the concepts of elliptical and hyperbolic points discussed in section 2. The fluid islands can clearly be seen to resemble the elliptical point schematically shown in Figure 3, and the pinched areas between the islands would correspond to the hyperbolic points of Figure 4. The bottom snapshot then shown the tracing out of the fluid islands that occurs when a particle interacts with this fluid structure. Thus, even as the particle migrates inwards within the primary toroidal flow, there is also a spiral around the fluid islands with which it interacts, before the crossings coalesce into one location.

Figure 24 combines dye advection and particle migration to further illustrate that the locations of these clustered crossings seem to exactly coincide with regular regions (islands) within the chaotic flow, as suggested in Figure 22 and Figure 23. The particle crossings remain discrete (separated) when the particle is outside of these islands, yet are clustered in these periodic islands when the particle is stalled within the previously-mentioned KAM tubes or higher-order islands. The period 3 islands in Figure 24c closely mirror the 80rpm experiment in Figure 19. It would seem that migration mechanisms dominate in the well-mixed regions of the primary flow, thus the observed particle motion is monotonic. In contrast, in regions where the isolated fluid islands are stable, the migration is thwarted and the motion of the particles is halted in the various cluster formations shown.

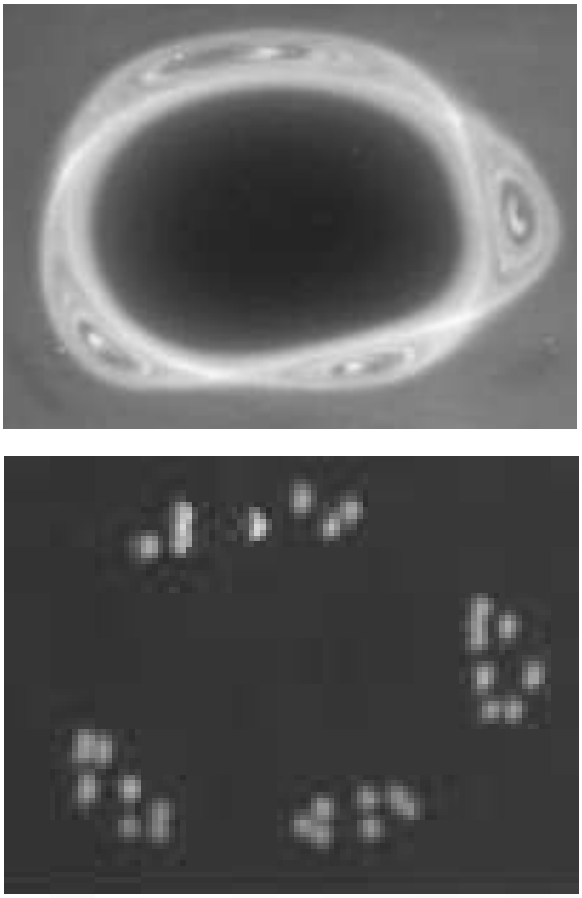

Figure 23: (Top) Closeup of period 4 fluid islands at 80rpm showing the repeated KAM surfaces within the islands. (Bottom) A different 80rpm experiment without dye showing 2mm heavy particles tracing out the same period 4 islands before clustering to single crossings.

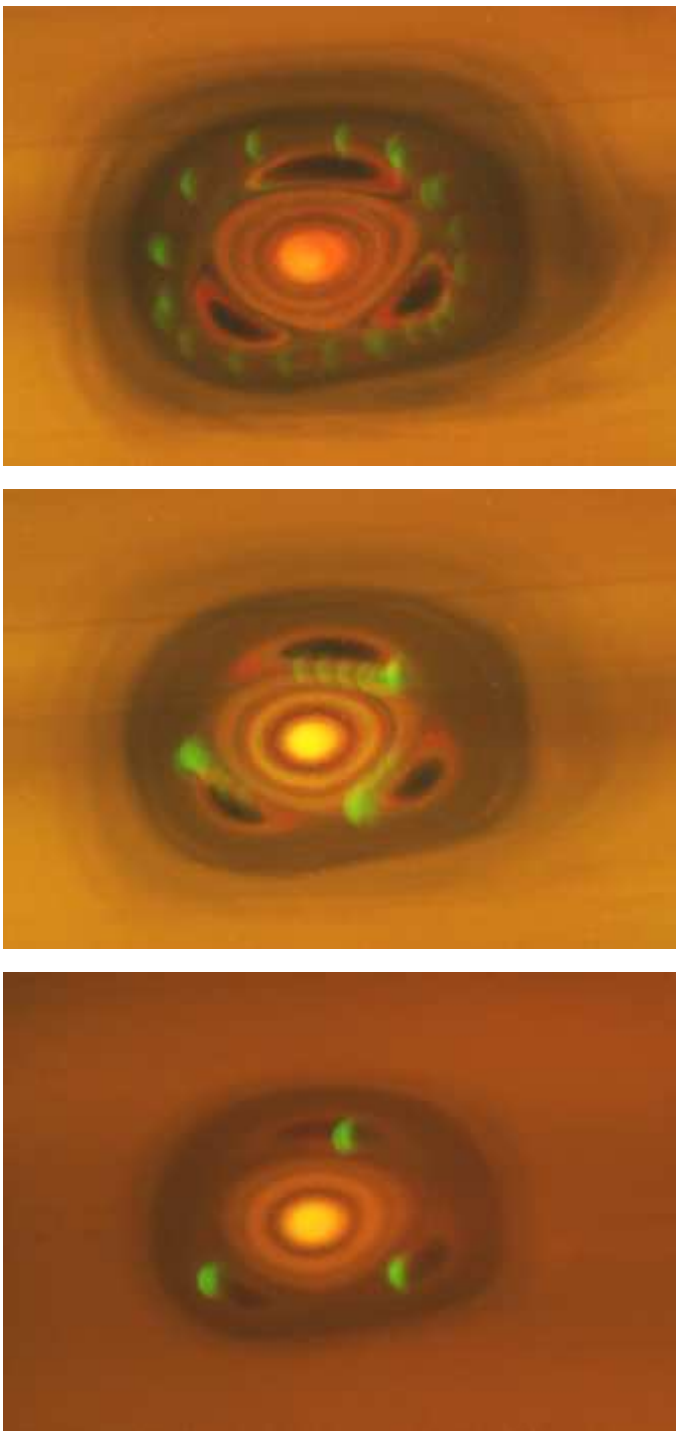

Figure 24: Dye advection snapshots of a heavy particle at 80rpm: (a) linear migration when the particle is between KAM surfaces; (b) interaction with the KAM tube which manifests as a clustering of particle positions in the 2D laser sheet; (c) particle is trapped within the fluid islands, creating a period 3 cluster.

3.5 MULTI-PARTICLE COMPETITION

The addition of a second particle forces the spheres to 'compete' for the asymptotic positions. The 70 and 80rpm plots in Figure 25 compare the progress of two heavy particles with that of a single heavy particle.

Both particles occupy the same circular path at the beginning of the 70rpm experiment. However, one particle overcomes the centrifugal forces and migrates inward, whereas the other maintains an outer orbital (Figure 25a). Closer examination of the radial positions shows that the motion of the *inner* particle is similar to that of a single particle experiment at the same rotation rate. In contrast, the *outer* particle stalls at a radial position $\simeq 0.55$, as though its ability to move inward towards a period 1 position are hindered by the inner particle's presence (Figure 25b).

Cluster formation is still observed for competing particles. The 80rpm plot of Figure 25 shows the outer particle clearly tracing out a period 4 formation (Figure 25c) for approximately 10 minutes of the experiment, even as the inner particle remains discrete and monotonic in its migration. Eventually, the migration paths of both particles merge into a single cellular orbital (Figure 25d).

As more particles are added, the flow system moves away from the dilute suspension limit and individual particle paths are much less discernible. Also, with more concentrated systems, it is difficult to discern whether the secondary structures are preserved or compare individual particle rates of migration. Figure 26 shows the progression of a multi-particle suspension within the stirred tank flow. With time, the cloud of particles becomes smaller as the spheres migrate further within the tori.

Again, although there is a visual difference in the 'cloud density' between top and bottom tori in the pictures, this did not translate into quantitative differences in the migration rate of single particles within adjacent tori. Rather, it is a function of the underlying fluid structure itself as seen from the laser fluorescence sequence in Figure 12.

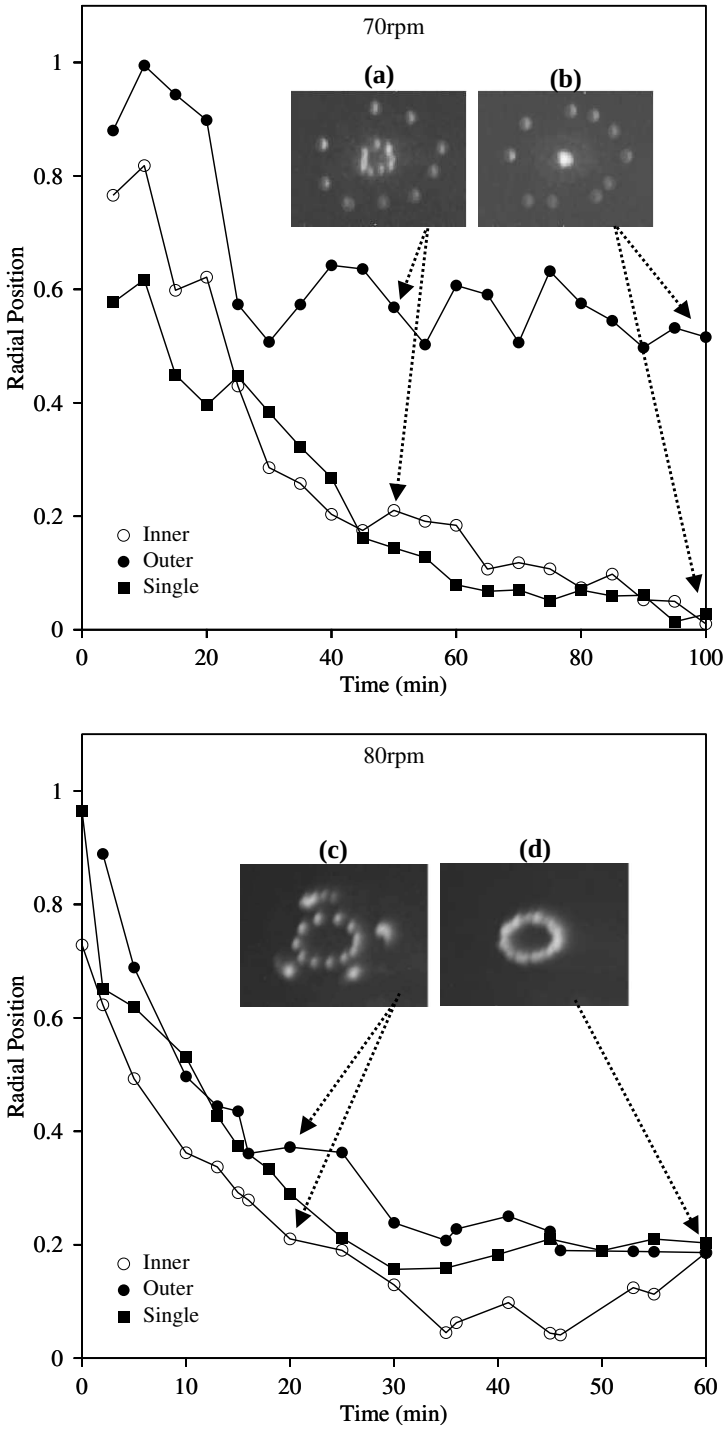

Figure 25: Comparison of radial positions for two heavy particles vs. a single particle at the same rotation rate. Inset snapshots were taken after: 70rpm- (a) 50min and (b) 100min; 80rpm- (c) 20min and (d) 60min.

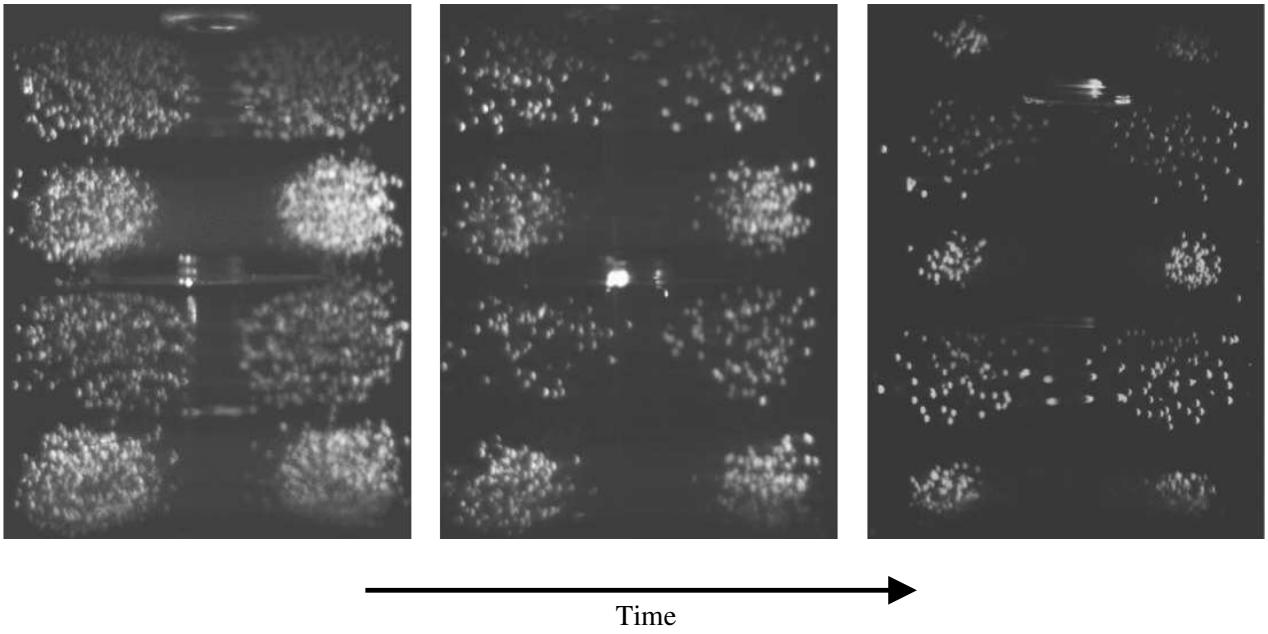

Figure 26: Collection of multiple 2mm particles into the fluid tori of a concentrated suspension.

4.0 CFD ANALYSIS OF ASYMMETRY

In chapter 2, it was discussed that the secondary structures that persist within a chaotic stirred tank flow can possibly be manipulated by varying the properties of the stirred tank itself. In chapter 3, it was shown that changes in impeller spacing had a considerable effect on the particle migration rate. In this chapter, the effect of the impeller tilt-angle relative to the shaft on the stability of the secondary KAM surfaces particularly with respect to non-Brownian particles is evaluated using a Computational Fluid Dynamics based solver called FLUENT©. Building a CFD model also provides a discretized velocity field of the flow dynamics within a particular geometry. The procedure for building the model for the stirred tank flow and the results obtained from this model are discussed in sections 4.1 and 4.2.

4.1 CREATING THE GEOMETRY

The tank model consists of four cylindrical volumes of non-negligible thickness representing the outer tank, shaft and two finite-thickness flat-disk impellers which were created using the preprocessor GAMBIT©. As shown in Figure 27, the four volumes began as line drawings simply spliced together. A surface mesh made of triangular elements was generated on each surface, which was later used to generate a volume mesh made of hexahedral elements for both the 2- and 3-inch diameter impellers.

The original idea of creating four distinct volumes and meshing those individually did not yield perfect connectivity between the surface meshes. Figure 28 shows that the mesh which defines the shaft is unrelated to the tank boundary – an issue for the Fluent solver since it

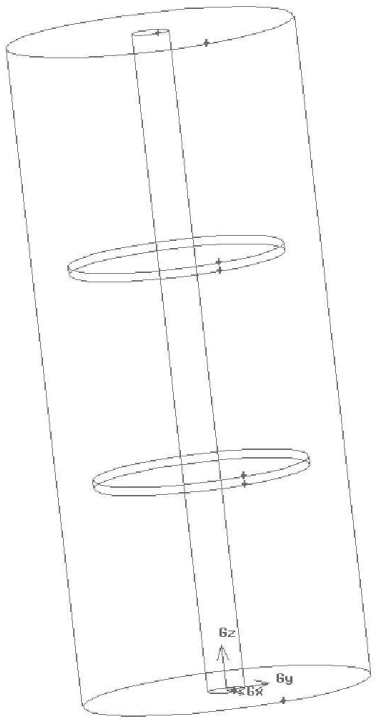

Figure 27: Gambit line drawing showing orientation of the four tank volumes.

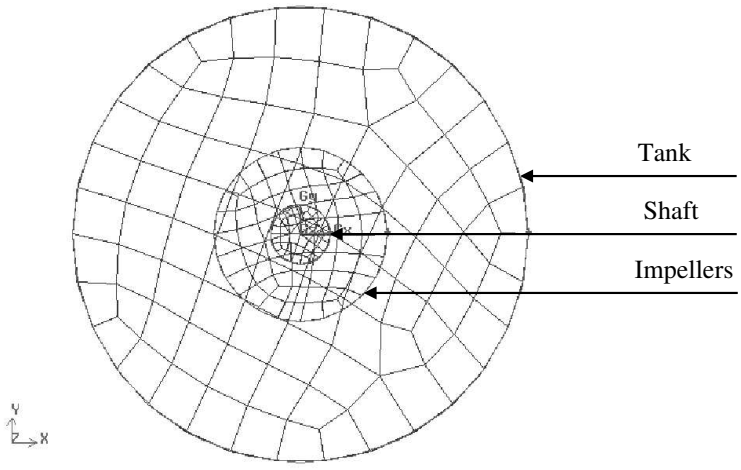

Figure 28: Top view of mixing tank showing mesh disconnection between shaft and tank.

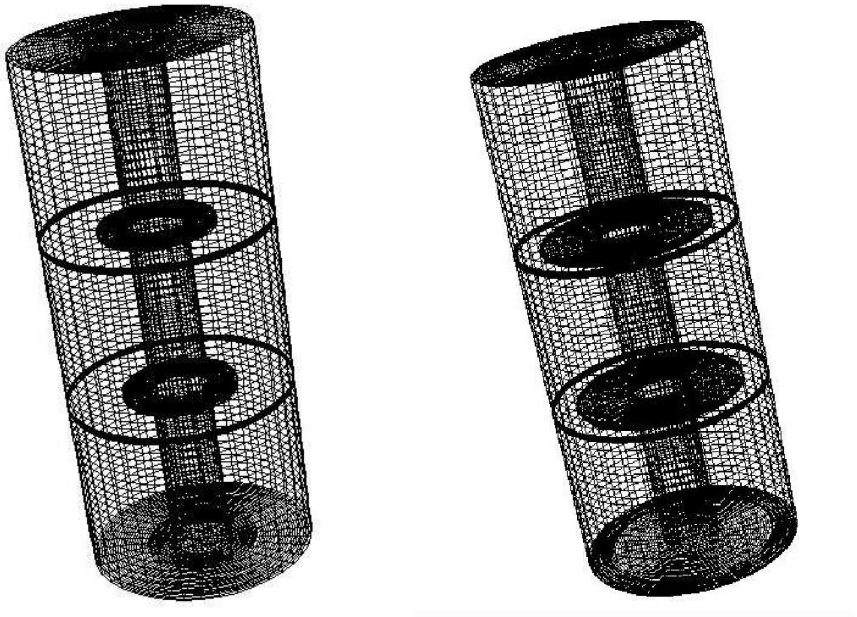

Figure 29: Mesh models of mixing tank with 2-inch (left) and 3-inch (right) impellers

was subsequently unable to create a continuous inner volume mesh between the boundaries. A more rudimentary approach was to create the model from *vertices* (the points that define the volumes), to *edges* (lines which explicitly connect the vertices) and then on to faces and volumes. Creating the mesh this way ensured that the volumes were completely connected, which was necessary to use the Cooper meshing scheme. This meshing technique treats the volume to which it is applied as a logical cylinder consisting of two source faces (which are the ends) and a barrel. This successively created the volume meshes showing in Figure 29. There are two methods to modeling the flow induced by rotating machinery:

1. The **Moving Mesh** method, in which the geometry is completely re-meshed after each iteration to simulate the rotation of the moving parts. This is computationally expensive since it requires more iterations to converge and the solution 're-written' each time.
2. The **Multiple Frames of Reference** approach which involves dividing the tank into two domains, each with its own frame of reference [72]. The impeller/shaft region is assigned to a moving/rotating reference frame which simulates rotation and imparts

motion to the adjacent fluid. The rest of the tank geometry is assigned to a stationary reference frame. A velocity correction is applied at the interface of the two frames of reference, allowing a steady state solution to be obtained.

The Multiple Frames of Reference method was used to solve for the flow field given that it requires less computation. The outer tanks as well as the surfaces defining the shaft and impellers were specified as walls with a no-slip boundary condition. Given these conditions, the simulation usually required approximately 800 iterations (less than 1 hr of real time) run in batch mode to reach steady state. The 2-inch model consisted of 175300 hexahedral cells, 536859 faces and 186334 nodes, and the 3-inch model was made of 175300 hexahedral cells, 538453 faces, and 187694 nodes. The shaft and impellers were defined as non-porous solids made of aluminum; the default interior was assigned the properties of glycerin.

4.2 EFFECT OF IMPELLER TILT

Velocity vectors are commonly used to visualize the direction and magnitude of fluid flow. Figure 30 displays a cross-section of the velocity distribution at 80rpm within the tank. The counter-rotating tori can be inferred, with the velocity magnitude increasing near the moving impellers. The legend also shows that the negative velocity near the tank wall within a particular torus is equal and opposite the positive value near the shaft. This symmetry dies away with increased distance from the impellers, i.e, towards the tank top and bottom.

It had been previously theorized [44] that the chaotic flow in a stirred tank geometry would only be seen when the impeller was tilted relative to the shaft in such as manner as to profoundly perturb the toroidal flow field. In that particular study, nested KAM surfaces were only observed when the impeller tilt-angle was greater than 10°. The setup used in the experiments (as shown in Figures 10 and 11) had a calculated machining error less than 1° for the impeller tilt relative to the shaft.

Thus, the CFD model was used to evaluate whether this seemingly negligible error in the apparatus was enough to substantially change the regularity of the toroidal structures. The formation of the fluid tori can be reproduced using pathlines to trace the trajectory of

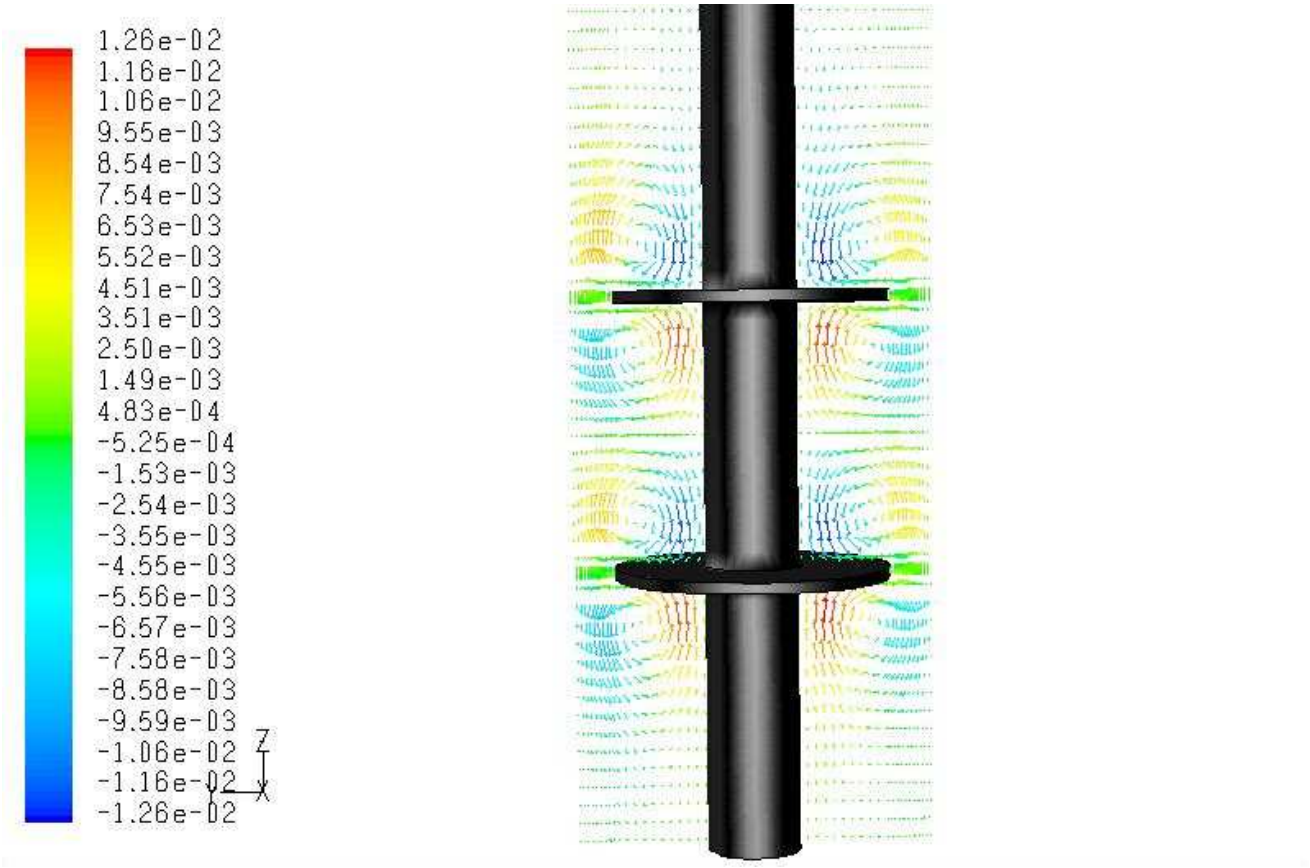

Figure 30: Velocity vectors at 80rpm, clearly showing two distinct counter-rotating tori between the impellers.

fluid particles. 20 pathlines were created along the height of the tank but close enough to the moving parts such that the fluid would be flung into the tori.

Figure 31 illustrates the tori formation when the impeller is perfectly perpendicular to the shaft. For the fluid elements started between the impellers, there is clear formation of the tori as well as the fluid separatrix that would exist between two adjacent structures. Fluid elements that begin outside of the impellers meander into trajectories that rotate about the shaft. Fluid particles that begin between the parallel impellers merge onto distinct paths and move about the shaft at a higher velocity. Figure 32; however, is when the impellers are still parallel to each other but are now tilted with respect to the shaft. Now the tori have 'dilated' and even though they remain distinct, the separatrix is no longer readily seen.

The tilt angle is fixed in space (relative to the shaft), and because the apparatus rotates at a constant rate, also in time. This introduces a constant frequency perturbation of the flow field which can alter the internal structure the tori even as it alters the external shape. It follows that such perturbation would also play a role in the migration behavior of solid particles migrating within such a flow. Since Fluent is unable to create Poincaré sections of the flow, it would require significant post-processing to create a cross section of the dilated tori and evaluate any secondary recirculation surfaces. Thus, these effects are further examined in the following chapter using the BBO model.

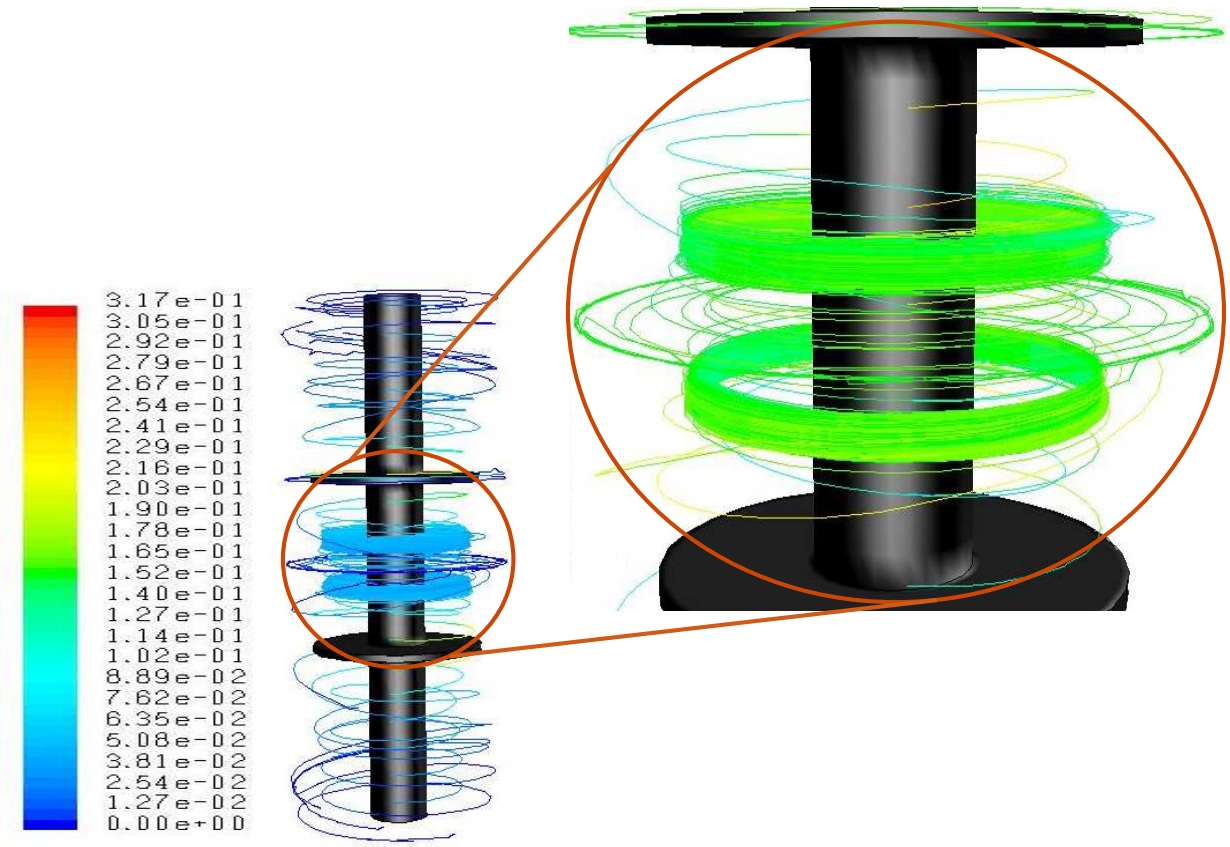

Figure 31: Fluid pathlines within stirred tank geometry for 3-inch impeller and 3-inch spacing: impellers are perfectly perpendicular to shaft, with well defined tori and separatrix.

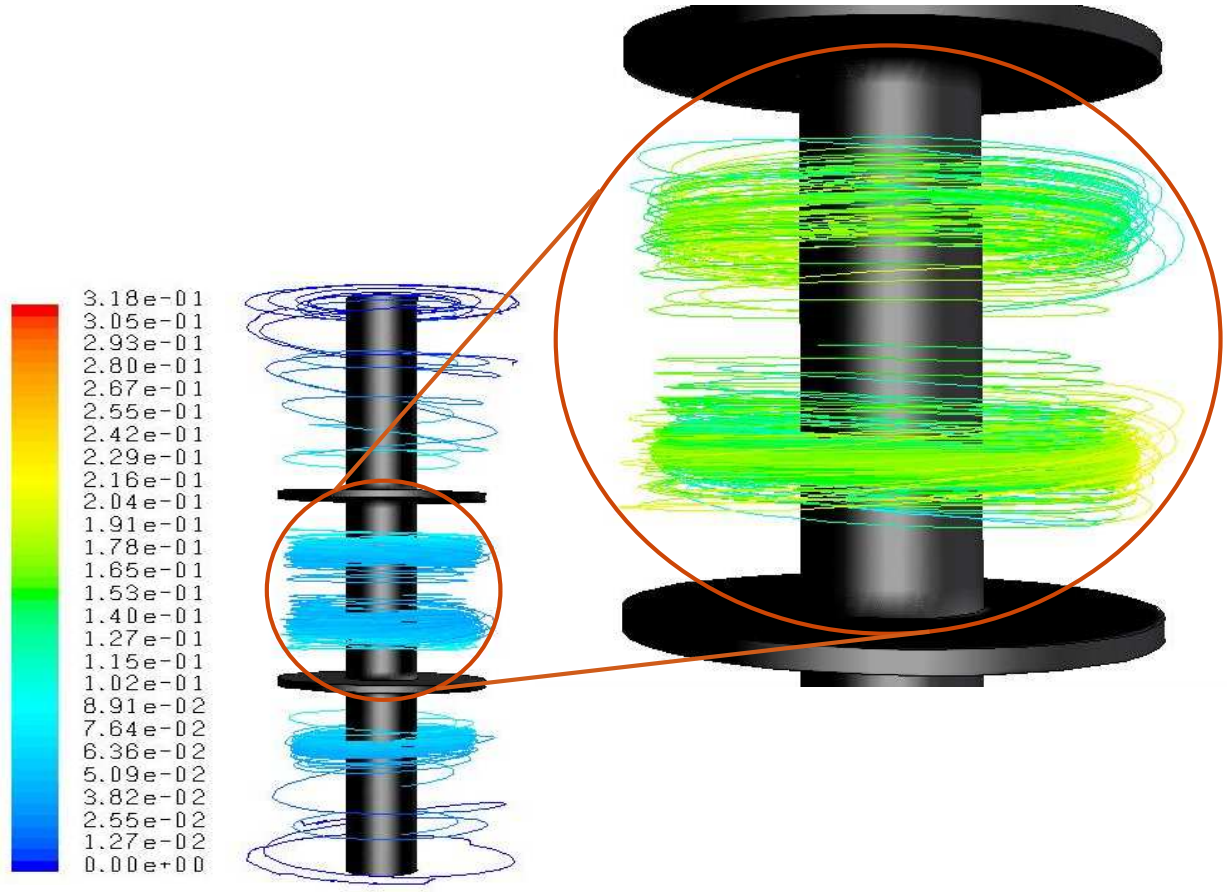

Figure 32: Fluid pathlines within stirred tank geometry for 3-inch impeller and 3-inch spacing: impellers are tilted 1° from shaft, which leads to a dilation of tori.

5.0 MIGRATION IN SIMPLE PERIODIC FLOWS

The objective of this section is to examine the asymptotic equilibria of solid spherical particles within a simple cellular flow. This behavior is simulated using a well-known one-way coupled Lagrangian-Eulerian model for a flow field made periodic in time by the addition of small, non-integrable perturbations. In the following sections, the BBO model is reformulated and used to analyze the migration behavior as a function of particle size, particle density and the rotation rate of the flow.

5.1 EQUATION OF MOTION

Figure 33 is a reproduction of some of the stirred tank experiments for 2mm light and heavy particles at 60 and 80rpm, for 2- and 3-inch impeller spacings. Although the particles end at the same radial position (the center of the tori), the initial slopes of the curves before 30 minutes show that at the larger impeller spacing (3-inch), the particles migrate at a quicker rate than within the smaller (2-inch) spacing. In subsequent plots, the coefficients in the equation of particle motion will be evaluated relative to the ratio U_o/L, which is a measure of shear rate. U_o represents the maximum velocity within the flow as defined by the rotation rate, and L is the cell width, previously defined as the tank wall-to-shaft distance.

Equation 5.1 governs the motion for a small solid sphere with non-vanishing inertia in a multi-directional cellular flow, and is the result of combining Eqns. 2.4 and 2.5.

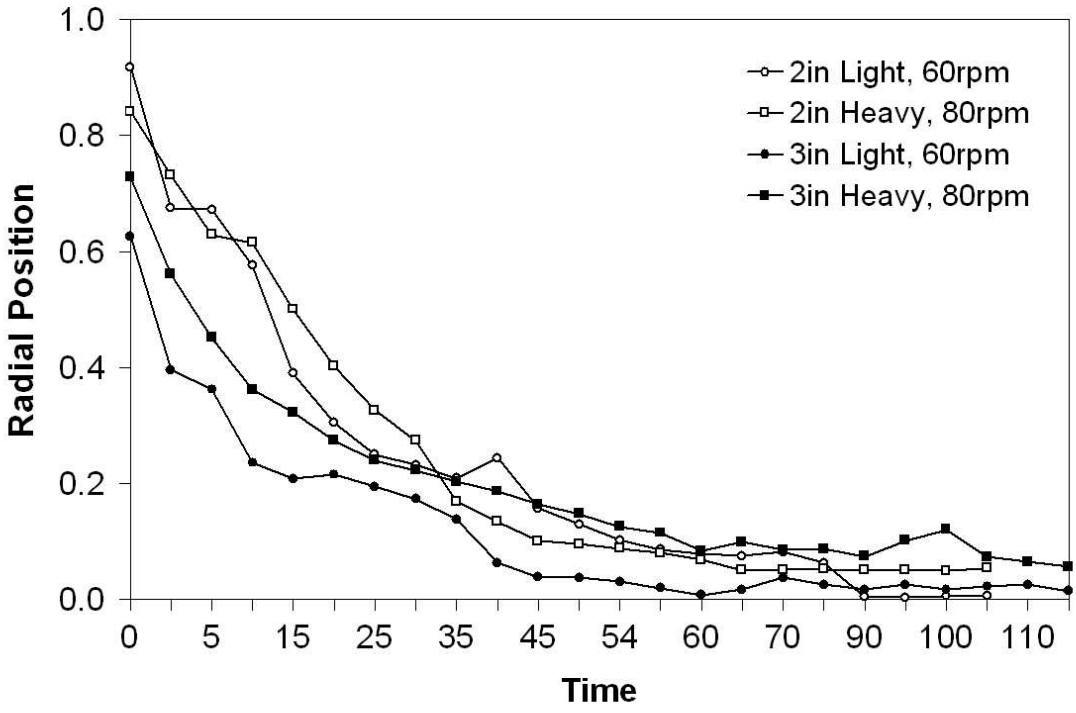

Figure 33: Selected experimental results for 2mm particles with 2- and 3-inch spacing, redrawn from Figures 15 and 16.

$$\frac{d\mathbf{V}}{dt} = A(\mathbf{U}-\mathbf{V}) - W + B(\mathbf{U}+\frac{\mathbf{V}}{2})\cdot\nabla\mathbf{U} + C|\nabla\times\mathbf{U}|^{-\frac{1}{2}}[(-\nabla\times\mathbf{U})\times(\mathbf{U}-\mathbf{V})] \quad (5.1)$$

The coefficients are a result of scaling the length, time, and velocity variables and combining like terms. A can be defined as the ratio of viscous to inertial forces. B is simply a mass ratio and a function of M, an additive mass term. C is the scaled lift coefficient, and W (defined as the settling velocity by Maxey [54]) represents a ratio of the buoyancy to drag forces. These terms are defined as follows:

$$\begin{aligned} A &= \frac{6\pi a\mu L}{U_o M} \\ B &= \frac{m_f}{M} \\ C &= \frac{6.46a^2}{M}(\frac{\mu\rho_f L}{U_o})^{\frac{1}{2}} \\ W &= \frac{(m_p - m_f)G}{6\pi a\mu U_o} \\ M &= m_p + \frac{1}{2}m_f \end{aligned}$$

A quantitative analysis of the various forces that form Equation 5.1 can be obtained by comparing how A, C and W vary with shear rate, as shown in Figures 34, 35 and 36. Values of $\frac{U_o}{L}$ are marked by red arrows for ease of comparison to the experiments . The particle diameter was also kept constant (2mm) for simple comparison and the shear rate was calculated for 0-100 rpm.

The dependence of A on the shear rate is shown in Figure 34, showing a decrease in this coefficient with increasing shear rate, particularly as the rotation rate increases. It can also be seen that A increases with increasing impeller spacing by comparing the magnitude of the (top) 2-inch spacing curves with the (bottom) 3-inch spacing curves of Figure 34, even though the location of the 60rpm and 80rpm experiments change when the impeller spacing

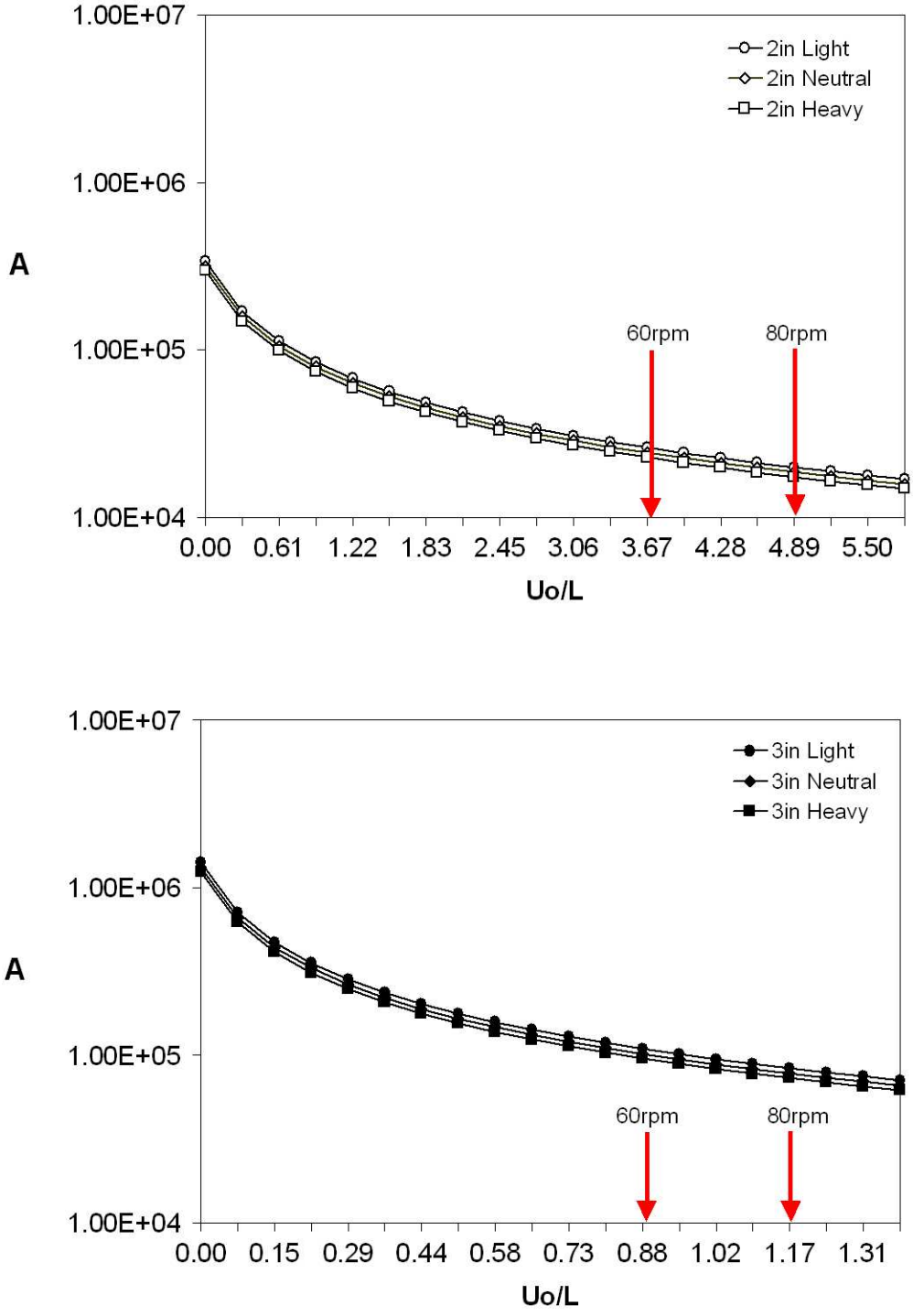

Figure 34: Ratio of viscous to inertial forces (A) showing decreasing magnitude for 2mm particles with increasing shear rate, within a 2-inch (top) and 3-inch (bottom) impeller spacing.

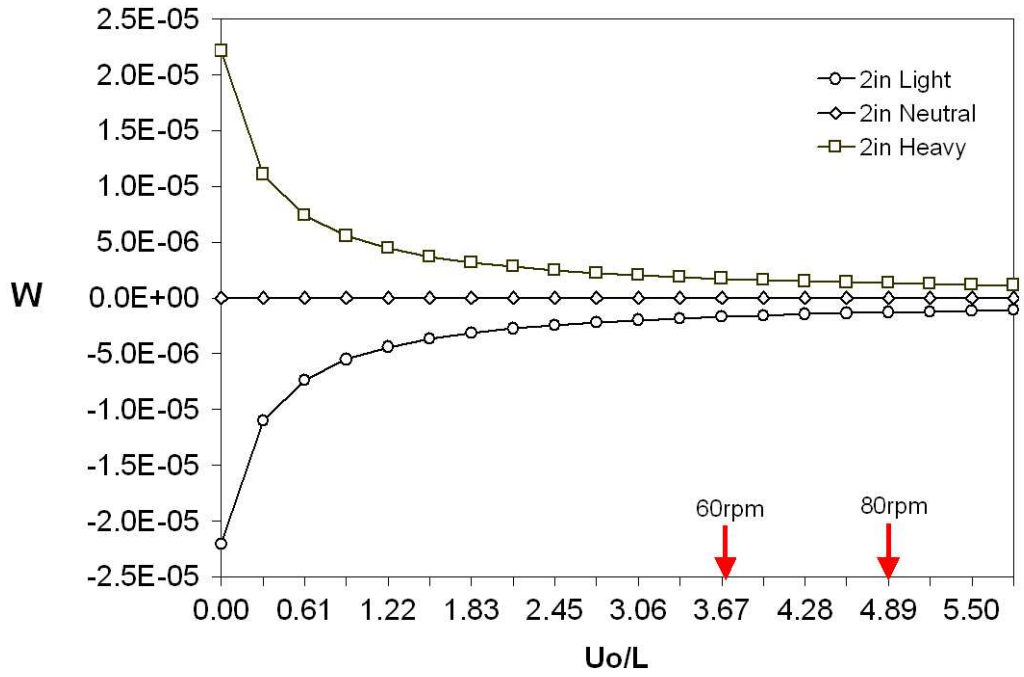

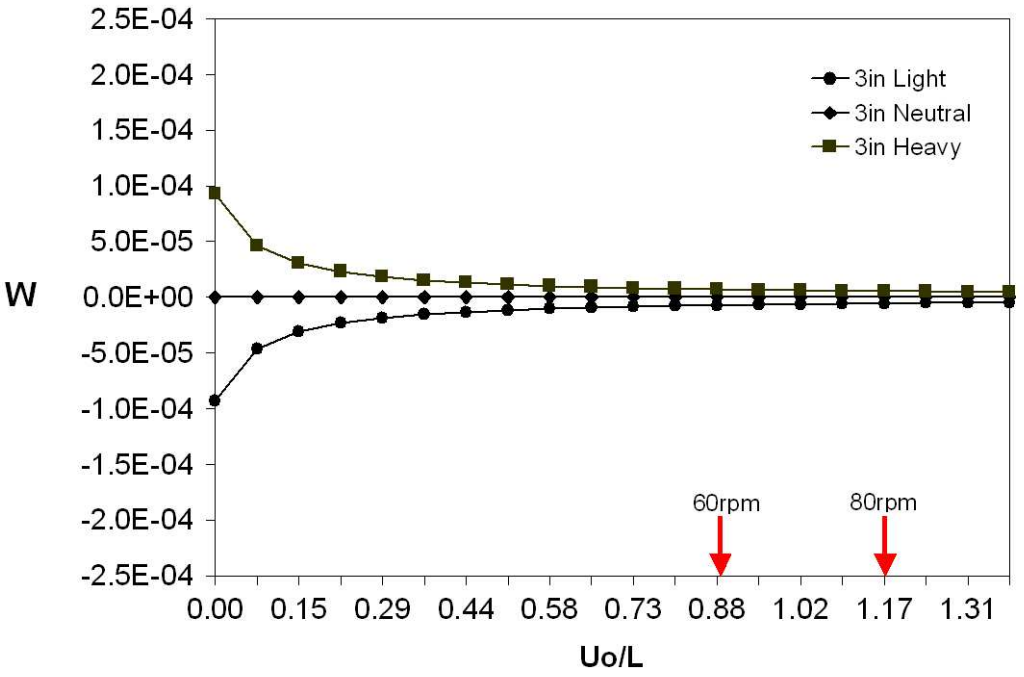

Figure 35: Settling velocity (W) for 2-inch (top) and 3-inch (bottom) spacing. The behavior of light or heavy particles tend to that of neutrally buoyant spheres with increasing shear rate.

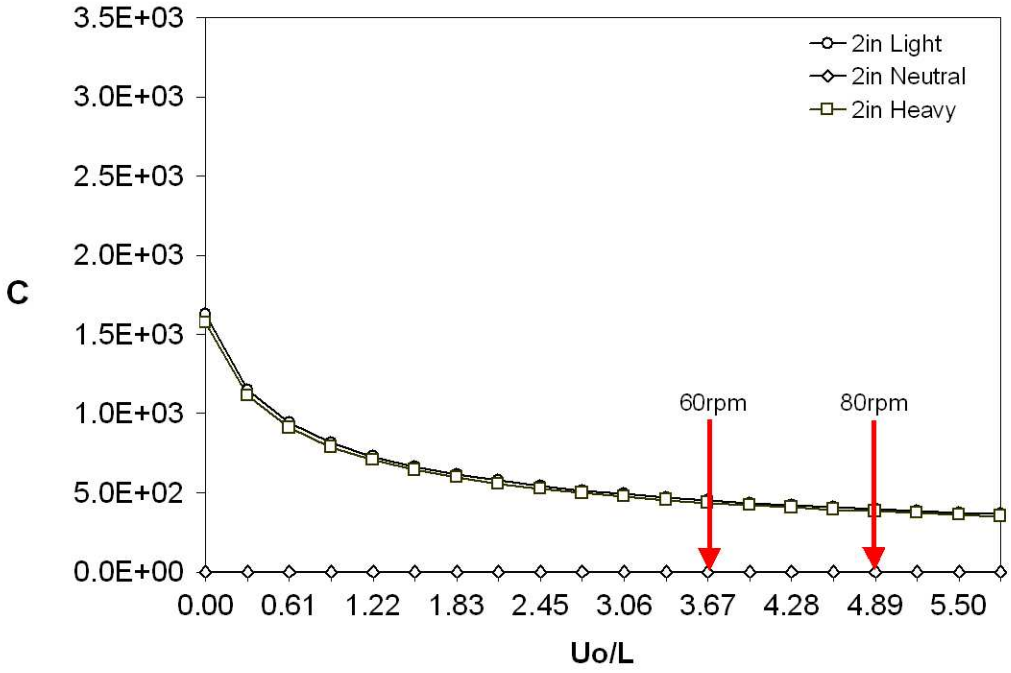

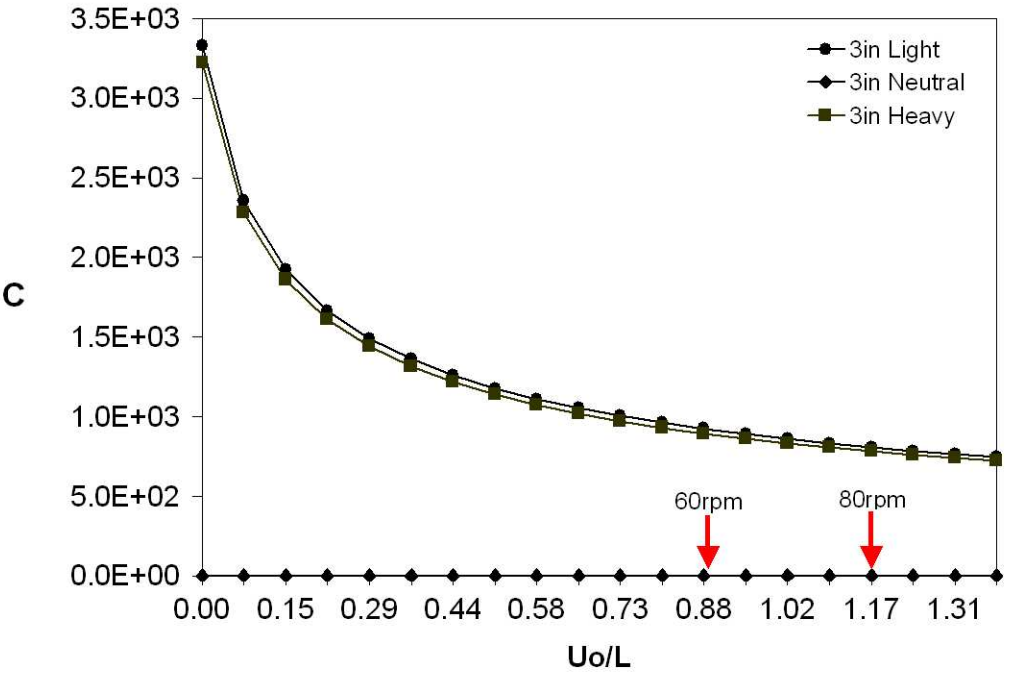

Figure 36: Dependence of lift coefficient (C) on shear rate for 2-inch (top) and 3-inch (bottom) spacing.

is increased. Interestingly, the magnitude of A is almost exactly the same for the light, neutral and heavy particles and for each impeller distance.

Figure 35 suggests that low rotation rates translate to large values of W, thereby allowing gravitational acceleration to compete with other forces. However, at higher rotation rates, the value of W tends towards a plateau as the impact of gravity decreases significantly. For light particles, W asymptotically approaches the constant value of the neutrally buoyant spheres. Heavy particles asymptotically decrease to this value with increasing shear rate.

Whereas hydrodynamic viscous forces cause a centripetal motion about the tank, the lift force enhances lateral motion towards the cell/torus center. Figure 36 shows how the lift coefficient C varies with shear rate. In this case, the lift term exponentially decreases for all non-neutrally buoyant particles with increasing shear rate. The magnitude of C is slightly larger with increased spacing, which supports the faster rate of migration seen in Figure 33 for the 3-inch spacing experiments. As with A and W, this term has the most impact at lower rotation rates.

Figures 34, 35 and 36 also reinforce the experimental findings that the particle behavior deviates from that of a passive tracer as the particle density deviates from that of the fluid. The particle size will play an even larger role as lift is included due to the square of the particle diameter in the numerator in C. Thus, as the particle size increases, there will be a greater departure from passive advection for larger particles since the lift coefficient is dependent on the particle diameter squared. Thus, including the lift force keenly affects the simulations as the particle size changes.

5.2 PERTURBATION FREQUENCY AND AMPLITUDE

Time-dependent perturbations have been used to enhance mixing in stirred vessels. [73]. It has also been observed that asymmetric perturbations are able to move an otherwise stable suspension of particles within a plane Couette flow to a more 'disordered' state system [27]. As was discussed in the background section, the toroidal flow within a stirred tank with parallel disk impellers can also be a chaotic flow.

The parameter α is defined as the particle-to-fluid density ratio (ρ_p/ρ_f). Based on the previous experimental results [74] within a stirred tank, *similar* behavior was observed for both light ($\alpha < 1$) and heavy ($\alpha > 1$) particles, *i.e.*, inward migration patterns. The values of α that are close to 1 reflect the acrylic and cellulose acetate particles used in the experimental work [74]. The simulated cells are 1.0×1.0 in width (x) and height (y) similar to Figure 7. The initial position of the particles vary from x=y=0.1 (near cell boundary) to x=y=0.5 (near cell center).

$$\psi(x,y) = U_o L sin(\frac{x}{L}) sin(\frac{y}{L}) \tag{5.2}$$

In order to capture the higher-order invariant structures that define a chaotic flow, the equation for a regular flow field (reproduced in Eqn. 5.2 with the streamlines shown in Figure 7) is modified with a time-periodic perturbation [68, 75] to achieve the streamfunction in Eqn. 5.3. The symbols ϵ and τ' represent the amplitude and frequency of the periodic oscillation, respectively. As a result of the perturbation, periodic motions are confined to time-invariant fractal structures which are easily observable in physical experiments [44, 74].

$$\psi(x,y) = U_o L sin(\frac{x}{L}) sin(\frac{y}{L} + \epsilon sin(\tau' t)) \tag{5.3}$$

Using this perturbed flow alters the hydrodynamics to that of a chaotic cellular flow consisting of higher-order islands which can serve as attractors to non-Brownian particles. This is akin to Maxey's definition of a capture radius for a regular flow, but extended to periodic flows. In fact, Babiano *et al* [67] conducted a review of KAM theory and stated that a tracer within a chaotic flow will either settle within the KAM tori or selectively visit stable regions characterized by small Lyapunov exponents. Thus, a neutrally buoyant particle even when released at a different velocity than the local fluid will eventually settle onto a trajectory that matches the fluid streamlines, thereby behaving as a tracer particle. Within the BBO model, this is only true if the velocity gradients were not appreciable such

that the two expressions in Eqn. 2.2 would reduce to the material derivative of the fluid velocity ($\frac{DU}{Dt}$) being equal to the the first derivative ($\frac{dU}{dt}$).

It is clear that the choice of the perturbation amplitude and frequency directly influence the size of the toroidal structures within the flow field. Physically, these parameters could be linked to the shaft-impeller parts of a stirred tank flow. In this case, the frequency with which the impeller completes a revolution could be prescribed by τ'. Previous work on such systems had theorized that the chaotic surfaces could only be achieved when the impeller was significantly tilted relative to an axial shaft. Likewise, the tilt-angle could be correlated to the amplitude ϵ of the perturbation caused by the impeller rotation. Thus, increases in either of these parameters results in increased deviation from the structure of the regular cellular flow.

Figure 37 shows that increases in the perturbation amplitude (ϵ) lead to a decreased well-spaced distance between successive streamlines until the emergence and persistence of secondary island structures as the streamlines close about stable locations to form island structures. On the other hand, increases in τ' result in a shift of the cell center and a loss of symmetry within the cellular flow field. These results are for constant fluid velocity.

5.3 REGULAR CELLULAR FLOW

The unaltered Maxey-Riley form of the BBO equation using the streamfunction described in Eqn. 5.2 is examined but within a single cell. Figure 38 depicts the particle positions of light ($\alpha = 0.9$), neutral ($\alpha = 1.0$) and heavy ($\alpha = 1.1$) particles at a constant rotation rate (60rpm) for the same length of simulation time (2hrs), for increasing particle size (a). The middle column of neutral particles of Figure 38 displays the concentric cells of decreasing radius previously described for a non-perturbed cellular flow. These neutrally-buoyant particles show little or no migration, in essence behaving as passive tracers of the cellular flow.

In contrast, the light ($\alpha = 0.9$) particles in the left column of Figure 38 show inward migration. The right column of Figure 38 shows that the *heavy* ($\alpha = 1.1$) particles migrate away from the cell center, as predicted by previous computational studies. These results

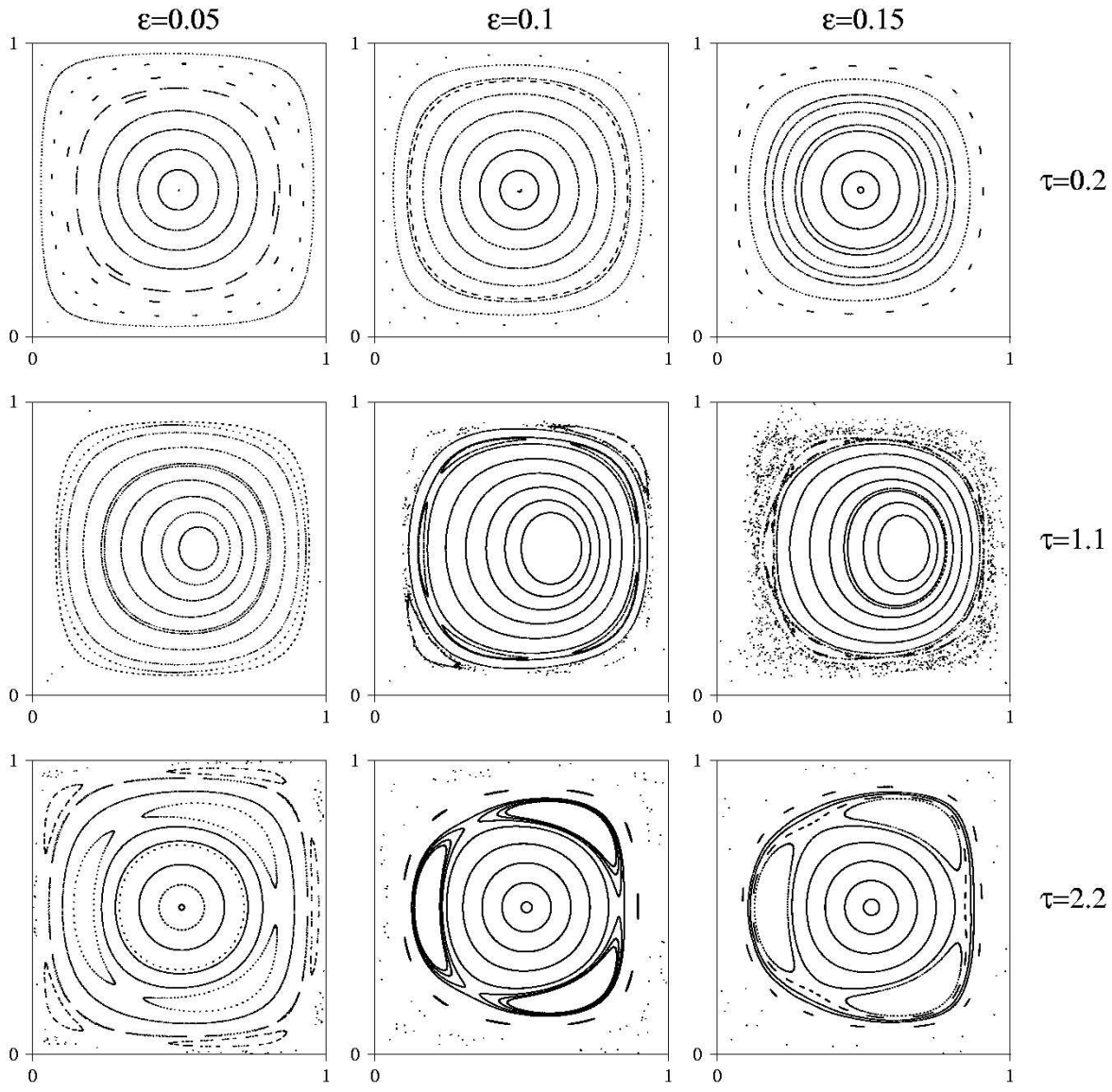

Figure 37: Changes in perturbation amplitude yield return to regular flow for $\epsilon = 0.05$ vs. dilation of secondary structures for $\epsilon = 0.15$. In contrast, increases in perturbation frequency yield a loss of symmetry, particularly for $\tau' = 1.1$

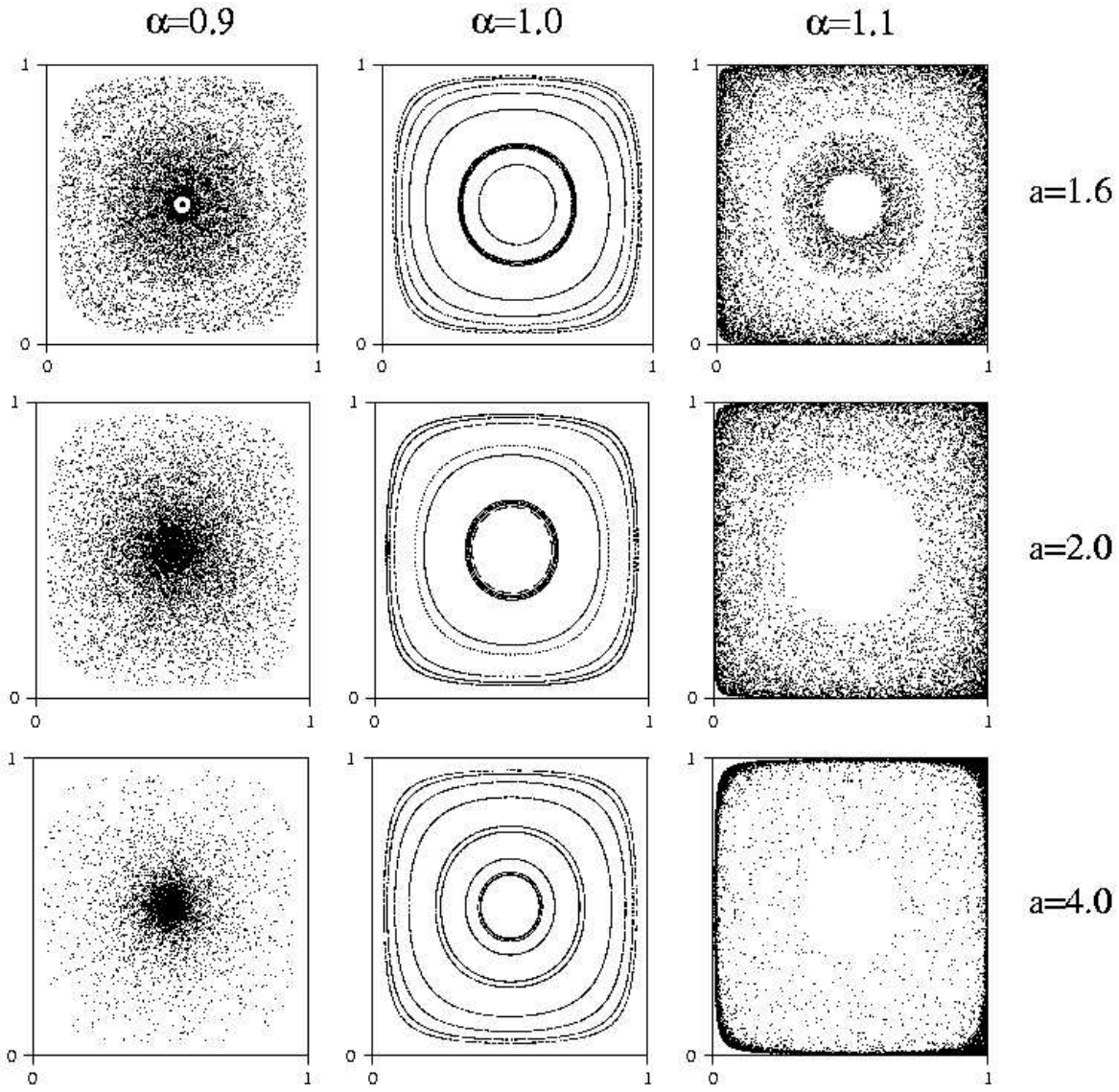

Figure 38: Regular flow at 60rpm. Light particles (left column) show inward migration; neutral particles (middle column) trace concentric trajectories; heavy particles (right column) migrate outward for increasing particle diameter (a).

also reveal the effect of the particle size on the observed particle migration, *i.e.* the larger the particle diameter, the farther the particle migration has seemingly progressed. There are fewer particle positions observed within the cells for the larger diameter particles for the same amount of simulation time, indicating a faster motion with larger particle diameter.

5.4 PERTURBED CELLULAR FLOW

The experimental work involved the chaotic flow between flat disk impellers in a stirred tank geometry. *Inward* migration for all particles was not only observed, but using laser-induced fluorescence, we were also able to capture higher-order toroidal structures which serve as attractors to non-Brownian particles [74]. The BBO model is able to capture rotation rate and particle diameter effects for light particles within the regular cellular flow; however, as written in Eqns 2.1 and 2.4, it incorrectly predicts the outward migration of heavy particles. In addition, a particle advected over the regular flow will not exhibit cluster formations since that particular flow is unable to reproduce the secondary tori. These are created when the cellular flow is perturbed as given by Eqn. 5.3. Figure 39 again compares migration patterns for different density ratios, but within the periodic cellular flow characterized for $\epsilon = 0.1$ and $\tau' = 2.2$. The original cellular flow is recovered by setting $\epsilon = 0$.

The neutral particles in Figure 39 clearly illustrate a slightly distorted cellular flow around the center of the cell, which shall be termed the period 1 island. However, period 3 and period 5 islands are observed further away from the cell center, with very narrow period 4 islands barely observable. It is interesting to note the difference in the size of the islands with particle size: for a=4, the period 5 clusters are much less visible and the period 4 islands seem to have disappeared altogether. Although the period 3 clusters have become more prominent in size, they have not shifted location. The internal structure of the islands is seen to also be nested and concentric – in essence, a replica of the main flow and consistent with the experimental flow visualizations. This is characteristic of invariant tori formations, which replicate *ad infinitum* [65]. More complex behavior can now be observed for the non-neutrally buoyant particles.

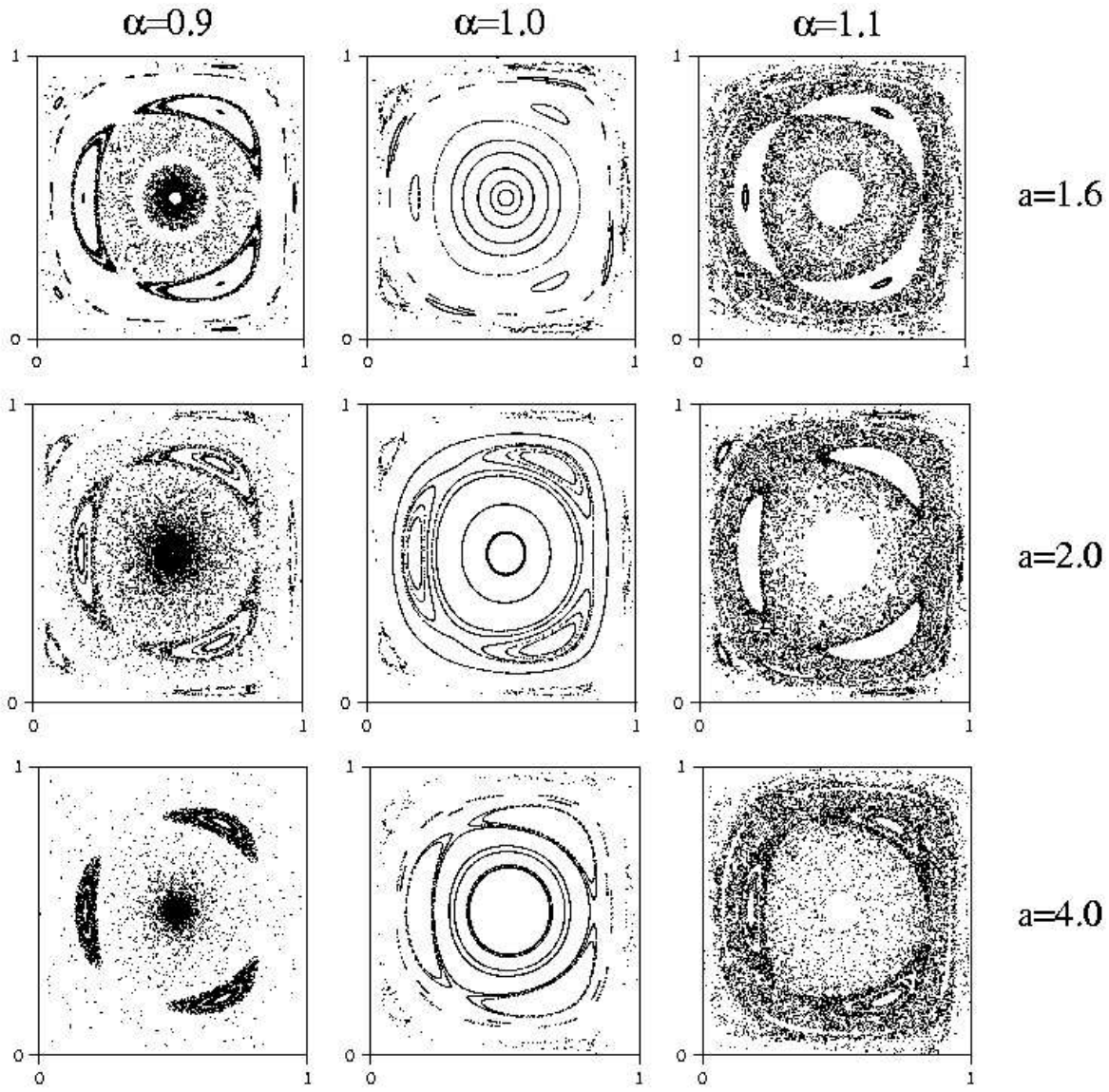

Figure 39: Periodic flow ($\epsilon = 0.1, \tau' = 2.2$) at 60rpm. Light particles (left column) show inward migration towards the cell center and into the period 3 islands; Neutral particles (middle column) maintain a cellular flow in the cell center and trace period 3, 4 and 5 islands further out; Heavy particles (right column) still demonstrate outward migration, but also attraction to period 3 islands particularly as particle size increases.

The light particles in the left column of Figure 39 migrate inwards to the period 1 and 3 locations, with some collection into the core of the period 5 islands. The larger particles in particular no longer fill the outer period 5 orbital but have migrated completely into the period 3 islands or into the cell center (period 1). The heavy particles in the right column of Figure 39 no longer collect at the periodic boundaries of the cell, but rather stay in the core of the period 3 islands or else outside of any island structures. In fact, the period 4 and 5 islands are again noticeable because the particle positions outline the location of these structures. With increased particle size, the inward migration of these particles is now more noticeable since the particle positions in effect outline this structure's location. Thus, the use of a forcing function to perturb the streamfunction yields a better representation of the flow and particle behavior seen in the experiments.

Although the overall direction of migration is not affected by initial position in the experiments, the initial location of a particle likely dictates the asymptotic position, particularly for non-neutrally buoyant spheres. Figure 40 illustrates this dependence for particles initially placed within period 3 and period 5 structures. The large black dot denotes the initial position of the particles, which is stated in parentheses by each row.

Particles of the same density as the fluid will trace out the fluid island structures, providing information as to the possible equilibrium positions. The plotted positions in the top plot of Figure 40 are for particles which began at (x,y)=(0.50, 0.18), which is near the edge of the period 3 islands. These particles outline not just the period 3 islands but the period 5 islands as well. In fact, the period 5 islands seem to be made up of smaller period 5 structures themselves, both for the neutrally buoyant ($\alpha = 1$) and heavy ($\alpha > 1$) cases; a phenomenon which is reminiscent of the repeated islands in the experimental flow (recall Figure 23). The light particles only trace the period 3 islands and only faintly outline the period 5 structures.

This changes slightly for particles begun in the top right island. Instead, the neutral particle traces the inner streamline of the period 3 islands; the light particles showcase the tertiary period 5 islands while the heavy particles have predominantly migrated to the center of the period 5 structures. Finally, the bottom row of Figure 40 shows particles which stayed at the center of the period 5 fluid islands.

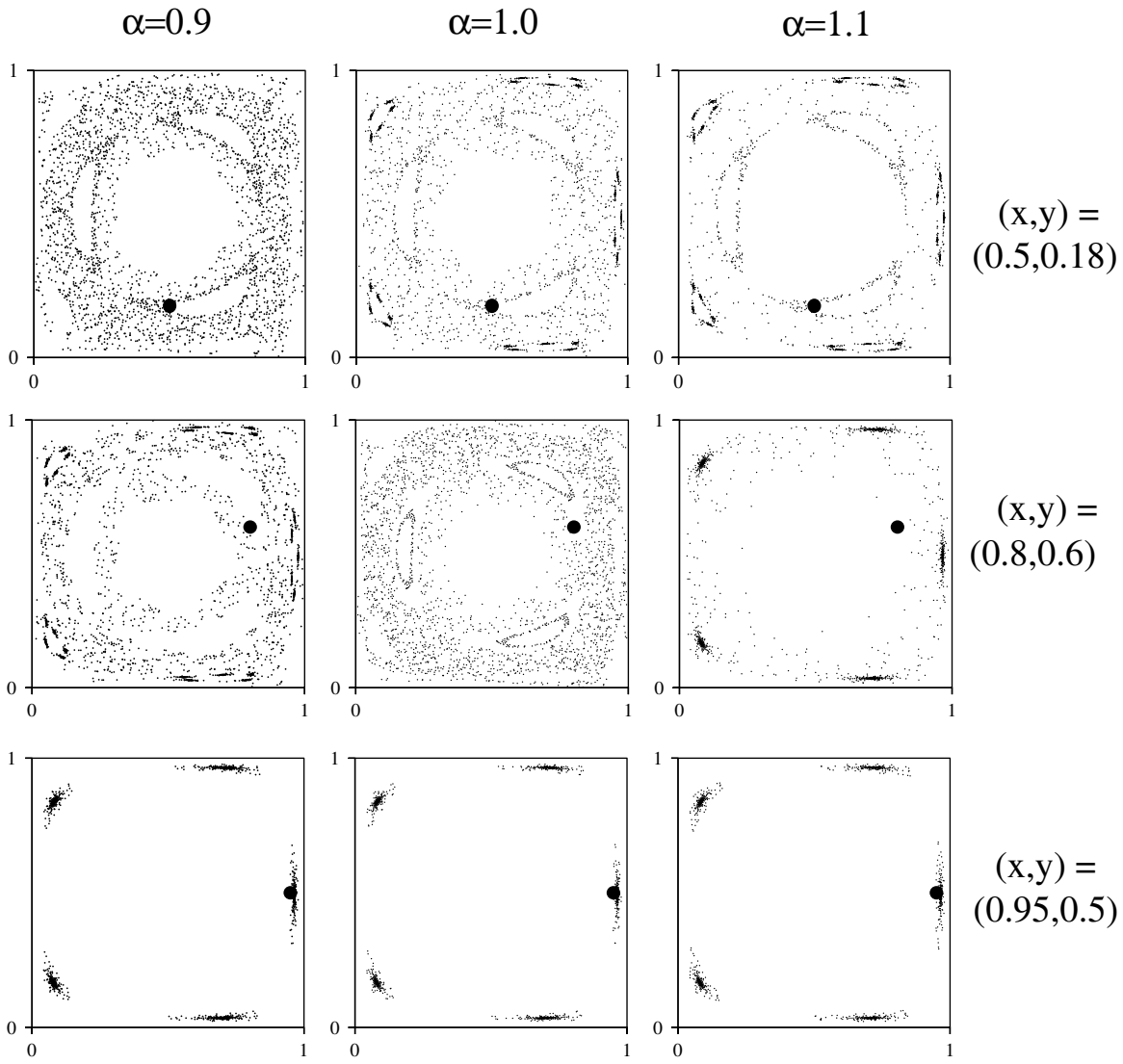

Figure 40: Initial placement effects for particles originally within bottom period 3 island (Top), within top right period 3 island (Middle) and furthest right period 5 island (Bottom). Large black bullet corresponds to (x,y) values shown, and marks exact initial location.

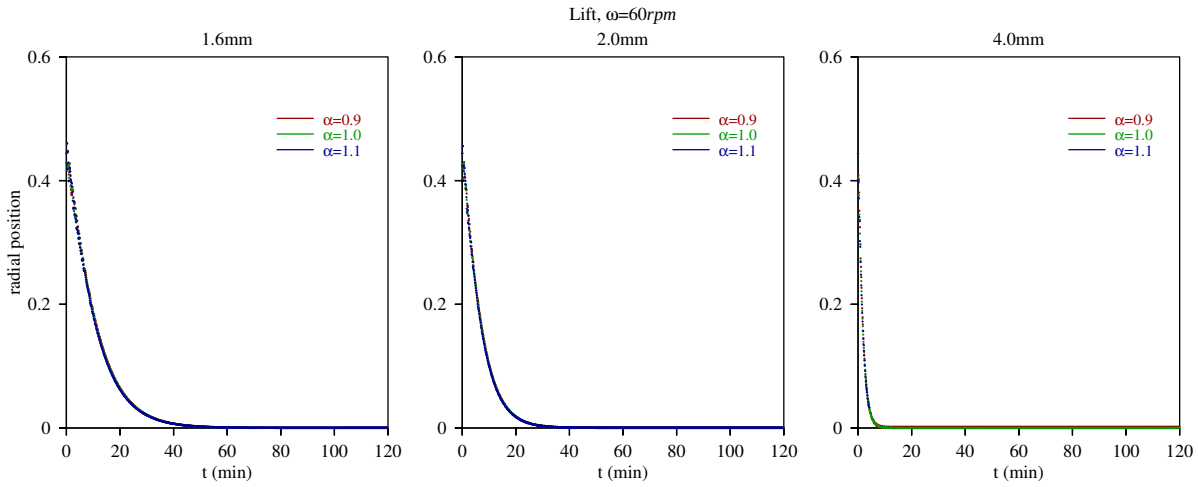

Figure 41: Radial positions as function of particle diameter and density, with lift

Animations of the particle position shows that for a particle begun within the period three islands, the particle visits each of the 3 islands in succession mimicking a 3D KAM tube. However, although the third dimension in the real life 3D scenario is spatial (*i.e.* including the z-direction); in this model, the third dimension is temporal and a result of the forcing function with respect to time.

5.5 LIFT EFFECTS

Finally, the lift force as previously given by Eqn. 5.1 is included in the model. Within a regular cellular flow (ϵ=0), there is an inward migration for all particles, with the rate of migration increasing with particle size as shown in Figure 41. It is interesting to note the behavior of the $\alpha = 1$ particle: it no longer shows slightly deviation from the flow, but is heavily influenced by the Saffman lift.

The reader should recall the force diagram within a 2D rotating flow (Figure 6) as derived by Ramirez *et al.* [1], where the two radial forces are the pressure (F_P) and lift (F_L). In the limits of *Re* prescribed for the lift force (given by Eqn. 2.5), the magnitude of the lift force

is much larger than the pressure term owing to the larg(er) particles being studied. Thus, inclusion of this term would overwhelm drag and buoyancy terms, forcing the inward motion of all particles.

Figure 42 illustrates the computed particle positions for the 1.6mm and 4mm particles at 60rpm for 2 hours of simulated time within a perturbed cellular flow. Again, there is no longer a pronounced difference between the $\alpha = 0.9$ and $\alpha = 1.1$ particles at steady state both for the regular flow field (top row) or for the perturbed flow (middle and bottom rows). There is still increased extent of migration as the particle size increases particularly when comparing a=1.6 (middle row) with a=4.0 (bottom row) particles within the perturbed flow. In fact, the small particles show a strong attraction to both the period 1 and period 3 islands, whereas the larger particles migrate further inwards and bypass the period 3 structure altogether. This mirrors our experimental findings [74] and reinforces that slightly non-neutrally buoyant particles can display inward migration within cellular flow structures regardless of whether $\alpha < 1$ or $\alpha > 1$.

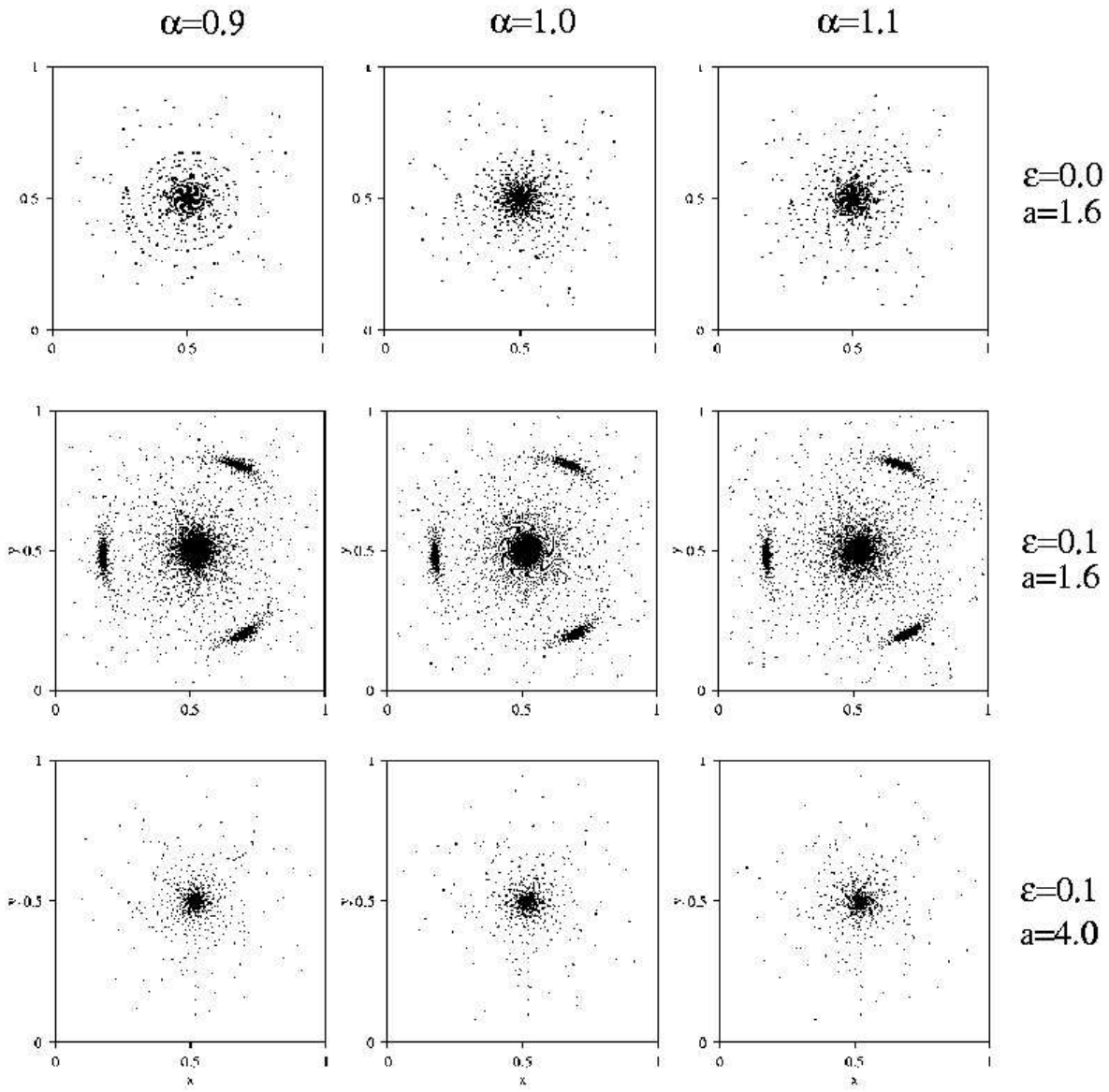

Figure 42: Lift effects within regular and periodic flows. All particles show inward migration with no appreciable difference for the various density ratios.

6.0 DISSIPATIVE PARTICLE DYNAMICS

Although the BBO model can yield qualitative insight into the experiments, more rigorous solid-fluid computational tools can better account for the interactions between both phases (two-way coupling). In this section, we discuss using a more strongly two-way coupled simulation technique called Dissipative Particle Dynamics to simulate a heavy particle migrating within a pipe flow.

6.1 FORCE MODELS

DPD is a coarse-grained simulation technique based on Molecular Dynamics, in which the fluid is actually made up of fluid particles and solid particles can be simulated as 'frozen' aggregates or clusters of the fluid. This method has been used to simulate complex flows such as colloids and emulsions [76]. This study specifically noted that using 'frozen' DPD particles to simulate a discrete elements can incur additional computational cost due to an increased potential while trying to conserve interactions between particles.

Other studies [77, 78] have investigated the change in length of macromolecules in linear shear flows particularly during extrusion processes. The polymer melt was treated as a continuous solid phase within another continuous fluid phase, with the DPD method able to capture the changes in polymer properties. There has also been some application of DPD models to biological systems such as the the extension of DNA molecules within microfluidic channels [79], with relative success.

DPD uses three force models to capture the physical phenomena of interest. The **conservative** force (F^C) models a soft repulsion between particles to enforce elastic collisions, and is shown in Eqn 6.2.

$$\begin{aligned} F^C &= a_{ij}(1 - r_{ij})\hat{\mathbf{r}}_{ij}, r_{ij} < r_c \\ &= 0, r_{ij} \end{aligned} \tag{6.1}$$

The **dissipative** (F^D) force shown in Eqn 6.2 reduces the relative velocity between two particles, simulating viscous fluid effects.

$$F^D = -\gamma w^D(r_{ij})(\hat{\mathbf{r}}_{ij} \cdot \mathbf{v}_{ij})\hat{\mathbf{r}}_{ij} \tag{6.2}$$

Finally, the **random** force (F^R) is the result of all thermal molecular motion within particles i and j. The random force coupled with the dissipative force act as a thermostat by adding heat to the system. This force is given by Eqn 6.3.

$$F^R = \sigma w^R(r_{ij})\theta_{ij}\hat{\mathbf{r}}_{ij} \tag{6.3}$$

In equations 6.2, 6.2 and 6.3, $\mathbf{r}$ represents the position vector; a_{ij} is the maximum repulsion between particles within a pre-defined cutoff radius, r_c, and θ_{ij} is a random number function. Using these forces, the transport equations for a simple DPD particle i are shown in Equation 6.5.

$$\frac{d\mathbf{r}_i}{dt} = \mathbf{v}_i(\frac{y}{L}) \tag{6.4}$$

$$\frac{d\mathbf{v}_i}{dt} = \sum_{j \neq i}(F^C_{ij} + F^D_{ij} + F^R_{ij}) \tag{6.5}$$

In Eqn 6.5, $\mathbf{v}$ represents the individual fluid particle velocity vector. The coefficients γ and σ characterize the magnitude of the dissipative and random forces, which vanish for $r > r_c$. Both w^D and w^R are weighting functions which satisfy the following condition:

$$w^D(r) = [w^R(r)]^2, \quad \gamma = \frac{\sigma^2}{2k_BT} \tag{6.6}$$

6.2 BOUNDARY CONDITIONS

Equation 6.6 ensures a balance of kinetic energy within the DPD model based on the Fluctuation-Dissipation Theorem [80], where k_B is the Boltzmann constant and T is the temperature of the system. This theorem states that a perturbation within a system at the molecular level dissipates as the system returns to equilibrium. [79, 81] In essence, F^D and F^R serve as a thermostat in order to maintain the temperature, ensuring the system is not artificially heated.

The manner in which the walls are prescribed in DPD is an unresolved matter in the literature. Wall particles are 'frozen' (*i.e.* of the lowest thermal energy within the system), but the soft repulsion between particles does not prevent actual fluid elements from 'penetrating' the wall. For particles which interacted with the wall, the tangential component of velocity was randomized (using a random number generator) to generate a new direction whereas the normal component was made equal in magnitude and opposite in direction.

In addition, there is the problem of the wall particles decreasing the overall fluid temperature. Various researchers have sought to combat this by analytically solving for effective wall forces, [82] increasing the density of particles at the wall, [77, 78] or by introducing a random velocity distribution (with fixed mean) for the wall particle [79].

In implementing a DPD model, we have opted to follow the Fan *et al.* [79] approach for solid boundary conditions. That is, we keep the wall particles frozen and induce a random velocity distribution (with zero average slip velocity) within a thin particle layer near the wall. Also, particles that collide with the walls have the same normal velocity, but in the opposite direction.

6.3 LATERAL PIPE MIGRATION

A 3D linear shear flow was simulated to test and establish DPD capabilities using 12000 particles. The graph in Figure 43 illustrates the initial and final velocity of each particle, clearly showing the standard parabolic profile for flow within a pipe.

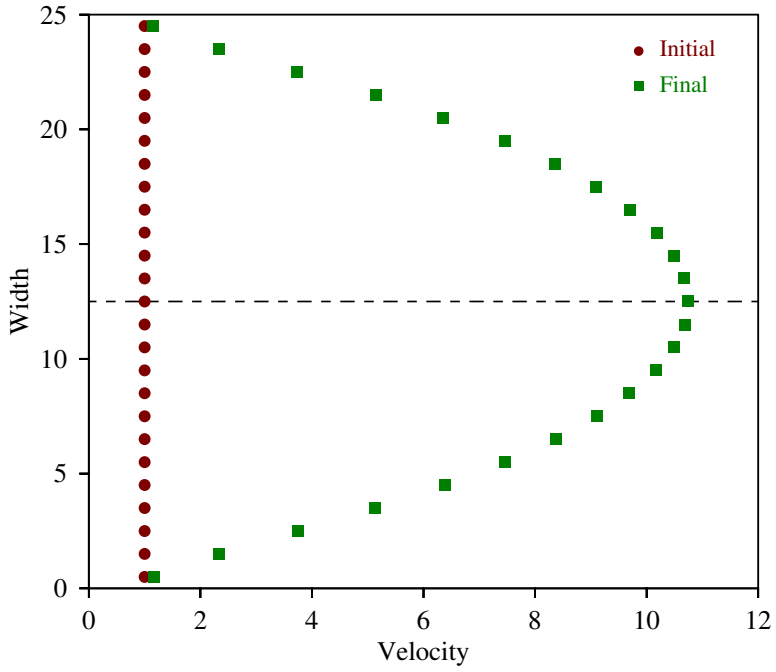

Figure 43: DPD simulation of 12000 fluid particles within a pressure-drive pipe flow: velocity profile.

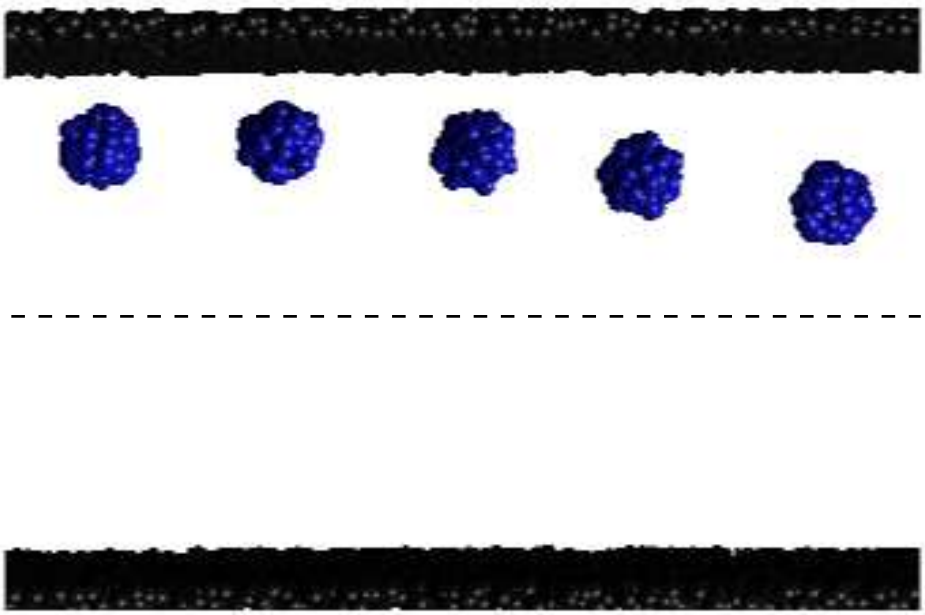

Figure 44: DPD simulation of 12000 fluid particles within a pressure-drive pipe flow: migration of 200-particle cluster

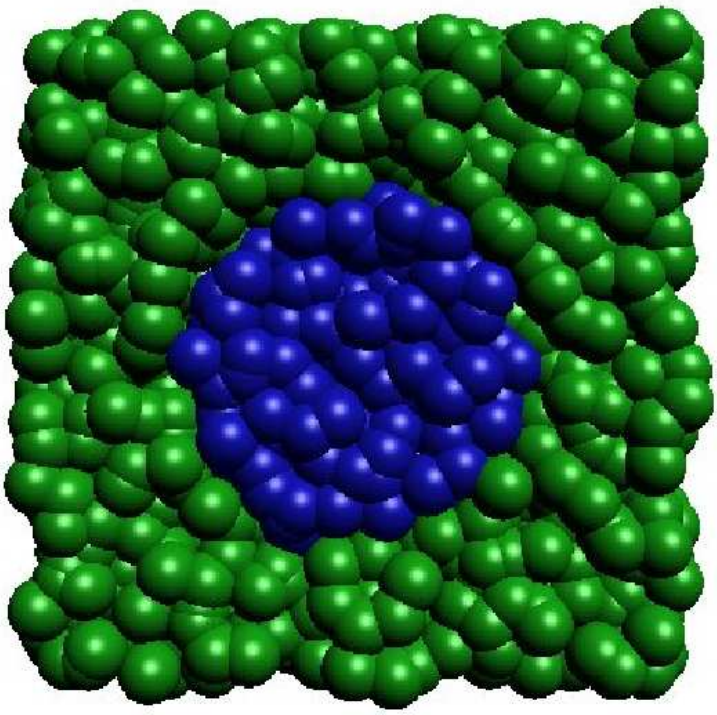

Figure 45: Close-up of fluid elements with particle defined by ‘frozen’ cluster.

Figure 44 illustrates the results we have obtained for a heavy particle cluster migrating within the pipe flow. In the domain of 12000 particles, we set 200 to be a 'cluster' of solid particles, *i.e.* they did not move relative to each other. The motion of the cluster is governed by the averaged forces and torque of each individual particle. The particle seems to be moving toward the center line of the pipe (a region of higher shear) which is in line with the literature for a heavy particle. Figure 45 is a closeup of the particle cluster position within the larger fluid particle domain.

6.4 CONCLUSIONS

The results from the DPD pipe model are promising. The fact does remain that Dissipative Particle Dynamics as a viable modeling tool for fluid-solid multiphase systems is not clearly established, as illustrated by the boundary condition issue. Thus, it could prove more beneficial to experiment with other two-way coupled discrete element methods, such as the Lattice Boltzmann method (LBM).

As detailed in a review by Chen and Doolen [83], LBM is an easily-parallelized algorithm, able to model the intricacies of multiphase flows while incorporating the physical interactions that occur in such systems. Although based on the Lattice Gas (LG) Automata kinetic model, a simplified kinetic equation is used in LB. Time and space are still defined on a discrete, symmetric lattice, with particles initially residing at each node of the lattice. At each time step, a particle can either *stream* to the nearest node in the direction of it's resultant velocity, or *collide* with another particle. In the latter case, both particles have a resultant velocity based on scattering rules.

7.0 SUMMARY AND OUTLOOK

The migration phenomena within multiphase systems was experimentally and computationally examined in order to understand the parameters which govern the behavior of these structured suspensions. The results demonstrate that the migration of particles in a multi-directional, viscous flow with finite fluid inertia yields a rich variety of behavior.

7.1 STIRRED TANK FLOW

This work has demonstrated that particles both heavier and lighter than the continuous phase can migrate across streamlines to position themselves in repeatable equilibrium locations in the flow between parallel disks within a stirred tank. At certain rotation rates, the particles remain stalled in clusters within the flow which seem to closely coincide with regular islands within the chaotic fluid flow. An exponential migration rate was quantitatively observed whenever the particle crosses the 2D laser sheet in discrete locations, but no migration when the particle is stalled in the various clusters. Table 1 concisely displays the observed cluster patterns, as well as the approximate asymptotic value of the radial position. This suggests that some control of the asymptotic particle position is possible through manipulation of the fluid island positions and size. It was also noted that in multi-particle experiments, inter-particle interactions seem to promote/allow migration for one particle at the expense of the other, even at vanishingly small concentrations.

The dye advection experiments suggest that the stalling behavior is characterized by the particle interaction with the higher-order KAM surfaces/islands. The higher-order tori are farther away from the center of the torus; however, the stability of a particle within these

KAM tubes is highly dependent on the local shear environment, as dictated by the rotation rate and impeller spacing. The particles tend to reside in lower-order islands as the rotation rate increases or conversely, as the impeller spacing decreases. The literature suggests that the sizes of the fluid islands increases as the particle approaches the torus center, [44, 45]. Such studies align with the observation that larger particles are forced to migrate further inward to find islands large enough to be trapped within. However, if the sizes of the fluid islands are preserved by an increased impeller spacing, the particle can still reside in a higher-period island at a relatively higher rotation rate. This would also help to explain the same periodicity clusters at different rotation rates and different impeller spacings (see Table 1).

7.2 NUMERICAL MODELS

FLUENT© was used in Chapter 4 to visualize in 3D the toroidal flow within a stirred tank as a function of impeller tilt-angle. It was seen that even a slight tilt of the impellers relative to the shaft was sufficient to change the internal structures of the tori, and thus, the migration behavior of particles within these structures. Chapter 5 presented a 2D numerical analysis of the migration of spherical particles in a cellular viscous flow using the BBO model. This motion is a function of the localized fluid profile around the single particle as it moves through the fluid. When the particle rotation about its own axis is accounted for (by including the lift term), it is seen that particles of different density than the fluid can migrate across the streamlines towards the center of the flow. The rate of this motion is more pronounced as the size of the non-Brownian particle deviates from that of the fluid.

Chapter 5 also showed that fluid islands can be generated by slightly perturbing the flow field. These structures are attractors for both the heavy ($\alpha > 1$) and light ($\alpha < 1$) particles, with increased migration rate as the particle size increases, although this was also seen with the inclusion of lift for the regular flow. In conclusion, the use of periodic perturbations yielded a means of qualitatively comparing the entrapment of non-Brownian particles within a rotating flow to the experimental results.

7.3 OUTLOOK

This dissertation has outlined various approaches to the non-Brownian migration phenomena. As such, there are multiple avenues that the future of this project could pursue.

7.3.1 Mixing Tank

The differences in initial position does not seem to affect the rate of migration *once* the particle is caught within the primary toroidal flow. However, it would be more convincing to initiate particle motion at certain specific locations so as to make sure the asymptotic particle position (particularly in the cluster formations) does not depend on initial placement. This would demonstrate experiment repeatability, but also the differences (if any) from different initial conditions could be examined.

The interest in particle migration is not solely confined to rigid particles, but can also be expanded to droplets (e.g. silicon oils which are immiscible with glycerin) or bubbles of different gases. Of particular interest is the shape of the particles in different shear regions of the flow, and if there is any internal circulating motion particularly for droplets consisting of an immiscible fluid of different viscosity than the main flow.

It is also not clear if there is a clear bifurcation in the observed particle island formations. If so, the transition between the islands should be quite clear. Experiments performed at intermediate rotation rates should clearly show the nature of any transition. It would also be advantageous to investigate the impact of disk diameter on the size of the fluid tori, especially as the impeller diameter was kept constant in this study at 3 inches. This could also be correlated to the effect of impeller spacing, since both the disk diameter and spacing affect the maximum length of the tori in which the particles migrate.

Finally, there is an interest in further understanding the multi-particle experiments (Section 3.5), since is obvious that multiple particles affect each other within the tank flow. However this requires the development of a visual method to track the paths/trajectories of the particles, possibly by introducing a single fluorescent particle into a system of same-density, non-fluorescent particles.

Table 2: Asymptotic particle positions for non-neutrally buoyant particles within rotating clinostat or HARV, according to Ramirez *et al.* [1].

Quadrant	**Equilibrium for:**
I	heavy particle with lift
II	light particle without lift
III	light particle with lift
IV	heavy particle without lift

7.3.2 HARV

Ramirez's analysis [1] of the flow within a HARV predicted 4 quadrants based on the flow properties of the particle. The force distribution reproduced in Figure 46 for a clockwise rotation shows that the pressure term (F_P) always points inward to the center of the HARV. The drag term (F_D) mimics the direction of rotation of the apparatus, the buoyancy term (F_B) points up or down depending on whether a particle light or heavy. The lift term (F_L) points away from the cell center, in the opposite direction of the pressure term. This suggests that for heavy particles in a real life experiment (where lift cannot be arbitrarily turned on or off), the equilibrium position would be located somewhere within quadrants I and IV.

Preliminary experiments were conducted in a simplified HARV (recall Figure 5). The 'growth cell' in the experiments was made from cast acrylic and mounted onto a horizontal motor. This apparatus rotated in a clockwise direction at low rpm, thus the force balance in each quadrant is more accurately represented by Figure 46, with the expected particle location summarized in Table 2.

Figure 47 shows preliminary experimental results for two types of heavy particles; the top is a 4mm glass sphere and the bottom of Figure 47 is a 3mm steel particle. These were

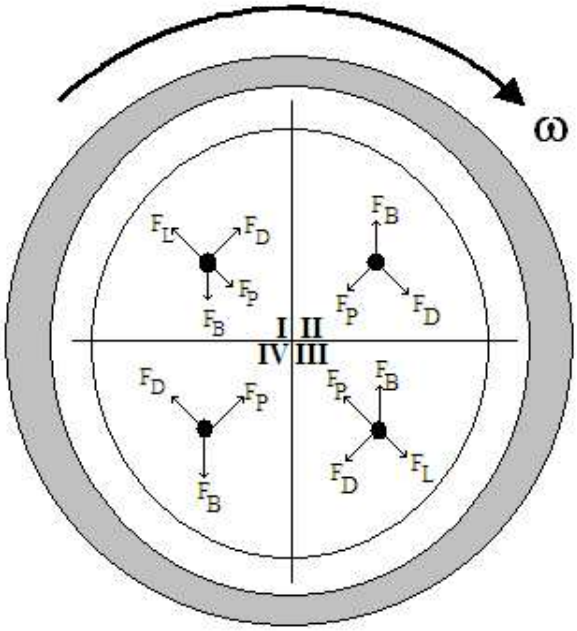

Figure 46: Front view of clinostat illustrating the force distribution in different quadrants for clockwise rotation at constant ω.

chosen predominantly because they were readily available and easy to visualize without the complex laser fluorescence setup. Both also show trajectories that seem to converge about the horizontal plane between quadrants I and IV, in line with the theory. Visualization of the HARV flow can also be provided using CFD, which could help to the experiments in particle choice and expectation of the asymptotic particle position. Given the relative agreement between the initial experiments and the literature, this should prove to be a worthwhile study.

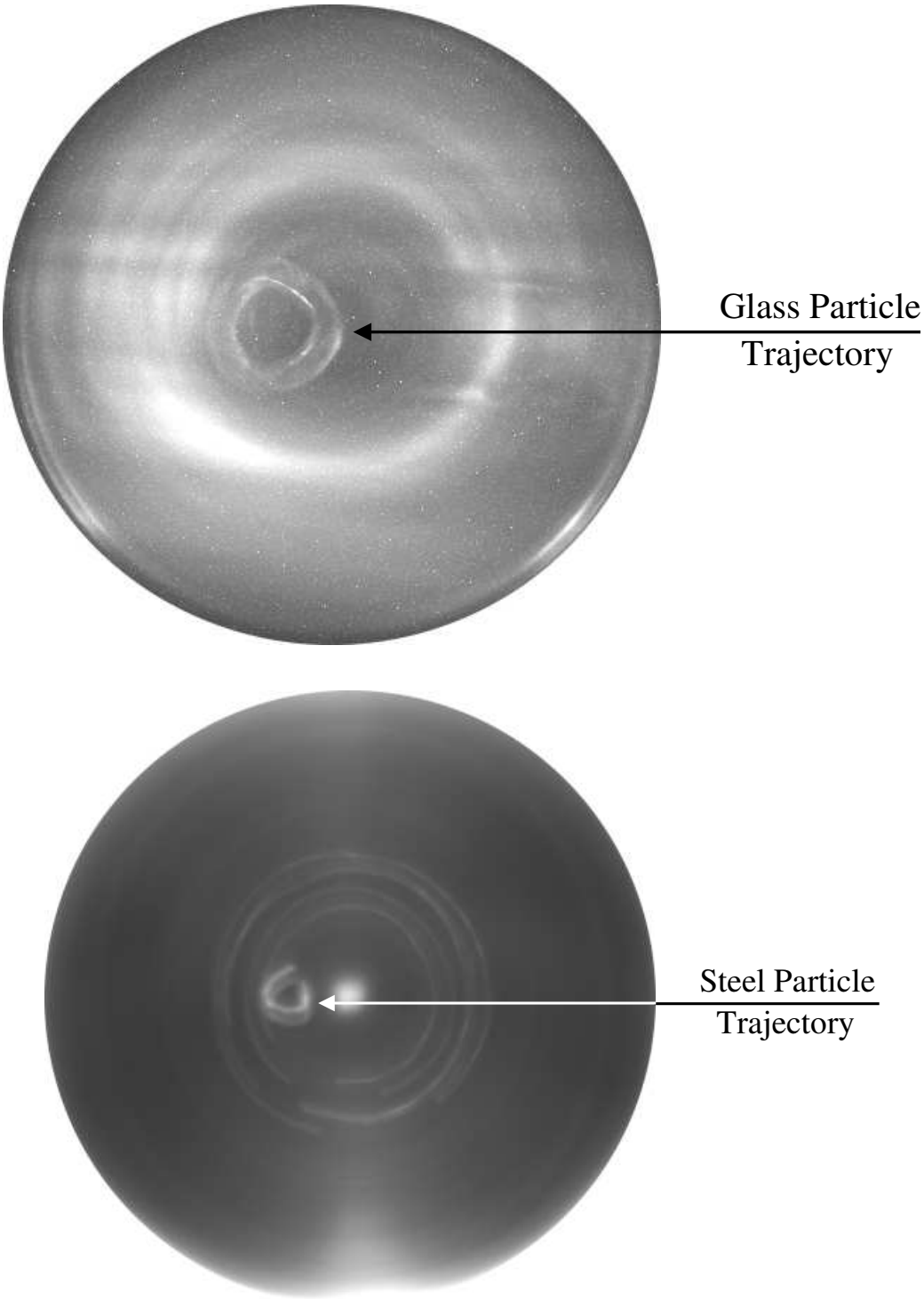

Figure 47: HARV trajectories for (top) 4mm glass beads and (bottom) 3mm steel shot.

APPENDIX A

BIOLOGICAL APPLICATIONS

As has already been discussed, other applications of this work lie in bioengineering processes, such as the study of the RWV flow. Another possible direction could be the study of blood flow in small vessels.

Blood comprises about 7% by weight of the human body and provides numerous functions including transporting oxygen to the tissues; removing carbon dioxide and waste from the tissues and transportation of nutrients. Furthermore, blood is a suspension of red blood cells (erythrocytes or RBC), white blood cells (leukocytes or WBC), and platelets (thrombocytes) in plasma, which is composed of proteins and small molecules in water.

Since red blood cells are the major cellular constituent of blood (comprise over 99% of cellular component of blood), they should be the main focus of modeling blood flow. Human red blood cells are about 8μm in diameter and biconcave discoid in shape. They are comprised of a flexible membrane filled with a hemoglobin solution. Since the red blood cells have no nuclei, low cytoplasmic viscosity, a viscoelastic membrane, and a high ratio of surface area to cell volume, the red blood cells can easily deform under normal conditions. The human circulatory system consists of vessels of a variety of sizes ranging from arteries with a diameter of 2 3.2 cm to capillaries, which have diameters ranging from 5-10 μm.

A.1 FAHRAEUS-LINQUIST EFFECT

The migration behavior of RBCs has been studied extensively, including the effects of hematocrit, blood vessel size, and deformability (of the vessel or the RBC membrane) on blood flow. For example, El-Kareh and Secomb [17] proposed a theoretical model to simulate Red Blood Cell (RBC) migration in bifurcating microvessels. The purpose was to understand the unequal hematocrit (RBC volume fraction) distribution downstream of a blood vessel bifurcation. Additional complexity in the model was due to the inherent properties of RBC to deform and preference for certain orientations once they have deformed. The authors defined a separating streamfunction ahead of a bifurcation, such that RBC migration across the blood flow streamlines near a bifurcation contributes to the unequal hematocrit downstream of the split. Others [19] have also developed similar computational models to model the motion of deformable capsules into pores of a membrane.

Others [20, 84] have also found that the migration behavior of rigid RBC is more similar to that of rigid spheres than normal, deformable cells. This is because suspensions of rigid cells exhibit Newtonian behavior and impart the highest viscosity to blood. If the cells are neutrally buoyant (*i.e.* $\rho_{cell} = \rho_{fluid}$), they merely rotate in the direction of flow. For RBCs, such motion is known as flipping (see figure 48, top), as the cells maintain a constant height or radial position while being advected through the vessel.

The cells can also migrate towards the vessel centerline [17]. However, suspensions of normal cells exhibit shear thinning behavior due to cell deformation, and the cells have been known to assume a variety of shapes while still migrating towards the centerline – a phenomena known as the known as the Fahraeus-Linquist (or plasma skimming) Effect [85]. In high shear, or when the viscosity ratio of the inner to outer fluid is low, the RBC will lose fore-aft symmetry while the cell membrane rotates about the hemoglobin solution, a condition known as tank-treading (see figure 48, bottom). Such shapes are more prominent when the vessel diameter is smaller than the longest dimension of a RBC, but for human blood the viscosity ratio is usually high enough [86] to suppress this phenomenon.

Part of the complexity in modeling blood is that in smaller vessels, the medium cannot be treated as a continuum but rather as a suspension of elastic, deformable particles. Thus,

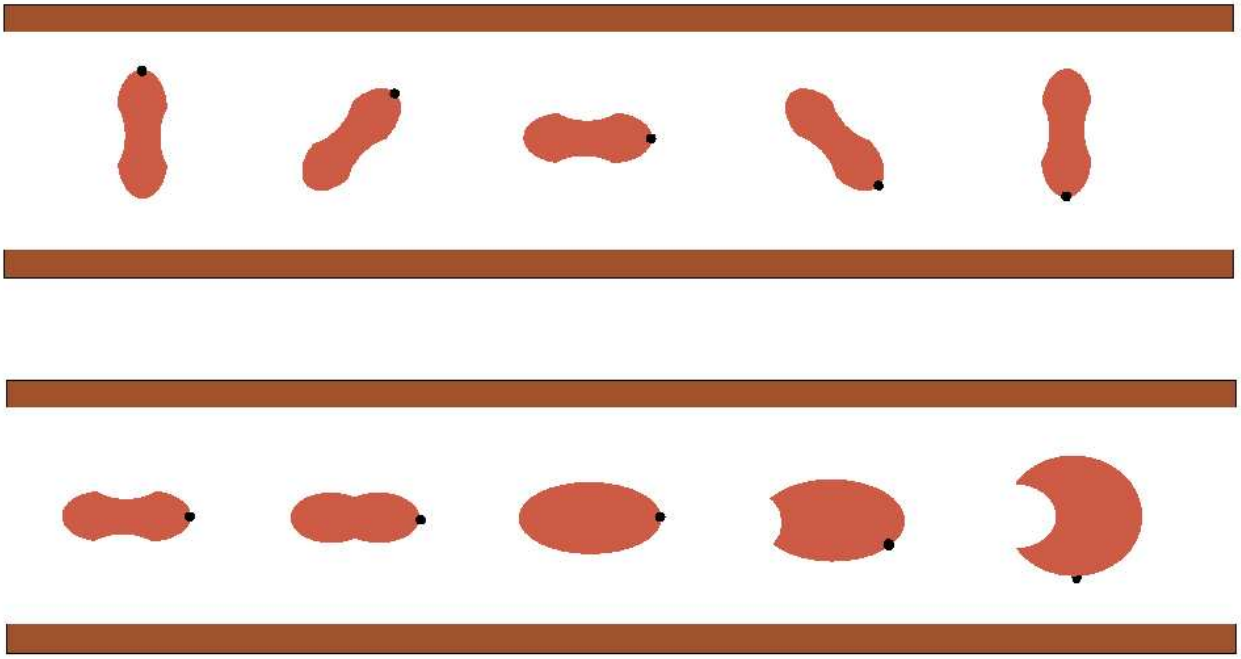

Figure 48: RBC motion: (top) flipping; (bottom) tank-treading

blood flow in vessels with diameter ≥ 100 μm is considered Newtonian, *i.e.* the rate of deformation varies linearly with shear stress and the viscosity can be determined to a somewhat constant value. However, blood flow in smaller vessels (diameter le 100 μm) is considered to have shear-thinning characteristics due to the deformability of the RBCs, and the fluid has to be approximated with a suspension model. From the literature review, it would seem that there is relatively little interaction between neighboring erythrocytes or Red Blood Cells in microcirculation, thus it is sufficient to approximate the motion of a single cell in motion using the BBO model. The RBC is represented by a rigid sphere filled with a hemoglobin solution, migrating in a Poiseuille flow driven by a pressure drop.

Initial particle motion is set equal to fluid motion, eliminating initial disturbances or the need for the history term. Furthermore, the history term could also be neglected since the continuous phase is plasma which can be taken to be a simple fluid with no memory.

Figure 49 shows the effect of initial position of the cell, as well as subsequent positions due to lift. Height=0 represents the vessel centerline, the dashed line represents height=0.5, and height=1 is the wall. As seen in the figure on the left, the particles tend to maintain a fixed height when the model does not include the lift force, whether introduced near the wall or near the centerline. However, when the lift force is included (as seen in the figure on the right), both particles tend towards the vessel center at a steady rate.

A.2 POSSIBLE MODIFICATIONS TO BBO MODEL

There seems to be a critical height (height=0.5) at which the motion transitions from a linear migration to an exponential rate. This might be related to work done by P. Olla in which the author modeled an isolated RBC as an ellipsoid using Jefferys theory [87, 88]. In their study, they found that the flow in a small blood vessel can be separated into two regions:

- **Outer Region**: an isolated RBC in this region would remain in flipping motion. As has been already discussed, rigid spheres would still migrate in this domain.
- **Inner Region**: an isolated cell would dispose itself perpendicular to the flow and assume a parachute shape, while migrating towards the vessel centerline. Such deformation of

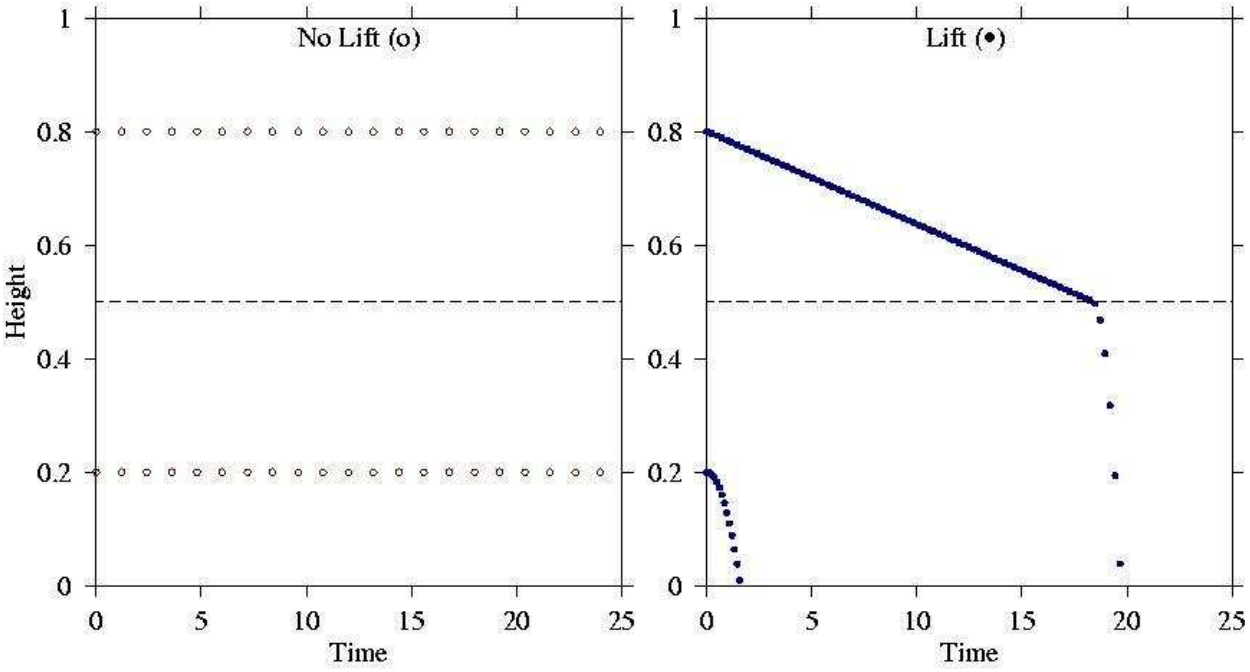

Figure 49: Results for the motion of an isolated rigid sphere moving in a small vessel, with and without lift

the cell is most prevalent near the vessel wall, and produces a transverse drift away from the solid boundary.

This might explain the sharp change in migration behavior, since membrane deformability (and therefore, the effects of tank-treading) is not taken into account in the BBO equation. It is obvious (and consistent with Ollas findings) that inertial effects are not enough to describe the drift of RBCs. Even though the migration behavior to the center of the blood vessel was captured by the BBO model, the rate at which that migration occurs might be inaccurate due to the assumed rigidity and sphericity of the particle.

A possible modification might be to include a drag coefficient based on the Hadamard-Rybczynski Drag Law [51]:

$$C_D = \frac{24}{Re_r}\left(\frac{1+\frac{2}{3}\bar{\mu}}{1+\bar{\mu}}\right) \tag{A.1}$$

$\bar{\mu}$ in A.1 represents the ratio of the viscosity of the continuous phase to that of the fluid inside the representative sphere; Re_r is the Reynolds number based on the relative velocity (**U-V**). This simulates internal flow in response to an external shearing motion, where the outer viscosity would be that of plasma, and the inner viscosity would be that of the RBC hemoglobin solution. In addition, the use of a shape factor could better represent the asphericity of an actual RBC, allowing the particle to assume a number of shapes.

More intricate models have been developed in order to capture the details of erythrocyte migration. Obvious benefits include greater insight into the transport of oxygen and nutrients and better approximation of the local shear stresses. Such models would then allow the estimation of RBC equilibrium positions, shapes and yield more accurate measurements of apparent viscosity.

APPENDIX B

DELPHI STUDY

The University of Pittsburgh's Department of Chemical and Petroleum Engineering is developing a novel integrated curriculum based on block scheduling, which consists of 6 main or pillar courses augmented by a number of concurrent laboratory classes. The author was part of conducting a Delphi Study- a preliminary step in the development of assessment tools to evaluate the effectiveness of a curriculum.

B.1 INTRODUCTION

The undergraduate chemical engineering curriculum at the University of Pittsburgh was changed in 2004 to a block schedule format to better address the shifting focus of the field. Block scheduling allows extended contact time between student and instructor by merging multi-semester courses into a single core class [89, 90]. This has led to the current format based on the 6 pillars of chemical engineering [91], in which students are exposed to an extended interactive learning environment, and instructors are allowed the necessary time to include multi-level descriptions of the subject matter as well as accommodate the varied learning styles in the classroom. Of particular interest is the fact that this change places the emphasis on the understanding of fundamental material properties to better design process-level features – *i.e.* less process- and more product-design.

The change within the department aims to produce improvements in student understanding of major ChE concepts [92], which can be quantitatively meatablesured through the use of a Concept Inventory (CI). This tool measures the effectiveness of a curriculum by testing students understanding of commonly misunderstood fundamental concepts. Previous work by researchers at the Colorado School of Mines [93] resulted in CIs for Transport phenomena, Fluid Mechanics, Thermodynamics which have already been successfully administered at the University of Pittsburgh for the last 2 years. However, CIs for Reaction Kinetics (RK), Process Design and Control (PS) and Material and Energy Balances (ME) are yet to be developed.

This section deals with a particular tool to collect the common misconceptions that could be tested in an inventory, called the *Delphi method* [94]. The purpose of this tool is to gather and condense the expert judgments of experts about a particular subject under the conditions of anonymity, and therefore without bias [95]. In a Delphi study, the idea generation by the participants is independent, isolated and anonymous. Thus, the impact of 'choice-shift' (*i.e.*, the polarization of opinions due to strong personalities or name recognition) is minimized while the opinions are being collected. This study details the procedure by which a Delphi study was used to collect misconceptions which would be used to create CIs for Reaction Kinetics, Process Design and Control and Material and Energy Balances.

B.2 PROCEDURE

In the conventional Delphi Study method, there is no communication between the participants. Rather, information flow is orchestrated by a director and occurs through feedback questionnaires which are periodically sent to the participants. By structuring the group communication in this manner, the process is considered effective at allowing a group of experts to identify the specific characteristics of a problem, and ways to better deal with the problem [95].

For our study, the problem at hand was identifying commonly misunderstood yet fundamental concepts to each of the 3 pillars under consideration (RK, PS and ME). The 13

participants were ChE faculty from nationally renown programs, and the opinion-gathering was done in a series of rounds to first gather and then refine the data. The Round 0 correspondence requested participation in the study and stimulated interest by offering a small monetary incentive. At this stage, the participants were asked to identify a list of commonly misunderstood concepts which were of fundamental importance to any core undergraduate ChE curriculum. The particular invitation was as follows:

November 2004

Dear Respondent:

Thank you for agreeing to participate in our Delphi study of difficult concepts in chemical engineering. As we previously indicated, the study will be conducted in four rounds. In this round, we would like you to list concepts in material and energy balances, reactive processes (kinetics, reactors, and advanced separations), and process systems that you think are either important or difficult for students. Please submit as many items as you would like in each of the categories.

We would like to have this round completed by December 8th so that we can promptly consolidate your responses and move on to the next round.

The response to Round 0 was refined by only keeping concepts that had been identified by two or more participants to eliminate redundancies and/or opinions which could be coalesced. The responses were further evaluated by an 'expert' group made up of three professors with expertise in the three areas of interest (RK, PS and ME). This round yielded 44 RK, 33 ME, 34 PS and 11 general concepts. For Round 1, the condensed questionnaire was electronically sent to the respondents requiring their opinion on the group responses, and their strong agreement or disagreement as to where a particular concept was commonly misunderstood and of high importance on a scale of 0-10. This second invitation is shown below:

March 2005

Dear Respondent,

Thank you for your participation in our Delphi study. As a reminder, the purpose is to identify and rank difficult concepts for undergraduate students in chemical engineering. Based on your Round 1 responses, we have calculated the median and an inter-quartile range of the importance and understanding of each concept. Your task now is to compare your previous ratings from round 1 with the group median and inter-quartile range (provided in parentheses) for each concept. Please explain your rating from Round 1 if it lies outside the range, and then please rank again each concept for understanding (U) and importance (I) on a scale from 0-10, where:

0 - No one understands OR it is not important to understand this concept
10 - Everyone understands OR it is extremely important to understand this concept

You will not have to rank any concept for which you do not feel you have sufficient expertise. You may "skip" the concepts that you do not feel comfortable rating. Please complete your ratings by MIDNIGHT, MAY 11, 2005.

These responses were further refined by defining a cut-off for how high in importance a concept could be while also being poorly misunderstood. Figure 50 shows the cutoff of these concepts based on the average score of the group, which yielded 36 RK, 26 ME, 26 PS and 11 general concepts.

Round 2 was used to further narrow down the idea of a misconception. Participants were given the median ranking as well as the 50% inter-quartile range of the group. They were then asked to revise their responses to further refine the collected data. The third invitation stated the following:

April 2005

Dear Respondent,

Thank you for your participation in our Delphi study. As a reminder, the purpose is to identify and rank difficult concepts for undergraduate students in chemical engineering. Based on your Round 1 responses, we have calculated the median and the 50% inter-quartile range of the importance and understanding for each concept. For Round 2, please compare your previous ratings from round 1 with the group median and range for each concept. Please explain your rating from Round 1 if it lies outside the range, and then rank again each concept for understanding and importance on a scale from 0-10, where:

0 - No one understands OR it is not important to understand this concept
10 - Everyone understands OR it is extremely important to understand this concept

You will not have to rank any concept for which you do not feel you have sufficient expertise. You may "skip" the concepts that you do not feel comfortable rating. Please complete your ratings by MIDNIGHT, MAY 11, 2005.

This yielded 13 RK, 20 ME, 15 PS and 11 general concepts. Comparing Figure 51 to Figure 50 shows the shift in importance and/or understanding of some concepts when the participants had access to the opinions of others within the group.

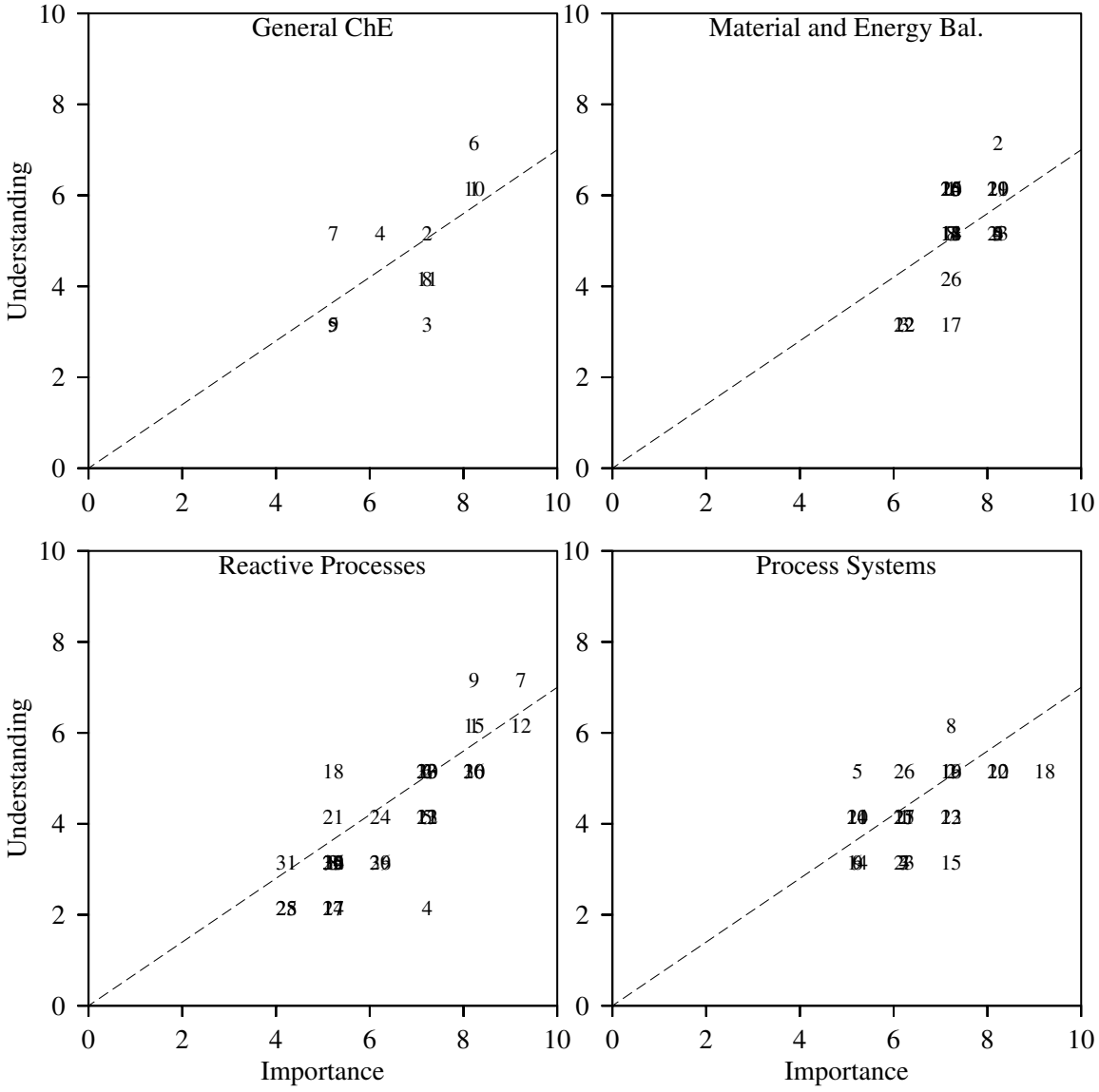

Figure 50: Delphi Study, Round 1 responses.

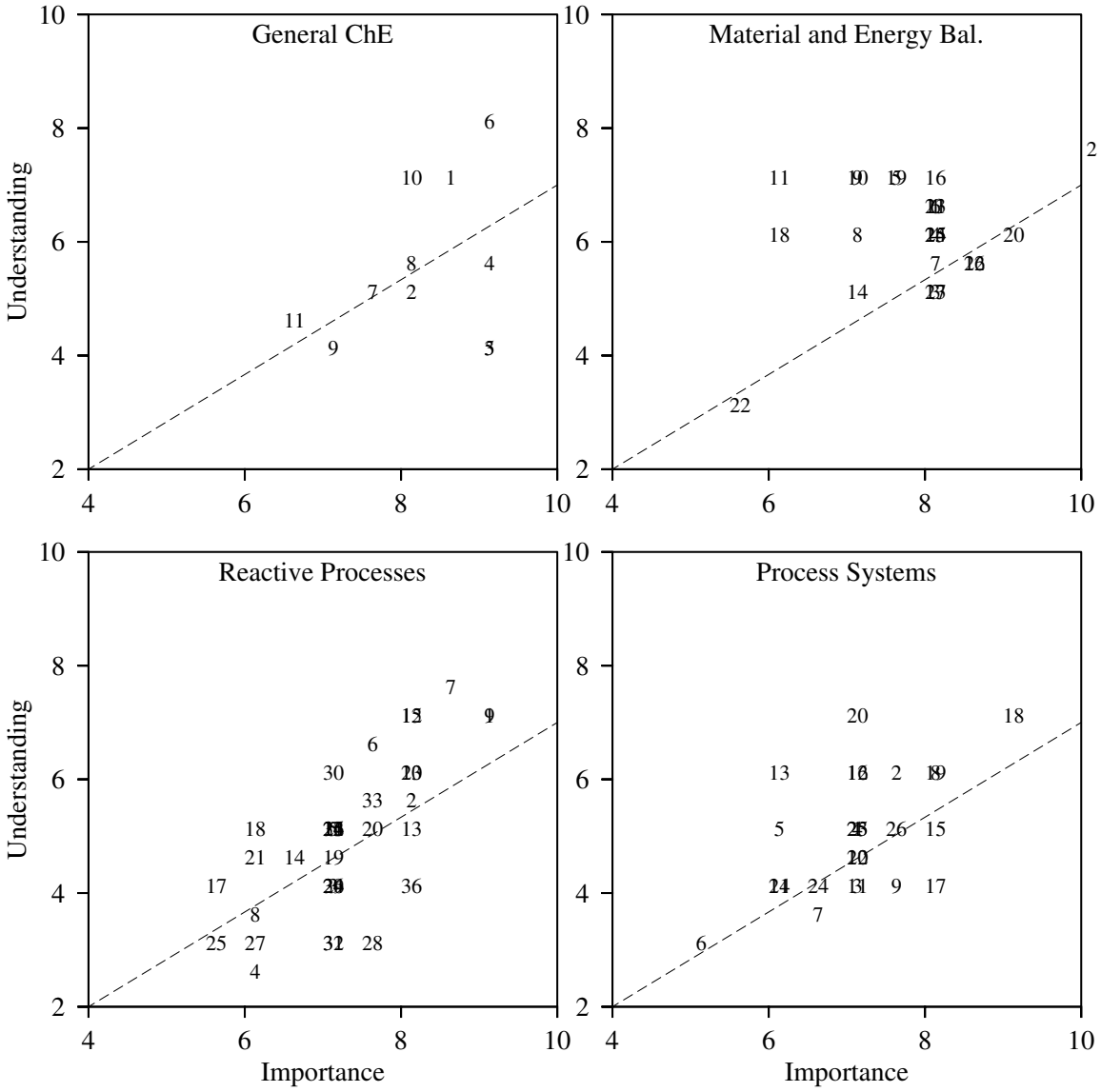

Figure 51: Delphi Study, Round 2 responses.

Table 3: This illustrates the refinement of the number of truly fundamental yet misunderstood concepts with each successive round.

Round	*RK*	*PS*	*ME*
1	44	33	34
2	36	26	26
3	13	20	15
4	11	9	8

B.3 DISCUSSION

The final number of misconceptions which are high in importance but also high in misunderstanding is shown in Table 3, which also shows the narrowing down of group consensus with subsequent rounds. By Round 4 (comprising only of our local experts), the final list was 11 RK, 9 ME, 8 PS with the following 3 GEN misconceptions absorbed into the 3 pillar areas.

- The relationship between *real* (usually with incomplete information) and *ideal* (specific, single-correct-answer) problems
- Connectivity between core science subjects and engineering courses
- More applications from non-traditional areas (bio, energy, environmental, etc.)

For the Reaction Kinetics (RK) pillar, the following misconceptions were identified:

- The relationship between reaction rate expressions/laws and molecular, stochastic and chemical kinetics
- Residence time distribution
- Non-ideal and multiphase reactors, e.g. bubble columns, fluidized, packed, fixed and entrained beds

- Molecular and atomic or elemental species balances on reactive systems (including selectivity, yield, extent of reaction concepts)
- Linear independence of chemical reactions, rate determining step, elementary and non-elementary reactions, complex reaction pathways
- Biological system applications, e.g. metabolic engineering, controlled drug delivery, bioseparations
- Extracting intrinsic kinetics from reactor modeling
- Appropriateness of correlations given acceptable error
- Physical meaning of operating and equilibrium lines
- Reactor stability and safety
- Experimental/theoretical tests for heat and mass transfer limitations in reactors

The following were noted for the Material and Energy Balances pillar (ME):

- Unsteady state processes
- Flow work concept; First Law analysis for open and closed systems
- Thermodynamic state functions, standard state for enthalpy, reference states
- Dimensionless groups (e.g. Thiele modulus, Damkohler, Peclet, Reynolds, Schmidt numbers)
- Systematic means of DOF analysis in reacting systems
- Proper use of equations of state
- Identifying control volume
- Phase diagrams of single species

Finally, the following misconceptions were identified for the Process Systems and Engineering (PS) pillar:

- Reactor network design
- Hierarchical design: heuristics $\rightarrow$ algorithms $\rightarrow$ economics $\rightarrow$ optimization
- Non-ideal and multiphase reactors
- Emphasis on environmentally friendly and high efficiency processes
- Principles of optimization

- Use of experimental data in process analysis and design
- Time-domain modeling
- interactions between design and control

B.4 CONCLUSIONS

Although extremely useful, the Delphi method is not without limitations. The method inherently assumes that the background and experiences of each participant are enough to speak on the topics under consideration. With our study, we consistently received responses from the panel in which they only proffered opinions on sections in which they had particular experience in early rounds and then abstained from doing so in later rounds, particularly when given the response of the group.

Since the panel members were also faculty with responsibilities of their own, there was also the possibility that the amount of time devoted to completely answering the questionnaire was greatly varied. Indeed, some respondents responded with paragraphs when first asked to give their opinions on misconceptions in round 0, whereas others merely stated one sentence topics which were clear to them but required further explanation for the purposes of the study.

One of the most beneficial aspects of this method is participant anonymity because of the way in which the responses are gathered. However, there is no quantitative manner to measure how individuals were possibly swayed since the participants eventually conformed to the median group response, reintroducing the issue of choice-shift after all. Finally, although the group was fairly exhaustive of the issues in teaching their respective fields (which was further confirmed by our expert panel), this does not necessarily mean the list itself was exhaustive as it relates to ChE curricula in the United States.

In spite of these concerns; however, the Delphi method has been used in many fields to gather and refine information in an anonymous and less biased manner and we feel confident that the data compiled here is useful. Eventually, the list of misconceptions will be used by the expert panel to formulate questions to test each concept – these will comprise the

CI. Thus, we successfully employed this tool to aid in creating concept inventories which will be used to gauge the effectiveness of the current ChE curriculum at the University of Pittsburgh, particularly in the Reaction Kinetics, Process Systems and Control and Material and Energy Balances pillars.

B.5 ACKNOWLEDGMENTS

This material is based upon work supported by the National Science Foundation under Grant No. EEC-0342713.

APPENDIX C

NOTATION

English Symbol	Meaning
a	particle radius
g	acceleration due to gravity
k_B	Boltzmann constant
L	cell width
m_p	particle mass
m_f	fluid mass
p	pressure
t	time
T	Temperature
$\mathbf{U}$	fluid velocity
U_o	maximum fluid velocity
$\mathbf{V}$	particle velocity

Greek Symbol	**Meaning**
μ	fluid viscosity
ν	kinematic fluid viscosity
ρ_p	particle density
ρ_f	fluid density
ϵ	perturbation amplitude
τ'	perturbation frequency

BBO constant	**Meaning**
$A = \frac{6\pi a\mu L}{U_o M} \sim \frac{1}{Re}$	particle inertia parameter
$B = \frac{m_f}{M} = \frac{1}{2\alpha+1}$	mass ratio
$C = \frac{6.46a^2}{M}(\frac{\mu\rho L}{U_o})^{\frac{1}{2}}$	lift coefficient
$M = m_p + \frac{1}{2}m_f$	mass scale
$W = \frac{(m_p - m_f)g}{6\pi a\mu U_o}$	settling velocity

BIBLIOGRAPHY

[1] L. Ramirez, E. A. Lim, C. F. M. Coimbra, and M. H. Kobayahi, "On the dynamics of a spherical scaffold in rotating bioreactors," *Wiley Periodicals, Inc.*, 2003.

[2] E. Kreyzig, *Advanced Engineering Mathematics, Eighth ed.* 605 Third Avenue, New York, NY 10158: John Wiley and Sons, Inc., 2001.

[3] M. R. Maxey, "The motion of small spherical particles in a cellular flow field," *Phys. Fluids*, vol. 30, pp. 1915–1928, 1987.

[4] G. Segré and A. Silberberg, "Radial particle displacements in poiseuille flow of suspensions," *Nature*, vol. 189, pp. 209–210, 1961.

[5] G. Segré and A. Silberberg, "Behavior of macroscopic rigid spheres in poiseuille flow," *J. Fluid Mech.*, vol. 14, pp. 115–136, 1962.

[6] J. Lee and A. Ladd, "Axial segregation of a settling suspension in a rotating cylinder," *Physical Review Letters*, vol. 95, p. id 048001, 2005.

[7] B. Chun and A. Ladd, "Inertial migration of neutrally buoyant particles in a square duct: An investigation of multiple equilibrium positions," *Physics of Fluids*, vol. 18, p. id 031704, 2006.

[8] D. Leighton and A. Acrivos, "The shear-induced migration of particles in concentrated suspensions," *J. Fluid Mech.*, vol. 181, pp. 415–439, 1987.

[9] M. Tirumkudulu, A. Tripathi, and A. Acrivos, "Particle segregation in monodisperse sheared suspensions," *Physics of Fluids*, vol. 11, pp. 507–509, 1999.

[10] M. Tirumkudulu, A. Mileo, and A. Acrivos, "Particle segregation in monodisperse sheared suspensions in a partially filled rotating horizontal cylinder," *Physics of Fluids*, vol. 12, pp. 1615–1618, 2000.

[11] M. F. Frank, D. Anderson, E. R. Weeks, and J. F. Morris, "Particle migration in pressure-driven flow of a brownian suspension," *J. Fluid Mech.*, vol. 493, pp. 363–378, 2003.

[12] O. Usta, J. Butler, and A. Ladd, "Flow-induced migration of polymers in dilute solution," *Physics of Fluids*, vol. 18, p. id 031703, 2006.

[13] M. V. Kameneva, Z. J. Wu, A. Uraysh, B. Repko, K. N. Litwak, T. R. Billiar, M. P. Fink, R. L. Simmons, B. P. Griffith, and H. S. Borovetz, "Blood soluble drag-reducing polymers prevent lethality from hemorrhagic shock in acute animal experiments," *Biorheology*, vol. 41, pp. 53–64, 2004.

[14] M. S. Jhon and K. F. Freed, "Polymer migration in newtonian fluids," *J. Polymer Sc.*, vol. 23, pp. 955–971, 1985.

[15] A. Crisanti, M. Falcioni, A. Provenzale, and A. Vulpiani, "Passive advection of particles denser than the surrounding fluid," *Physics Letters A*, vol. 150 (2), pp. 79–84, 1990.

[16] J. Ye and M. C. Roco, "Particle rotation in a couette flow," *Physics of Fluids A*, vol. 4, pp. 220–224, 1992.

[17] A. W. El-Kareh and T. W. Secomb, "A model for red blood cell motion in bifurcating microvessels," *International Journal of Multiphase Flow*, vol. 26, pp. 1545–1564, 2000.

[18] R. L. Schiek and E. G. Shaqfeh, "Cross streamline migration of slender brownian fibres in plane poiseuille flow," *J. Fluid Mech.*, vol. 332, pp. 23–39, 1997.

[19] C. Quéguinar and D. Barthés-Biesel, "Asymmetric motion of capsules through cylindrical channels," *J. Fluid Mech.*, vol. 348, pp. 349–376, 1997.

[20] C. Coulliette and C. Pozrikidis, "Motion of an array of drops through a cylindrical tube," *J. Fluid Mech.*, vol. 358, pp. 1–28, 1998.

[21] J. Magnaudet, "Small inertial effects on a spherical bubble, drop or particle moving near a wall in a time-dependent linear flow," *J. Fluid Mech.*, vol. 485, pp. 115–142, 2003.

[22] P. Vasseur and R. G. Cox, "The lateral migration of a spherical particle in two-dimensional shear flow," *J. Fluid Mech.*, vol. 78, pp. 385–393, 1976.

[23] R. C. A. Nadim and H. Brenner, "Transport of sedimenting brownian particles in a rotating poiseuille flow," *Phys. Fluids*, vol. 28, pp. 3457–3466, 1985.

[24] J. S. Halow and G. B. Wills, "Radial migration of spherical particles in couette system," *AIChEJ*, vol. 16, pp. 281–286, 1970.

[25] A. Acrivos, R. Mauri, and X. Fan, "Shear-induced resuspension in a couette device," *Int. J. Multiphase Flows*, vol. 19, pp. 797–802, 1993.

[26] C. C. Chan and J. C. H. Fung, "The change in settling velocity of inertial particles in cellular flow," *Fluid Dynamics Research*, vol. 25, pp. 257–273, 1999.

[27] R. Mauri and D. T. Papageorgiou, "The onset of particle segregation in plane couette flows of concentrated suspensions," *Intl. J. Multiphase Flows*, vol. 28, pp. 127–136, 2002.

[28] B. P. Ho and L. G. Leal, "Inertial migration of rigid spheres in two-dimensional unidirectional flows," *J. Fluid Mech.*, vol. 65, pp. 365–400, 1974.

[29] H. A. Stone, "Dynamics of drop deformation and breakup in viscous fluids," *Annu. Rev. Fluid Mech.*, vol. 26, pp. 65–102, 1994.

[30] M. J. F. and J. F. Brady, "Pressure-driven flow of a suspension: Bouyancy effects," *Int. J. Multiphase Flows*, vol. 24, pp. 105–130, 1998.

[31] P. G. Saffman, "The lift on a small sphere in a slow shear flow," *J. Fluid Mech.*, vol. 22, pp. 385–398, 1965.

[32] R. F. Mctigue, R. C. Givler, and J. W. Nunziato, "Rheological effects of nonuniform particle distributions in dilute suspensions," *Journal of Rheology*, vol. 30, pp. 1053–1076, 1986.

[33] H. G. Choi and D. D. Joseph, "Fluidization by lift of 300 circular particles in plane poiseuille flow by direct numerical simulation," *J. Fluid Mech.*, vol. 438, pp. 101–128, 2001.

[34] D. D. Joseph and D. Ocando, "Slip velocity and lift," *J. Fluid Mech.*, vol. 454, pp. 263–286, 2002.

[35] P. Ashwin and G. P. King, "A study of particle paths in non-axisymetric taylor-couette flows," *J. Fluid Mech.*, vol. 338, pp. 341–362, 1997.

[36] G. King, G. Rowlands, M. Rudman, and A. Yannacopoulos, "Predicting chaotic dispersion with eulerian symmetry measures: wavy taylor-vortex flow," *Phys. Fluids*, vol. 13(9), pp. 2522–2528, 2001.

[37] G. Baier and M. D. Graham, "Two-fluid taylor-coutte flow: Experiments and linear theory for inmiscible liquids between corotating cylinders," *Phys. Fluids*, vol. 10, pp. 3045–3055, 1998.

[38] S. T. Wereley and R. M. Lueptow, "Inertial migration in a taylor couette rotating filter," *Phys. Fluids*, vol. 11, pp. 325–333, 1999.

[39] 12^{th} International Couette-Taylor Workshop, *Spiral and Wavy Vortex Flows in Short Counter-Rotating Couette-Taylor Cells*, (Evanston, IL), September 6-8 2001.

[40] P. Annamalai and R. Cole, "Particle migration in rotating liquids," *Phys. Fluids*, vol. 29 (3), pp. 647–649, 1986.

[41] A. D. Harvey, D. H. West, and N. B. Tufillaro, "Evaluation of laminar mixing in stirred tanks using a discrete time particle mapping procedure," Tech. Rep. HPL-1999-56, Integrated Solutions Laboratory, Hewlett Packard Laboratories Palo Alto, April 1999.

[42] G. Gauthier, P. Gondret, F. Moisy, and M. Rabaud, "Instabilities in the flow between co- and counter-rotating disks," *J. Fluid Mech.*, vol. 473, pp. 1–21, 2002.

[43] M. M. Alvarez, J. M. Zalc, T. Shinbrot, and F. J. Muzzio, "Mechanisms of mixing and creation of structure in laminar stirred tanks," *AIChE Journal*, vol. 48, pp. 2135–2148, 2002.

[44] G. O. Fountain, D. V. Khakar, I. Mezic, and J. M. Ottino, "Chaotic mixing in a bounded three-dimensional flow," *Journal of Fluid Mechanics*, vol. 417, pp. 265–301, 2000.

[45] T. Shinbrot, M. M. Alvarez, J. M. Zalc, and F. Muzzio, "Attraction of minute particles to invariant regions of volume preserving flows by transients," *Physical Review Letters*, vol. 86, No. 7, pp. 1207–1210, 2001.

[46] J. Morin, D. Preterre, V. Keravec, and C. Thuillez, "Rotating wall vessel as a new *in vitro* shear stress generation system: Application to rat coronary endothelial cell cultures," *Cell Biology and Toxicology*, vol. 19, pp. 227–242, 2003.

[47] N. Rowghani, M. Heise, D. McKeel, E. McGee, R. Koepsel, and A. Russel, "Maintenance of morphology and growth of ovarian follicles in suspension culture," *Tissue Engineering*, vol. 10 (3), pp. 545–552, 2004.

[48] N. Cowger, K.C.O'Connor, T. Hammond, D. Lacks, and G. Navar, "Characterization of bimodal cells death of insect cells in a rotating-wall vessel and shaker flask," *Biotechnology and Bioengineering*, vol. 64 (1), pp. 14–26, 1999.

[49] C. M. Begley and S. J. Kleis, "The fluid dynamic and shear environment in the nasa/jsc rotating-wall perfused-vessel bioreactor," *Biotechnology and Bioengineering*, vol. 70 (1), pp. 32–40, 2000.

[50] F. P. Bretherton, "The motion of rigid particles in a shear flow at low reynolds number," *J. Fluid Mech.*, vol. 14, pp. 284–304, 1962.

[51] C. Crowe, M. Sommerfield, and Y. Tsuji, *Multiphase Flows with Droplets and Particles*. Boca Raton, FL: CRC Press, 1998.

[52] E. E. Michaelides, "Review- the transient equation of motion for particles, bubbles, and droplets," *Journal of Fluids Engineering*, vol. 119, pp. 233–247, 1997.

[53] L. P. Wang, M. R. Maxey, T. D. Burton, and D. E. Stock, "Chaotic dynamics of particle dispersion in fluids," *Phys. Fluids A*, vol. 4, pp. 1789–1804, 1992.

[54] M. R. Maxey and J. J. Riley, "Equation of motion for small rigid spheres in a nonuniform flow," *Phys. Fluids*, vol. 26, pp. 883–888, 1983.

[55] C. F. M. Coimbra and R. H. Rangel, "General solution of the particle momentum equation in unsteady stoke's flows," *Journal of Fluid Mechanics*, vol. 370, pp. 53–72, 1998.

[56] P. G. Saffman, "Corrigendum, the lift on a small sphere in a slow shear flow," *J. Fluid Mech.*, vol. 31, p. 624, 1968.

[57] H. A. Stone, "Philip saffman and viscous flow theory," *J. Fluid Mech.*, vol. 409, pp. 293–310, 2000.

[58] J. B. McLaughlin, "Particle size effects on lagrangian turbulence," *Phys. Fluids*, vol. 31, pp. 2544–2553, 1988.

[59] J. B. McLaughlin, "The lift on a small sphere in wall-bounded linear shear flows," *J. Fluid Mech.*, vol. 246, pp. 249–265, 1993.

[60] E. S. Asmolov, "The inertial lift on a spherical particle in a plane poiseuille flow at large channel reynolds number," *J. Fluid Mech.*, vol. 381, pp. 63–87, 1999.

[61] C. F. M. Coimbra and M. H. Kobayashi, "On the viscous motion of a small particle in a rotating cylinder," *J. Fluid Mech.*, vol. 469, pp. 257–286, 2002.

[62] D. Legendre and J. Magnaudet, "A note on the lift force on a spherical bubble or drop in a low-reynolds number shear flow," *Phys. Fluids*, vol. 9, pp. 3572–3574, 1997.

[63] M. Agrawal, A. Bakker, and M. Prinkey, "Tracking big particles," tech. rep., Fluent Newsletter, Fall 2003.

[64] H. Stommel, "Trajectories of small bodies sinking slowly through convection cells," *J. Marine Research*, vol. 8, pp. 24–29, 1949.

[65] R. Abraham and J. E. Marsden, *Foundations of Mechanics, Second Edition*. Reading, Massachusetts: The Benjamin/Cummings Publishing Co., 1978.

[66] H. Aref, "The development of chaotic advection," *J. Fluid Mech.*, vol. 14 (4), pp. 1315–1325, 2002.

[67] A. Babiano, J. H. E. Cartwright, O. Piro, and A. Provenzale, "Dynamics of a small neutrally buoyant sphere in a fluid and targeting in hamiltonian systems," *Physical Review Letters*, vol. 84(25), pp. 5764–5767, 2000.

[68] J. B. Weiss, "Hamiltonian maps and transport in structured fluids," *Physica D*, vol. 76, pp. 230–238, 1994.

[69] J. Laskar, "A numerical experiment on the chaotic behaviour of the solar system," *Nature*, vol. 338, pp. 237–238, 1989.

[70] H. Levison, J. Lissauer, and M. Duncan, "Modeling the diversity of outer planetary systems," *Astron. J.*, vol. 116, pp. 1998–2014, 1998.

[71] A. C. Correia and J. Laskar, "The four final rotation states of venus," *Nature*, vol. 411, pp. 767–770, 2001.

[72] CSIRO, *Predicting Gas-Liquid Flow in a Mechanically-Stirred Tank*, (Melbourne, Australia), December 6-8 1999.

[73] D. J. Lamberto, F. J. Muzzio, and P. D. Swanson, "Using time-dependent rpm to enhance mixing in stirred vessels," *Chem. Eng. Sci.*, vol. 51(5), pp. 733–741, 1996.

[74] A. A. Abatan, W. L. Vargas, and J. J. McCarthy, "Particle Migration in the Rotating Flow between Co-Axial Disks." to appear in AICHE Journal, 2006.

[75] H. W. Broer, "Kam theory: The legacy of kolmogorov's 1954 paper," *Bulletin of the American Mathematical Society*, vol. 41(4), pp. 507–521, 2003.

[76] M. Whittle and E. Dickinson, "On simulating colloids by dissipative particle dynamics: Issues and complications," *J. of Colloid and Interface Science*, vol. 242, pp. 106–109, 2001.

[77] S. Willemsen, H. Hoefsloot, D. Visser, P. Hamersma, and P. Iedema, "Modelling phase change with dissipative particle dynamics using a consistent boundary condition," *J. Comp. Phy.*, vol. 162, pp. 385–394, 2000.

[78] S. Willemsen, H. Hoefsloot, and P. Iedema, "Mesoscopic simulation of polymers in fluid dynamics problems," *J. Stat. Phys.*, vol. 107, pp. 53–65, 2002.

[79] X. Fan, N. Phan-Thien, N. T. Yong, X. Wu, and D. Xu, "Microchannel flow of a macromolecular suspension," *Phys. Fluids*, vol. 15, pp. 11–21, 2003.

[80] A. T. Clark, M. Lal, J. N. Ruddock, and P. B. Warren, "Mesoscopic simulation of drops in gravitational and shear fields," *Langmuir*, vol. 16, pp. 6342–6350, 2000.

[81] M. Ripol, M. H. Ernst, and P. Español, "Large scale and mesoscopic hydrodynamics for dissipative particle dynamics," *Journal of Chemical Physics*, vol. 115, pp. 7271–7284, 2001.

[82] M. Revenga, I. Zúñiga, and P. Español, "Boundary conditions in dissipative particle dynamics," *Computer Physics Communications*, vol. 121-122, pp. 309–311, 1999.

[83] S. Chen and G. D. Doolen, "Lattice boltzmann method for fluid flows," *Annual Reviews in Fluid Mechanics*, vol. 30, pp. 329–364, 1998.

[84] P. Gaehtgens, "Motion, deformation, and interaction of blood cells and plasma during flow through narrow capillary tubes," *Blood Cells*, vol. 6(4), pp. 799–817, 1980.

[85] M. V. Kameneva, G. W. Burgreen, K. Kond, B. Repko, J. F. Antaki, and M. Umezu, "Effects of turbulent stresses upon mechanical hemolysis: Experimental and computational analysis," *ASAIO J.*, 2004.

[86] R. Pal, "Rheology of concentrated suspensions of deformable elastic particles such as human erythrocyte," *J. Biomechanics*, vol. 36, pp. 981–989, 2003.

[87] P. Olla, "The role of tank-treading motions in the tranverse migration of a spheroidal vesicle in a shear flow," *J. Phys. A, Math Gen.*, vol. 30, pp. 317–329, 1997.

[88] P. Olla, "A simplified model for red cell dynamics in small blood vessels," *Phys. Rev. Letters*, vol. 82 (2), pp. 453–456, 1999.

[89] J. Carroll, "Organizing time to support learning," *The School Administrator*, vol. 51, pp. 26–33, 1994.

[90] R. Canady and M. Rettig, *Block Scheduling: A Catalyst for Change in High Schools*. Priceton, New Jersey: Eye on Education, Inc., 1995.

[91] J. McCarthy and R. Parker, "The pillars of chemical engineering: A block scheduled curriculum," *Chemical Engineering Education*, vol. 38(4), pp. 292–301, 2004.

[92] J. McCarthy, A. Abatan, R. Parker, and M. Besterfield-Sacre, "Work in progress: Pillars of chemical engineering," in *Proceedings of the 2005 Frontiers in Education (FIE) conference*, Indianapolis, IN, October 19-22, 2005.

[93] R. Streveler, B. Olds, and R. Miller, "Using a delphi study to identify the most difficult concepts for students to master in thermal and transport science," in *Proceedings of the American Society for Engineering Education (ASEE) Annual Conference and Exposition*, 2003.

[94] G. Gray, S.Krause, J. Martin, C. Midkiff, B. Notaros, M. Pavelick, D. Rancour, T. Reed-Rhoads, P. Steif, R. Streveler, and K. Wage, "Progress on concept inventory assessment tools," in *Proceedings of the 33rd ASEE/IEEE Frontiers in Education (FIE) Conference*, Boulder, CO, November 5-8, 2003.

[95] M. Clayton, "Delphi: A technique to harness expert opinion for critical decision-making tasks in education," *Educational Psychology*, vol. 17 (4), pp. 373–386, 1997.